

# Event Reconstruction for ICAL Detector and Neutrino Mass Hierarchy Sensitivity Analysis at India-based Neutrino Observatory (INO)

A Thesis

Submitted to the  
Tata Institute of Fundamental Research, Mumbai  
for the degree of Doctor of Philosophy  
in Physics

by  
Kolahal Bhattacharya

School of Natural Sciences  
Tata Institute of Fundamental Research  
Mumbai  
August, 2015

Final version submitted in December, 2015

---

DECLARATION

---

## **DECLARATION**

This thesis is a presentation of my original research work. Wherever contributions of others are involved, every effort is made to indicate this clearly, with due reference to the literature, and acknowledgement of collaborative research and discussions.

The work was done under the guidance of Prof. Naba K Mondal, at the Tata Institute of Fundamental Research, Mumbai.

Kolahal Bhattacharya

In my capacity as supervisor of the candidate's thesis, I certify that the above statements are true to the best of my knowledge.

Prof. Naba K Mondal

Date:

---

## ABSTRACT

---

India-based Neutrino Observatory (INO) is an upcoming underground basic science project undertaken by the Government of India for joining the worldwide efforts to study the properties of neutrino, an extremely illusive fundamental particle. A 50 kilo ton magnetized Iron **CAL**orimeter detector, equipped with about 30000 (2 m×2 m) RPC detectors serving as active planes, ICAL, will lead the major atmospheric neutrino oscillation experiment in INO and will make an attempt to resolve the neutrino mass hierarchy problem.

The detector will be stationed underground in a cavern, below the West Bodi Hills in Theni district of Tamil Nadu in South India. It will observe atmospheric neutrinos coming from all directions (even those that cross the earth and enter the detector from the ground up) in a wide range of energy  $E_\nu \in [0.5 - 15] GeV$ . Cosmic rays will mostly be shielded by the rock coverage of the hill, of at least a kilometer in every direction. The neutrinos will undergo various types of charged current and neutral current interactions and will generate a variety of secondary particles. These particles will bend in the magnetic field and will keep their foot prints at the active RPC planes in the form of electronic signals.

In this thesis, we first developed the methods of dealing with such experimental measurements in a GEANT4 based detector simulation framework. A C++ based software for event reconstruction was developed that performs pattern recognition (track finding) and track fitting. The former was designed to isolate muon tracks from the hadron shower in charged current  $\nu_\mu$  events. These tracks were fitted with a robust Kalman filter algorithm. Neutrino events generated by NUANCE were simulated by GEANT4 toolkit and muons were reconstructed by the reconstruction package. Apart from that, the hadron showers were also calibrated against the number of hadron hits in event by event basis, to estimate the hadron energy in any given event with somewhat poorer energy resolution. The reconstructed events were then analyzed using multivariate technique (TMVA) for efficiently isolating a pure sample for performing the oscillation analysis. This sample was finally used to estimate the neutrino mass hierarchy sensitivity of the ICAL experiment.

**To those who introduced me to the world of physics**

*Stuart Anderson*

&

*Debapriyo Syam*

**To those who inspired me**

*Geeta Bandyopadhyay*

&

*Sudakshina Ganguly*

&

*Pranab Dasgupta*

&

*Amal Bhattacharya*

---

## ACKNOWLEDGEMENTS

---

I would first like to thank my thesis advisor Prof. Naba K Mondal, working with whom taught me various things about modern day scientific research. The independence that I enjoyed while working with you is a unique asset for any graduate student. If I am required to do PhD again (perhaps not in INO!), I would prefer to do it with you only. The professional attitude which I learned from you, will remain as one of my greatest treasures for my future career in research. The same is true for Prof. Acharya whose silent role always propelled me forward to achieve my endeavors. I would also express my gratitude to Prof. Majumder and Prof. Banerjee who were the greatest mentors when I was developing the reconstruction code for ICAL.

I am grateful to the immense support I have received from my girlfriend and wife, Dr. Tamali Sikder. Her presence helped me recover from the hours of disappointments that is common to any PhD student. Thanks for tolerating me, for waking up at every night and doing calculations by switching on the tube light, while you were sleeping. Your presence made this journey a lot smoother. You opened the gateway for me to interact with more number of people than I usually do and this only enriched me over past few years.

One of the crucial persons in my journey from a student to a physicist is Swastik Da, who lit the light of my life. The light is still on and will remain so, to guide me in the way ahead of me. Your critical comments only help me to understand the nature in a better fashion. In TIFR, I had the opportunity to interact with people with the greatest minds like Sayan Da, Jyotirmoy Da and Amlan Da. The more I grow, the more I am able to appreciate their words.

I must mention my colleagues from the INO group and the HECR students' hall. Sharing time with you was an wonderful experience. Together we have had some of the happiest moments of our lives. The C++ tips and tricks from Tarak and Meghna, the trip to Bodi hills at the INO site while attending the collaboration meeting, the Friday detector simulation meetings at 3:00 pm etc. - all these shaped me in today's form. Thanks to all of you Animesh, Lakshmi, Meghna, Mathi, Moon Moon, Neha and last but not the least Saurav. I hope that your dream (expressed at the Matheran hill top) comes to reality as early as possible.

I am fortunate to have some wonderful friends like Khadiza, Atreyee, Soureek, Nairit, Ritam, Subhadeep and Shubhranshu in the last phase of my PhD in TIFR. They were kind enough to extend their helping hands when I needed to transfer my items. The same is true for Ramkrishna.

The discussion will remain incomplete without mentioning my college friends Manoneeta, Tanmay and Saurav (Maths). Sharing room with Tanmay during coursework was a hilarious experience. Working together in electronics project, walking together at marine drive, discussing together on symmetries in QM and playing together the game of 29 - we both shared a great time. I hope to carry forward the friendship, mate! I am also grateful to Saurav for precious discussions on various topics. Manoneeta, the selected one, is the person who was convinced about my potentials, even when she did not know

how to solve most of the potentials which appear in physics. In spite of all fight with you, your critical comments always helped me to find the correct way. Thanks for being such a wonderful friend.

---

## CONTENTS

---

1	SYNOPSIS	xiv	
1.1	Introduction	xiv	
1.2	Perspective	xv	
1.3	Track fitting with single muon (GEANT4 Monte Carlo)	xvi	
1.3.1	Validation of existing Kalman filter code	xvii	
1.3.2	Identifying the source of problems	xviii	
1.3.3	Improvements in track reconstruction	xviii	
1.3.4	Track element merging	xx	
1.3.5	Results	xxi	
1.4	A more realistic approach to MH analysis	xxii	
1.4.1	Pattern recognition program	xxii	
1.4.2	Event selection	xxiv	
1.4.3	$\nu$ MH sensitivity analysis	xxv	
1.5	Scope of improvements	xxv	
1.6	Acknowledgements	xxvi	
<b>I</b>	<b>Neutrino Physics and Perspective of INO-ICAL</b>		<b>0</b>
2	THESIS INTRODUCTION	1	
2.1	Introduction	1	
3	NEUTRINO PHYSICS	3	
3.1	Introduction	3	
3.2	Neutrino deficit experiments before 2000	5	
3.2.1	Chlorine experiment by Ray Davis	5	
3.2.2	SAGE and GALLEX	6	
3.2.3	Super Kamiokande	6	
3.2.4	SNO	6	
3.2.5	Atmospheric neutrinos: Super Kamiokande	7	
3.3	Explanation of the findings	8	
3.3.1	Two neutrino mixing	9	
3.3.2	Three neutrino mixing	10	
3.4	KamLAND and Super Kamiokande	12	
3.4.1	KamLAND	12	
3.4.2	Super Kamiokande	12	
3.5	Matter effects in neutrino oscillation	12	
3.6	Neutrino oscillation experiments after 2000	14	
3.6.1	Experiments	15	
3.6.2	Current status	17	
3.6.3	Open questions	17	
3.6.4	India-based Neutrino Observatory	18	

4	ICAL DETECTOR AT INDIA BASED NEUTRINO OBSERVATORY PROJECT	20
4.1	Introduction	20
4.2	About the detector	21
4.3	Atmospheric neutrino flux at INO	21
4.4	ICAL detector	21
4.5	Active detector elements: RPC	23
4.6	ICAL magnet	25
<b>II</b>	<b>ICAL Simulation and Reconstruction Framework</b>	<b>26</b>
5	GEANT4 DETECTOR SIMULATION AND DIGITIZATION	27
5.1	Introduction	27
5.2	Detector construction	27
5.2.1	Construction of Iron CALorimeter	27
5.2.2	Implementation of Magnetic field	28
5.3	GEANT4 simulation	29
5.3.1	Signal generation at sensitive detector	30
6	TRACK RECONSTRUCTION I: PATTERN RECOGNITION	32
6.1	A brief outline of the algorithm	33
6.1.1	Forming Hits and Clusters	34
6.1.2	Forming Triplets	35
6.1.3	Joining Triplets and Forming Segments/Track-lets	35
6.1.4	Forming a track and shower	37
6.2	Setting the properties of the seed track	37
6.2.1	Z direction of motion	38
6.2.2	Vertex position of the seed track	38
6.2.3	Calculation of $t_x$ and $t_y$	38
6.2.4	Fully/partially contained events	39
6.2.5	Events in dead/inactive space	39
6.2.6	Calculation of standard error of measurements	39
6.3	Performance of the program	40
6.3.1	Neutral current background rejection performance	41
6.3.2	Degree of muon-hadron separation	42
6.3.3	Estimation of correct direction of the particle	42
6.3.4	Properties of seed track: input to track fitter	43
7	TRACK RECONSTRUCTION II: TRACK FITTING	44
7.1	Qualitative picture of the process	45
7.2	Kalman filter formalism in HEP experiments	47
7.2.1	Nomenclature of quantities	47
7.2.2	Prediction to next site with a measurement	48
7.2.3	Filtering the estimate at the current site	49
7.2.4	Smoothing the fitted track	49
7.3	Kalman filter in ICAL@INO	50
7.3.1	Track following method	51
7.3.2	State and error propagation for $(x, y, t_x, t_y)$	53

7.3.3	Signed inverse momentum	55	
7.3.4	Random error contribution	58	
7.4	Track fitting results	60	
7.4.1	Single muon results	61	
7.4.2	Performance from quantitative aspects	65	
7.4.3	Momentum and direction resolution	66	
7.4.4	Improvements of the existing code	68	
7.4.5	CPU Time	70	
7.4.6	NUANCE event reconstruction performance	70	
7.4.7	Hadron energy calibration	72	
7.5	Influence of other factors	73	
7.6	Flow chart of reconstruction program	73	
7.6.1	InoPatternRecognition	74	
7.6.2	InoTrackFitAlg	75	
<b>III Event Selection</b>			<b>76</b>
8	EVENT SELECTION	77	
8.1	Introduction	77	
8.2	Trial and error methods	78	
8.3	Multivariate techniques	79	
<b>IV Neutrino Mass Hierarchy Sensitivity Analysis and Results</b>			<b>82</b>
9	NEUTRINO MASS HIERARCHY SENSITIVITY ANALYSIS	83	
9.1	Introduction	83	
9.2	Event generation with NUANCE	84	
9.3	Plan of mass hierarchy sensitivity analysis	85	
9.4	Mass hierarchy sensitivity result	88	
9.5	Scope of improvements	89	
<b>V Appendix</b>			<b>91</b>
10	APPENDIX: A	92	
<b>VI Bibliography</b>			<b>94</b>

---

LIST OF TABLES

---

Table 1	$\nu$ oscillation parameters	xv
Table 2	Magnetic Field Integrals	xix
Table 3	NUANCE level Muon reconstruction performance	xxiv
Table 4	Outcome of different simulation runs	xxv
Table 5	Neutrino oscillation parameters	17
Table 6	Magnetic Field Integrals	54
Table 7	Explanation of terms in Bethe Bloch formula	55
Table 8	Comparison of the two codes at $\cos \theta_{\mu}^{Gen} = 0.75$	70
Table 9	NUANCE generated Muon reconstruction performance	71
Table 10	Hadron Hit energy calibration table for no. of hits $\in [31, 35]$	73
Table 11	Event selection results with trial and error	79
Table 12	Event selection results with multivariate techniques	81
Table 13	Event Sample for oscillation analysis	89

---

LIST OF FIGURES

---

Figure 1	(a) Mixing between $\nu$ flavors and mass states, (b) $\nu$ oscillation	xv
Figure 2	$\nu$ MH ambiguity	xv
Figure 3	(a) ICAL detector geometry and (b) Magnetic field map shown in central module. The same field pattern exists in side modules as well.	xvi
Figure 4	(a) Reconstructed momentum distribution for $P_{\mu}^{Gen} = 5$ GeV/c and (b) systematic mean shift in momentum reconstruction	xvii
Figure 5	(a) Track split in dead space (b) charge identification efficiency	xvii
Figure 6	(a) Tasks to perform in a small tracking step (b) tracking algorithm	xx
Figure 7	Comparison between old (red) and the new (blue) Kalman filters: reconstructed (a) momentum plot (b) $\cos \theta$ plot - for 5000 $\mu^{-}$ events with $P_{\mu}^{Gen} = 5$ GeV/c and $\cos \theta_{\mu}^{Gen} = 0.95$	xxi
Figure 8	(a) $\chi^2/\text{ndof}$ plot for events with $P_{\mu}^{Gen} = 6$ GeV/c and $\cos \theta_{\mu}^{Gen} = 0.95$ ; (b) charge identification efficiency for $\mu^{-}$ (continuous line) and for $\mu^{+}$ (broken line) over wide $P_{\mu}^{Gen} - \cos \theta_{\mu}^{Gen}$ input range.	xxi
Figure 9	The stages of pattern recognition algorithm	xxiii
Figure 10	(a) Genuine $\mu$ fraction in hits tagged as ‘muon hits’ (b) genuine $\mu$ contamination in hits tagged as ‘hadron hits’	xxiii
Figure 11	(a) Background separation with $\frac{N^{-}-N^{+}}{N^{-}+N^{+}}$ in training phase (b) application of BDT to a general sample of data	xxiv
Figure 3.1	$\beta$ decay electron energy spectrum	3
Figure 3.2	Fundamental building blocks of nature	4
Figure 3.3	(a) Neutrino spectrum of the sun for different solar reaction channels (b) Ray Davis’s experimental setup at Homestake mine. Figure taken from [1].	5
Figure 3.4	(a) Giant cylindrical tank at Super Kamiokande and a prospective event (b) Construction of heavy water Cherenkov detector at Sudbury neutrino observatory	7
Figure 3.5	Super Kamiokande: $\nu_{\mu}$ deficit	8
Figure 3.6	$L/E$ dependence of neutrino survival probability. Figure adopted from [1]	10
Figure 3.7	Three neutrino flavor mixing	11
Figure 3.8	$\nu$ mass hierarchy problem	18
Figure 4.1	ICAL detector and its window to atmospheric neutrinos	20
Figure 4.2	Atmospheric neutrino and cosmic muon generation in atmosphere	21

Figure 4.3	Atmospheric neutrino flux at proposed INO site. Dependence on $\cos \theta$ for (a) $E = 1$ GeV, (b) $E = 3.2$ GeV and (c) $E = 10$ GeV. Figure taken from [2]	22
Figure 4.4	(a) Layout of ICAL detector and (b) local view of the stack of iron plate and RPC detectors	22
Figure 4.5	ICAL detector and its window to atmospheric neutrinos	23
Figure 4.6	(a) Structural view of an RPC (b) Cross sectional view. Figures adopted from [3], [4]	24
Figure 4.7	(a) ionization due to passage of high energy particle, (b) initiation of an avalanche, (c) electrons reach the anode much faster than the ions could reach cathode, due to higher drift speed, (d) charges in the resistive layer influence the field in a small area around the position where the avalanche is developed	24
Figure 4.8	(a) Slots for current coils in ICAL detector (b) One module of ICAL with coil inserted. Figures adopted from [5]	25
Figure 5.1	(a) Schematic diagram of ICAL detector, (b) Cross sectional view of RPC detector	28
Figure 5.2	ICAL inhomogeneous magnetic field map	29
Figure 5.3	ICAL GEANT4 simulation flow chart	30
Figure 6.1	Muon track and hadron shower of a typical NUANCE event	34
Figure 6.2	formation of (a) Hits and Clusters and (b) Triplets	35
Figure 6.3	formation of (a) Hits and Clusters and (b) Triplets	36
Figure 6.4	Muon track and hadron shower of a typical NUANCE event	37
Figure 6.5	(a) Distribution of neutrinos/muons in $P - \cos \theta$ plane and (b) fractional momentum delivered to muons vs incident neutrino momentum	40
Figure 6.6	(a) No. of final state particles, produced in the neutrino interactions, shown as a function of $P_\nu$ and $\cos \theta_\nu$ , (b) no. of hits in the detector generated by these particles.	41
Figure 6.7	Performance of the pattern recognition program: (a) degree of correct identification of muon hits in a muon track and (b) fraction of incorrect inclusion of muon hits in hadron shower	42
Figure 6.8	Residuals distributions of (a) $X$ , (b) $Y$ , (c) $t_x$ , (d) $t_y$ .	43
Figure 7.1	Qualitative view of Kalman filtering and smoothing procedure	46
Figure 7.2	(a) Schematic diagram of a track and (b) tracking steps between RPC planes	51
Figure 7.3	effect of multiple scattering on a track	58
Figure 7.4	Reconstructed muon of momentum 6 GeV/c at zenith angle $18.2^\circ$ ( $\cos \theta = 0.95$ ). Pull Distributions: (a) $X$ , (b) $Y$ , (c) $t_x$ , (d) $t_y$ , (e) $\frac{q}{P}$ and (f) $\chi^2/\text{ndof}$ distribution	62
Figure 7.5	(a) Distribution of hits, (b) p-value distribution @ $P_\mu = 6$ GeV/c at $\cos \theta_\mu = 0.95$	63
Figure 7.6	(a) p-value vs $\chi^2/\text{ndof}$ plot, (b) p-value distribution @ $P_\mu = 10$ GeV/c at $\cos \theta_\mu = 0.95$	64
Figure 7.7	Variation of Mean and Sigma of q/P Pull Distribution	64

Figure 7.8	(a) Correlation of the directions between incoming neutrino and outgoing muon (b) accuracy of reconstructed zenith angle for various $P_\mu^{Gen} - \cos \theta_\mu^{Gen}$ values	65
Figure 7.9	(a) Mean shift in the reconstructed momentum distribution and (b) Charge identification efficiency in % for reconstructed events at various $P_\mu - \cos \theta_\mu$ values	65
Figure 7.10	Reconstructed (a) momentum resolution plot and (b) $\cos \theta$ resolution plot	67
Figure 7.11	(a) A track split near the border of two RPCs at $x = 12$ m and (b) % of split events at different $P_\mu^{Gen} - \cos \theta_\mu^{Gen}$	68
Figure 7.12	Comparison of (a) $P_{rec}$ (b) $\cos \theta_{rec}$ distributions for $P_\mu^{Gen} = 5$ GeV/c and $\cos \theta_\mu^{Gen} = 0.95$	69
Figure 7.13	(a) $P_\mu^{Gen} - \cos \theta_\mu^{Gen}$ spectrum of reconstructed (black) and not reconstructed (red) events, (b) a surface plot of reconstructed events to express the relative abundance of events in $P_\mu^{Gen} - \cos \theta_\mu^{Gen}$ plane	71
Figure 7.14	(a) ‘Hadron’ hit-hadron energy calibration plot when no. of ‘hadron’ hits = 31, (b) corresponding hadron energy generation by ROOT based Vavilov random no. generator	72
Figure 7.15	Flow chart for InoPatternRecognition class	74
Figure 7.16	Flow chart for InoTrackFitAlg class	75
Figure 8.1	Training plots for (a) chi square probability, (b) vertex $y$ position, (c) error in $q/p$ element of the state vector and (d) $\frac{N^- - N^+}{N^- + N^+}$	80
Figure 8.2	Separation of signal like events and background like events by multivariate techniques: (a) BDT method (b) ANN method	80
Figure 8.3	Plots for (a) fractional error in momentum and (b) error in $\cos \theta$ estimation, for events that survive multivariate techniques based event selection criteria.	81
Figure 9.1	plan for $\nu$ mass hierarchy sensitivity analysis	86
Figure 9.2	Difference of neutrino oscillation probabilities for NH ( $\Delta_{31} > 0$ ) and for IH ( $\Delta_{31} < 0$ ) for two values of baselines $L$ . Thus, $N_{ij}^{pred}$ at every $ij^{th}$ bin is different depending on whether calculated based on NH or IH. The figure is adopted from [6]	87
Figure 9.3	Distribution of events in $q \times P_\mu - \cos \theta_\mu$ plane	88
Figure 9.4	Overlapped distributions of $\chi_{true}^2$ and $\chi_{false}^2$	89
Figure 9.5	$\nu$ mass hierarchy sensitivity plot of ICAL experiment, assuming NH as the true hierarchy	90
Figure 10.1	$\delta(dl)$ Correction	93

---

SYNOPSIS OF THE DOCTORAL WORKS

---

---

SYNOPSIS

---

## 1.1 INTRODUCTION

India-based Neutrino Observatory (INO) is an upcoming underground basic science project, funded by the Government of India, to study the properties of neutrino ( $\nu$ ), an extremely elusive fundamental particle. ICAL is a 50 kiloton magnetized Iron tracking **CAL**orimeter detector that will be used at INO for resolving the  $\nu$  mass hierarchy (called  $\nu$ MH hereafter) problem. About 30000 ( $2 \text{ m} \times 2 \text{ m}$ ) resistive plate chamber (RPC) detectors, with position resolution of the order of centimeter, will serve as the sensitive detectors of the giant ICAL detector ( $48 \text{ m} \times 16 \text{ m} \times 14.5 \text{ m}$ ), placed underground below the west Bodi Hills, near the city of Madurai (Tamil Nadu), in south India. Apart from the ICAL detector the cavern will also house the detectors for Neutrino-less Double Beta Decay (NDBD) experiment, Dark matter search experiment etc. The project is expected to initiate the trend of long term world class High Energy Physics experimental research in India.

One of the unsolved mysteries in neutrino physics is the hierarchy of the neutrino mass eigenstates. Neutrinos are produced as distinct neutrino flavors ( $\nu_e, \nu_\mu, \nu_\tau$ ) in the stars, earth atmosphere, supernovae etc. through weak interactions. Their propagation can be understood in terms of mixing among three mass eigenstates ( $\nu_1, \nu_2, \nu_3$ ), connected to the flavor states via a unitary matrix  $U_{PMNS}$  that is parametrized by the mixing angles [7]:

$$\begin{pmatrix} \nu_e \\ \nu_\mu \\ \nu_\tau \end{pmatrix} = \begin{pmatrix} c_{13} c_{12} & c_{13} s_{12} & s_{13} e^{-i\delta} \\ -c_{23} s_{12} - s_{13} s_{23} c_{12} e^{i\delta} & c_{23} c_{12} - s_{13} s_{23} s_{12} e^{i\delta} & c_{13} s_{23} \\ s_{23} s_{12} - s_{13} c_{23} c_{12} e^{i\delta} & -s_{23} c_{12} - s_{13} c_{23} s_{12} e^{i\delta} & c_{13} c_{23} \end{pmatrix} \begin{pmatrix} \nu_1 \\ \nu_2 \\ \nu_3 \end{pmatrix} \quad (1)$$

In Eq. (1),  $\delta$  denotes the  $CP$  violating phase and  $c_{ij} = \cos \theta_{ij}$  and  $s_{ij} = \sin \theta_{ij}$  -where the angle  $\theta_{ij}$  denotes the mixing angle ( $i, j \in [1, 2, 3]$ ).  $\theta_{ij}$  parametrize the mixing of the  $\nu$  flavor states with the  $\nu$  mass states (see Fig. 1.1(a)).

The mixing induces a non-zero probability of neutrino oscillation as neutrinos of energy  $E$  travel through some distance  $L$  (Fig. 1.1(b)). First indication of neutrino oscillation came from Ray Davis's solar neutrino experiment. Then, evidences of oscillation in atmospheric neutrinos were reported by Super Kamiokande collaboration in 1998 [8]. These observations were followed by the confirmations from the SNO and KamLAND teams, that the neutrino oscillation was the reason behind the solar neutrino deficit problem [9] that had baffled the physicists for past three decades.

These experimental findings established constraints on the allowed parameter space of three flavor neutrino oscillations ( $\theta_{13}, \theta_{23}, \theta_{12}, \Delta m_{21}^2, |\Delta m_{31}^2|$ ), where  $m_i$  represents the mass of the mass eigenstate  $\nu_i$ . The analysis of solar neutrino data unambiguously

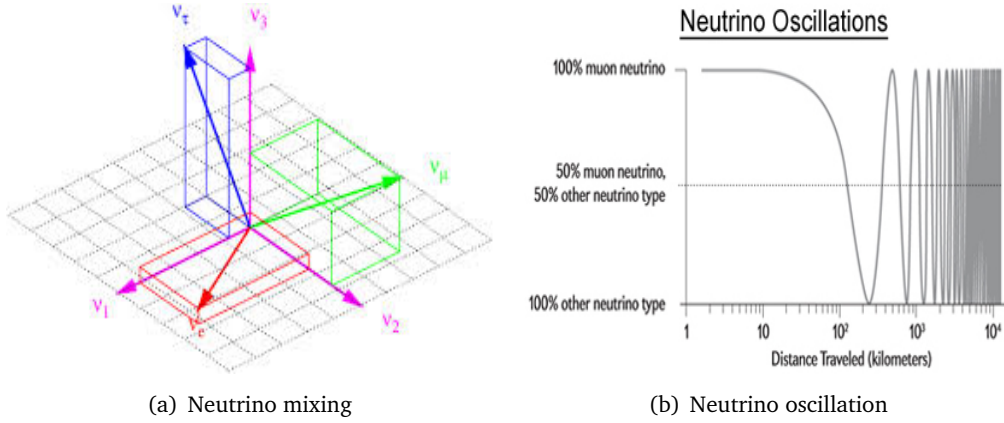


Figure 1.: (a) Mixing between  $\nu$  flavors and mass states, (b)  $\nu$  oscillation

predicted  $\Delta m_{21}^2 \equiv m_2^2 - m_1^2 > 0$  [10]. The allowed range of values and best-fit values [11] are shown in the table below.

Table 1.:  $\nu$  oscillation parameters

Parameter	Best fit	$3\sigma$ range
$\sin^2 \theta_{12}$	0.307	0.259-0.359
$\sin^2 \theta_{23}$	0.386	0.331-0.637
$\sin^2 \theta_{13}$	0.0241	0.0169-0.0313
$\Delta m_{21}^2$ (eV <sup>2</sup> )	$7.54 \times 10^{-5}$	$6.99-8.18 \times 10^{-5}$
$ \Delta m_{31}^2 $ (eV <sup>2</sup> )	$2.43 \times 10^{-3}$	$2.19-2.62 \times 10^{-3}$

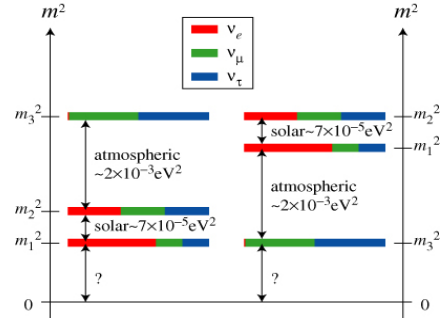


Figure 2.:  $\nu$ MH ambiguity

However, the sign of  $|\Delta m_{31}^2|$  being unknown, one cannot predict whether or not  $m_3 > m_1$ . This is the so-called  $\nu$ MH problem (Fig. 2) that ICAL detector at INO hopes to resolve. It will have access to the neutrinos ( $\nu$ ) and anti-neutrinos ( $\bar{\nu}$ ) coming through the core of the earth (up going neutrinos) and will be able to distinguish  $\nu$  from  $\bar{\nu}$  by observing the charge of the lepton produced in charged current (CC) neutrino interactions. Gandhi et al. have shown [6] that: at specific values of the baseline  $L$ , the oscillation patterns are different based on whether neutrinos follow Normal Hierarchy or Inverted Hierarchy. Hence, keen observation of neutrino oscillation pattern in ICAL can reveal the true hierarchy.

In the detector, only the secondary particles generated in neutrino interactions are observable and they carry the partial information about the neutrino energy and baseline. For this thesis, we have tried to develop the methods to extract the information, so as to carry out a  $\nu$ MH sensitivity analysis for ICAL detector for 10 years of operation.

## 1.2 PERSPECTIVE

ICAL detector is sensitive to muon neutrinos of momenta  $P_\nu > 0.8$  GeV/c. These neutrinos flood the detector from all possible directions, depending upon their points of production in the atmosphere. The oscillation baseline  $L$  ranges from a few tens of

kilometers (down-going neutrinos, produced up in the atmosphere at the experimental site), to about ten thousand kilometers (up-going neutrinos, produced in the atmosphere at a *place on earth*, diametrically opposite to the ICAL experimental site). Many of these neutrinos travel through the core of the earth before they arrive at the detector.

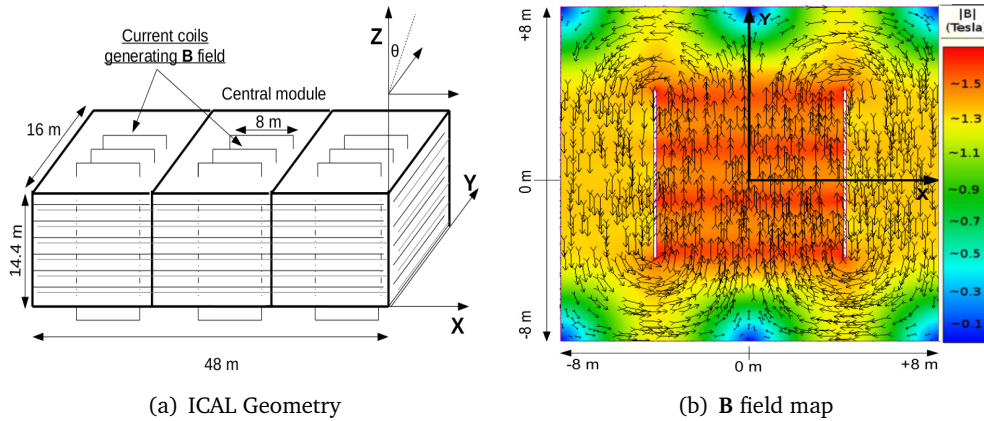


Figure 3.: (a) ICAL detector geometry and (b) Magnetic field map shown in central module. The same field pattern exists in side modules as well.

CC interactions of these neutrinos with the detector material produce muons ( $\mu^\pm$ ) and hadrons. Typically, these hadrons ( $\pi^{0,\pm}, p$ ) are absorbed within a few iron plates of the calorimeter. Muons being minimum ionizing particles, usually cross more number of sensitive RPC layers and hence, give clean longer tracks. Bethe Bloch ionization [12] is the dominant mode of energy loss by muons in this range of energy. The detector can distinguish between  $\mu^+$  and  $\mu^-$  tracks as it is equipped with magnetic field (Fig. 1.3(b)) operating through the iron plates.

To obtain some sensitivity to the neutrino oscillation, it is absolutely essential to reconstruct  $\mu^\pm$  momenta ( $P_\mu$ ) and directions ( $\theta_\mu$ ) with good accuracy and precision. Hadronic showers are not good for extracting information. Their total energy and direction can be calibrated with rather poor resolution [13]. Therefore, separation of muon track from hadrons, proper fitting of the track; and estimation of track parameters near neutrino event vertex are very important for the sake of the experiment.

### 1.3 TRACK FITTING WITH SINGLE MUON (GEANT4 MONTE CARLO)

In the thesis work, most emphasis has been given on revision and rectification of the algorithm for reconstruction of muons. This is done in two steps: (a) pattern recognition (track finding) and (b) track fitting. The former becomes of prime importance in the presence of other hadrons/electrons in the neutrino event. For track fitting and the extraction of track parameters (e.g. charge, momentum and direction), an extended Kalman filter was used. From the chronological perspective, the task of track fitting with Kalman filter was carried out first. It was done in three steps:- (a) validation of existing Kalman filter, (b) identifying the source of problems and (c) rectifying them. For this, single muon events were simulated in the detector by GEANT4, and signals generated in the sensitive detector (hits) were used for track fitting.

### 1.3.1 Validation of existing Kalman filter code

The problem is if a set of muons are simulated with known initial positions, directions, charge and momenta, then how good we can estimate such track parameters from the set of measurements (hits) in the detector. The performance of the reconstruction code was neither very accurate nor very precise, as can be seen from Fig. 1.4(a), where many events are found to get reconstructed with very poor estimation of input momentum ( $P_{\mu}^{Gen} = 5$  GeV/c). They crowd at the tails of the  $P_{rec}$  distribution and lead to less precision of

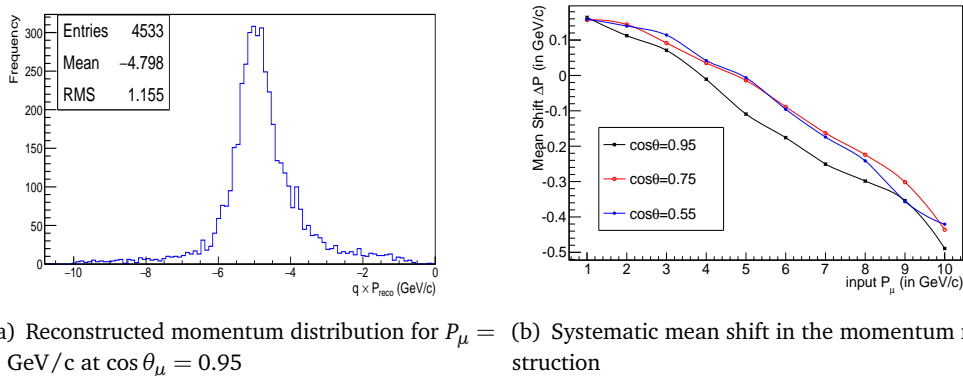


Figure 4.: (a) Reconstructed momentum distribution for  $P_{\mu}^{Gen} = 5$  GeV/c and (b) systematic mean shift in momentum reconstruction

estimation. The accuracy is also poor, since the mean of  $P_{rec}$  distribution comes at  $\sim 4.8$  GeV/c. In fact,  $(\langle P_{rec} \rangle - P_{\mu}^{Gen})$  decreases almost linearly, as we increase  $P_{\mu}^{Gen}$ , as shown in Fig. 1.4(b). The long tails in the reconstructed momentum distribution were due to those tracks, that were split into parts in the detector dead space (Fig. 1.5(a)). Every split tracklet was reconstructed individually and their fit parameters contributed to the poor reconstruction. Also, if we concentrate on the events with unbroken tracks, the

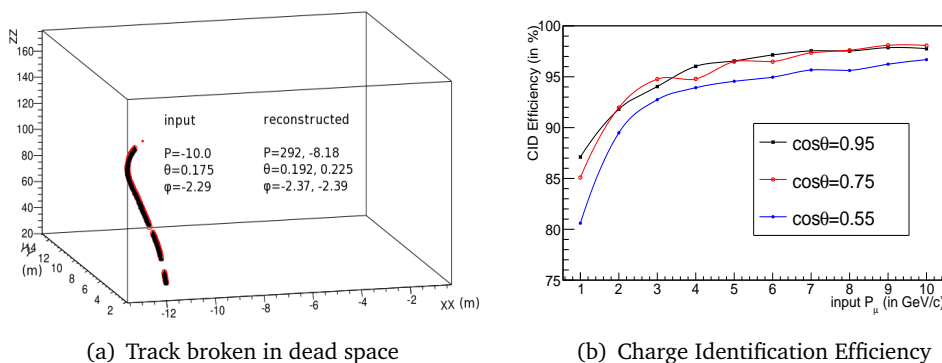


Figure 5.: (a) Track split in dead space (b) charge identification efficiency

charge identification efficiency is not so competitive, which must be the case as we want to make full use of the charge distinguishing capability of ICAL.

### 1.3.2 Identifying the source of problems

The following problems resulting in poor performance of track fitting code were identified:

- (a) Poor reconstruction efficiency and poor charge identification efficiency at lower  $P_\mu$  ( $< 1\text{GeV}/c$ ) and higher zenith angle  $\theta_\mu$  ( $> 50^\circ$ ).
- (b) Poor accuracy and precision of the momentum estimation.
- (c) Splitting of high energy tracks passing through vertical dead spaces.
- (d) Wrong directional information in some cases.

The first two issues were direct consequences of poor extrapolation and filtering algorithms of the existing Kalman filter. The filter was designed to fit tracks perpendicular to the active planes of the calorimeter (as happens with accelerator based experiments like MINOS [14]). Track extrapolation was done with the *swimswimmer* package, which worked in a transformed coordinate system where magnetic field has only  $B_z$  component. In each tracking step, the field was taken to be constant and next point in the track was predicted using the helix equations [15]. This package was known to produce worse results at lower momenta [16]. Kalman convergence also critically depend on the accurate error propagation matrix of fit parameters. If  $f(\mathbf{x})$  denotes the extrapolation routine, the error propagation matrix goes as  $\frac{\partial f}{\partial \mathbf{x}}$ . In this filter, a simplified propagator matrix [14], not self-adaptable to possible tracking conditions, was used. The error propagation between any two RPC planes containing measurements was done directly, neglecting the possible variation in the magnetic field. Also, while implementing the multiple scattering matrix in the Kalman filter, constant value of magnetic field was put by mistake. Situations such as these resulted in the poor performance for single muon cases only.

### 1.3.3 Improvements in track reconstruction

We started with usual track parameters  $\mathbf{x} = (x(z), y(z), t_x(z), t_y(z), q/p(z))$  and attempted to revise and rectify the whole track fitting program. Here  $t_x (= dx/dz)$  and  $t_y (= dy/dz)$  are two angle parameters related to angles  $\theta$  and  $\phi$  as  $\cos \theta = 1/\sqrt{1+t_x^2+t_y^2}$  and  $\tan \phi = t_y/t_x$ . Given the state vector at  $(x(z_0), y(z_0), z_0)$ , we obtained the formula to find the state vector at a point  $(x(z_0+dz), y(z_0+dz), z_0+dz)$  in the track [17] in the inhomogeneous magnetic field  $\mathbf{B}(x, y, z)$ , using an analytic iterative formula [18]. These formulae, used instead of *swimswimmer* package, are given below:

$$\begin{aligned} x(z_0+dz) = & x(z_0) + t_x dz + h(t_x t_y S_x - (1+t_x^2)S_y) + h^2[t_x(3t_y^2+1)S_{xx} \\ & - t_y(3t_x^2+1)S_{xy} - t_y(3t_x^2+1)S_{yx} + t_x(3t_x^2+3)S_{yy}] \end{aligned} \quad (2)$$

$$\begin{aligned} y(z_0+dz) = & y(z_0) + t_y dz + h((1+t_y^2)S_x - t_x t_y S_y) + h^2[t_y(3t_x^2+3)S_{xx} \\ & - t_x(3t_y^2+1)S_{xy} - t_x(3t_y^2+1)S_{yx} + t_y(3t_x^2+1)S_{yy}] \end{aligned} \quad (3)$$

$$\begin{aligned} t_x(z_0+dz) = & t_x + h(t_x t_y R_x - (1+t_x^2)R_y) + h^2[t_x(3t_y^2+1)R_{xx} \\ & - t_y(3t_x^2+1)R_{xy} - t_y(3t_x^2+1)R_{yx} + t_x(3t_x^2+3)R_{yy}] \end{aligned} \quad (4)$$

$$t_y(z_o + dz) = t_y + h \left( (1 + t_y^2)R_x - t_x t_y R_y \right) + h^2 [t_y(3t_y^2 + 3)R_{xx} - t_x(3t_y^2 + 1)R_{xy} - t_x(3t_y^2 + 1)R_{yx} + t_y(3t_x^2 + 1)R_{yy}] \quad (5)$$

Here  $h = \kappa(q/P)\sqrt{1 + t_x^2 + t_y^2}$  (with  $\kappa = 0.29979 \text{ GeVc}^{-1}\text{T}^{-1}\text{m}^{-1}$ ) and in the RHS of Eq.(2)-(5),  $t_x = t_x(z_o)$  and  $t_y = t_y(z_o)$ .  $S_{\dots}$  and  $R_{\dots}$  denote magnetic field integrals [18], shown in table 2. The field integrals  $S_{\dots}$  and  $R_{\dots}$  were evaluated assuming

$S_x$	$S_y$	$S_{xx}$	$S_{xy}$	$S_{yx}$	$S_{yy}$
$\frac{1}{2}B_x dz^2$	$\frac{1}{2}B_y dz^2$	$\frac{1}{6}B_x^2 dz^3$	$\frac{1}{6}B_x B_y dz^3$	$\frac{1}{6}B_x B_y dz^3$	$\frac{1}{6}B_y^2 dz^3$
$R_x$	$R_y$	$R_{xx}$	$R_{xy}$	$R_{yx}$	$R_{yy}$
$B_x dz$	$B_y dz$	$\frac{1}{2}B_x^2 dz^2$	$\frac{1}{2}B_x B_y dz^2$	$\frac{1}{2}B_x B_y dz^2$	$\frac{1}{2}B_y^2 dz^2$

Table 2.: Magnetic Field Integrals

that  $B_i(x(z), y(z))$  vary too slowly along the track  $(x_{particle}(z), y_{particle}(z))$  and might be assumed to be constant when integrating with respect to  $z$ . This is correct, unless the particle is traversing almost parallel to the detector plane ( $\theta \approx 90^\circ$ ). Using the state extrapolation formula  $f$ , expressed through Eq.(2)-(5), we calculated the corresponding rows of the Kalman propagator matrix [17]. This propagator is sensitive to local values of  $t_x, t_y, q/p$  and magnetic field and thus, can propagate the errors in a proper way.

We also incorporated the detector structure information in the track fitting routine. Energy losses in each separate material were accounted for using the Bethe Bloch formula (with density correction terms). For accurate convergence of  $q/p$  in Kalman filter, accurate calculation of the term  $\frac{\partial(\frac{q}{p})_{l+dl}}{\partial(\frac{q}{p})_l}$  in each material is very crucial. So, we obtained the CSDA range vs momentum tables [19] for all dense materials (iron, copper, aluminum, graphite and glass) having density  $> 1.5 \text{ g/cc}$ . The row for error propagation in  $q/p$  in the propagator matrix was calculated considering the fact that in ICAL, the tracks are not perpendicular to the sensitive detector (RPC) planes. Here we made generalization of the formalisms found in the existing literature [20].

The error propagation was done by the equation  $\tilde{C} = F\hat{C}F^T + Q$ , where the first term denotes the systematic error propagation (coming of magnetic field, energy loss etc) and the second term  $Q$  gives the error introduced by random process noise (like, multiple scattering).  $C$  refers to the ‘estimation error covariance matrix’. The filter equations [15] were applied whenever a measurement was available to compare with the prediction (obtained from Eq.(2)- (5)). A Kalman gain  $K$  matrix was calculated; it effectively decides whether to give more importance to the measurement or to the prediction. The application would shrink the error and give a near optimal estimate of the state at  $(x(z_o + dz), y(z_o + dz), z_o + dz)$ .

State extrapolation  $\tilde{\mathbf{x}} = f(\hat{\mathbf{x}})$  was done in each small tracking steps repeatedly taking into account nearby material boundaries. Along with that the error propagation was also done repeatedly. The whole chain of tracking can be shown as in Fig. 1.6(a) and 1.6(b):

We included the random noise matrix  $Q$  (equipped with thick scatterer approximation) to facilitate the filtering process. Here also, material dependent variance formulae [21] were used. Whereas previous track fitting works in ICAL [22] had made use of Highland formula [23] to account for multiple scattering, we chose to use the formula calculated

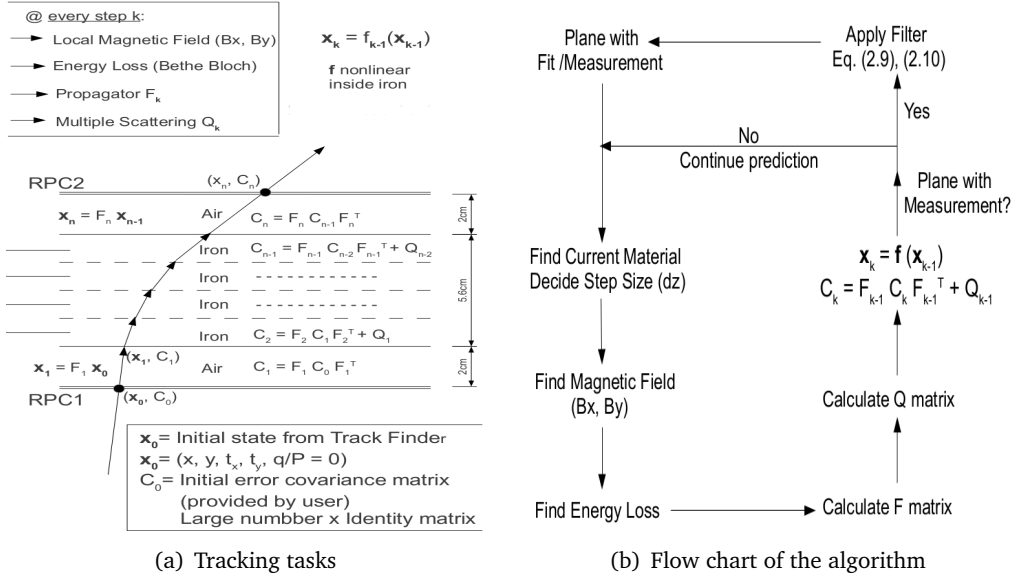


Figure 6.: (a) Tasks to perform in a small tracking step (b) tracking algorithm

in more recent literature [24], to keep the accounted random error independent of the choice of the size of the tracking step  $d$ . The formula is:

$$\langle \theta_{ms}^2 \rangle = \frac{225 \times 10^{-6} d}{\beta^2 p^2 X_s} \quad (6)$$

-where  $X_s$  is related to the radiation length of the material.

The variance  $\sigma^2(q/p)$  and other covariance terms like  $cov(q/p, t_x)$  etc. were calculated by implementing the Urban model [25]. Essentially, this gives the value of  $\sigma^2(E)$  of a Landau distribution truncated beyond an upper limit. Other formulae, previously used in track fitting context, are insensitive to the  $Z$  of the materials which is why we did not use them.

After all the hits in the muon track candidate have been filtered, the hits are processed in the reverse order using the same algorithm. This procedure ‘smooths’ the fitted track. The processing of hits in the forward and backward directions, completes one iteration. We have used four iterations, though for  $> 90\%$  cases, the fractional change in the desired state vector estimate were seen to become  $< 10\%$  after the 2nd iteration. For tracks with only 4–5 hits convergence was not at all achieved after four iterations.

### 1.3.4 Track element merging

Since, it is highly unlikely to have two separate atmospheric neutrino events occurring at the same position in the detector simultaneously, no great harm is anticipated if we merge the two tracklets appearing in an event; possibly they are *not coming* from different events. From rear terminal of one tracklet we extrapolated using  $f(\hat{\mathbf{x}})$  to the vertex terminal of the other tracklet. We ensured a relatively relaxed condition, that allowed almost every such pairs to get merged. When that happened, we fitted the whole merged track as a single event. This improved our efficiency and that did not get worse when we worked with NUANCE data.

### 1.3.5 Results

After implementing the new algorithm and fixing the issue of the broken tracks, we had considerable improvements in the accuracy and precision in the estimation of track parameters. This is seen from the Fig. 1.7(a) and 1.7(b), where reconstructed estimates of a set of muons with  $P_\mu^{Gen} = 5 \text{ GeV}/c$  and  $\cos\theta_\mu^{Gen} = 0.95$  are shown. Other quality

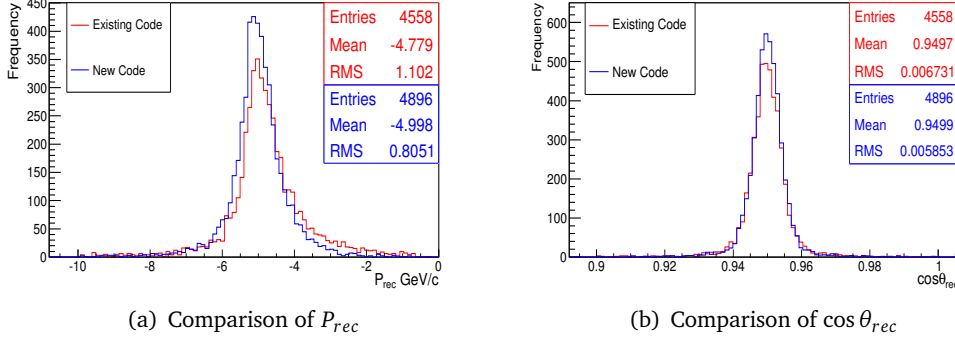


Figure 7.: Comparison between old (red) and the new (blue) Kalman filters: reconstructed (a) momentum plot (b)  $\cos\theta$  plot - for 5000  $\mu^-$  events with  $P_\mu^{Gen} = 5 \text{ GeV}/c$  and  $\cos\theta_\mu^{Gen} = 0.95$

control tests, such as having positive diagonal elements of covariance matrix in *all* calculations, having greater fit errors at the rear end of the track than at the vertex end of it etc. checked out fine. In Fig. 1.8(a), we show the reduced  $\chi^2$  plot that has a mean around unity, close to our expectation. Similar trend was seen to follow in most other  $P_\mu^{Gen} - \cos\theta_\mu^{Gen}$  input configurations. Charge identification efficiency (Fig. 1.8(b)) also improved compared to existing filter (Fig. 1.5(b)). Hence, this filter was employed in the

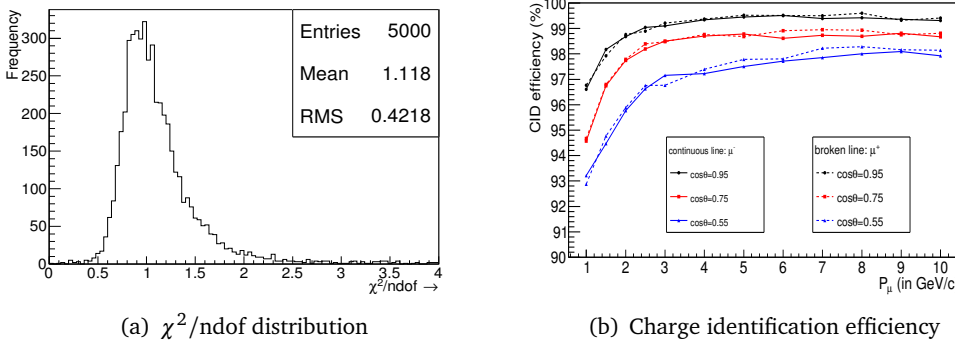


Figure 8.: (a)  $\chi^2/\text{ndof}$  plot for events with  $P_\mu^{Gen} = 6 \text{ GeV}/c$  and  $\cos\theta_\mu^{Gen} = 0.95$ ; (b) charge identification efficiency for  $\mu^-$  (continuous line) and for  $\mu^+$  (broken line) over wide  $P_\mu^{Gen} - \cos\theta_\mu^{Gen}$  input range.

official version of ICAL code released in 2013. A more detailed account of the algorithm can be found in our publication [17], where I served as the corresponding author.

## 1.4 A MORE REALISTIC APPROACH TO MH ANALYSIS

The improvement in the Kalman filter, shown in the previous section, was the first step towards the  $\nu$ MH sensitivity analysis with reconstructed NUANCE data. With this code, NUANCE neutrino events were reconstructed and hence, the sensitivity was found. All previous attempts [26–28] of obtaining mass hierarchy sensitivity were based on various kinds of approximations and indirect methods that were removed in this analysis. For example, Ghosh et al. [27] tabulated the muon response of the detector, estimated from the reconstruction of *GEANT4 level single* muons in the central region of the central module of the detector that is equipped with the homogeneous magnetic field. They did not consider the deteriorations caused by (a) the presence of hadrons in every event and (b) the region with sharply changing magnetic fields. Similarly, Devi et al. [28] obtained an enhanced sensitivity, on the assumption that *muon hits and hadron hits can be 100% separated in the detector*, apart from the earlier assumptions. Statistical fluctuations of the data were also not considered in these analyses. This work is independent of such assumptions. The whole analysis is divided into three steps: (a) construction of the pattern recognition (track finding) program, (b) event selection and (c) final  $\nu$ MH sensitivity analysis. The oscillation analysis program used in [27] was also used for this work.

### 1.4.1 Pattern recognition program

The presence of variable number of hadron hits in an event and their locations relative to the muon track greatly influences the performance of track fitting. If all the genuine muon hits of the muon track are not included, the Kalman filter program is forced to find the curvature from insufficient number of measurements. Situations become worse if few hadron hits are included in the muon track reconstruction, by mistake (as these hits are identical in all respects). The track finder code, used hitherto, was not good at separating muons and hadrons. So, this task was performed as a part of this thesis work.

All hits with maximum difference of 1 ns between  $x$  strip-timing and  $y$  strip-timing were taken into consideration. All the layers with  $> 4$  hits were separated and were called as the *shower planes*. In few events, typical *shower planes* contained hundreds of hits, in form of a shower. The separation procedure removed most of the hadron hits if the number of *shower planes* in an event was nonzero. Hits in all the other planes were checked for possible clustering, depending on their mutual proximity. No hit in the same plane was counted twice. After this we deal with all the clusters in all the planes. All possible clusters in each set of nearby planes were checked to test if a *triplet* can be formed. A *triplet* is a set of three clusters (in three nearby planes) which when joined, look like almost a straight line ( $15^\circ$  of divergence was allowed). It is the unit of formation of an InoTrackSegment. Next, the nearby *triplets* were tested for association and chains of *triplets* were formed. Usually, only one such chain resulted and this was termed as an InoTrack.

The algorithm is illustrated through Fig. 9, where the formation of a muon track is shown. If more than one chains were found, the longest one was considered. This InoTrack represented the *muon* track if it had at least 6 hits; only then, the event was further processed. Otherwise, the event was discarded as it was not clear whether at all the track came from a muon or not. All those hits in the InoTrack were used to find the

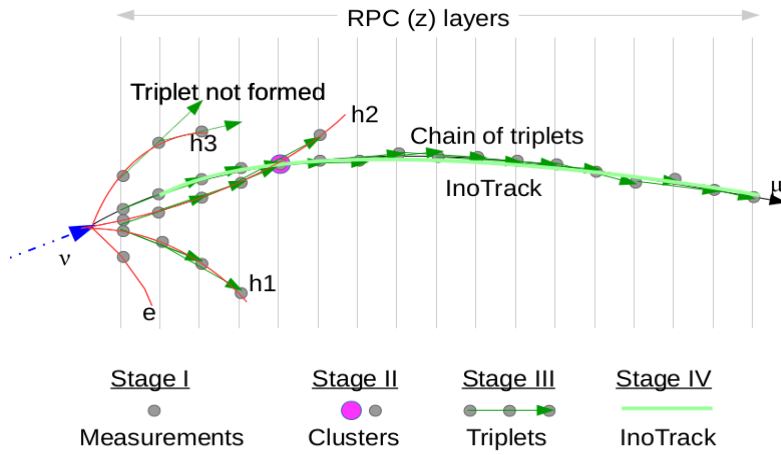


Figure 9.: The stages of pattern recognition algorithm

direction of the track (i.e. if the muon was up-going or down-going). As compared to the earlier track finder code, where in  $\sim 87\%$  cases the directions of the muons were correctly found, the present work gave correct direction in  $\sim 96\%$  cases. The efficiencies

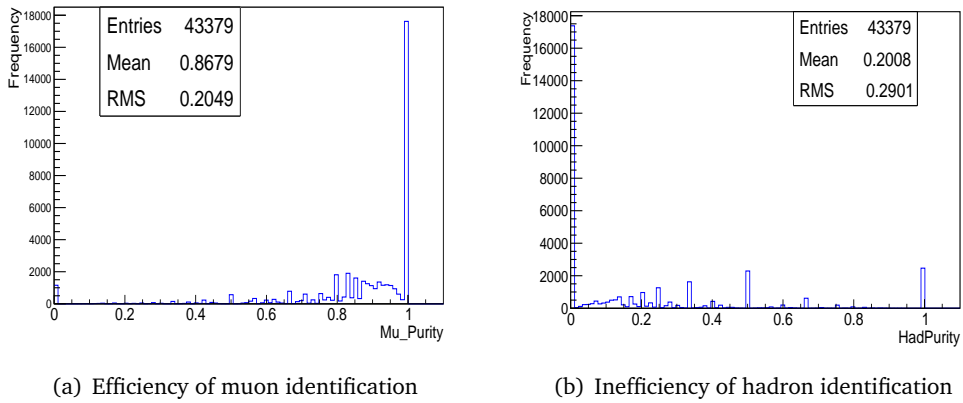


Figure 10.: (a) Genuine  $\mu$  fraction in hits tagged as ‘muon hits’ (b) genuine  $\mu$  contamination in hits tagged as ‘hadron hits’

of identification of muon hits and hadron hits were also quantified for the first time (in INO). We show these information in Fig. 1.11(a) and Fig. 1.11(b).

#### 1.4.1.1 Track fitting performance for NUANCE data

After implementing these, NUANCE neutrino event data were reconstructed. The results are shown below. The poor performance even with the new reconstruction code reflects the realistic detector response of ICAL as of now. The effective resolution worsens as most events are at higher  $\theta$ .

Parameter	previously	currently
Reconstruction efficiency	38%(50%)	40%
Charge identification efficiency	74%	89%
Directionality (up/down)	83%-87%	95%-96%
% Events of $p < 10\%$ accuracy	20%-23%	31%-33%

Table 3.: NUANCE level Muon reconstruction performance

#### 1.4.2 Event selection

The next step toward performing the  $\nu$ MH analysis is to select the events that are reconstructed better in the detector. Several trial and error methods were attempted that used cuts on the no. of hits, reduced chi square, zenith angle etc. These produced a set of good events through the reduction in the no. of events. That posed a great problem as the no. of events in each of the  $P_\mu - \cos \theta_\mu$  bin of the analysis would go very low. Hence, we resorted to a TMVA based analysis, which gave us relatively better performance. In the trial and error method to reject one bad event with incorrect charge id, we had to loose 6 – 15 events with correct charge id, depending on the cuts used. Use of Adaptive Neural Network and Boosted Decision Tree gave a better ratio: 1 wrong

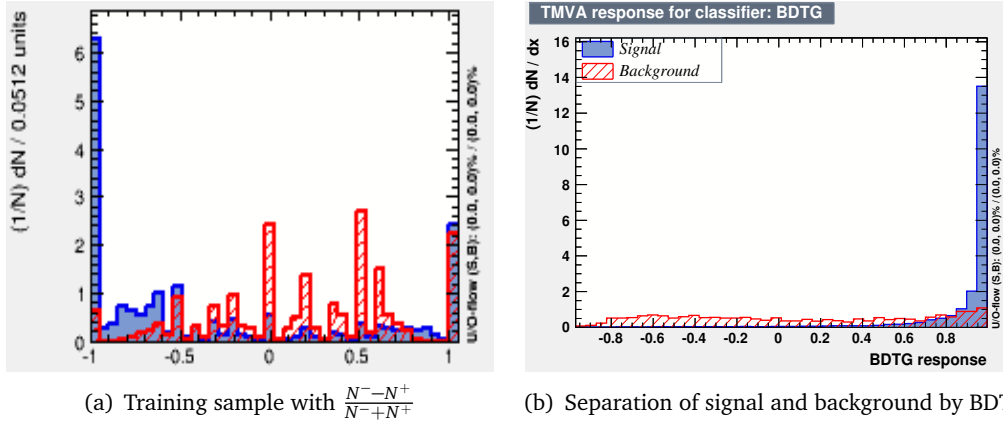


Figure 11.: (a) Background separation with  $\frac{N^- - N^+}{N^- + N^+}$  in training phase (b) application of BDT to a general sample of data

charge id. event for 2 – 3 correct charge id. events. The following variables were used to train the population and discriminate between the general set of reconstructed data (a)  $y$  position of the event vertex ( $|y| > 6$  m means fringing magnetic field), (b)  $p$ -value of the  $\chi^2$  distribution, (c) relative occurrence of the hadron hits in an event, (d) fit error in  $q/p$  at the vertex end and at the rear end and (e) the quantity  $\frac{N^- - N^+}{N^- + N^+}$ , where  $N = N^- + N^+$  is the total no. of hits,  $N^{+(-)}$  is the no. of fit-sites with +ve(-ve) sign measurement by Kalman filter.

The use of TMVA lead to survival of  $\sim 75\%$  of total number of reconstructed events and they had  $\sim 98.5\%$  charge identification efficiency. About 40% of these events had their momenta found within 10% accuracy.

### 1.4.3 $\nu$ MH sensitivity analysis

The neutrino oscillation analysis code used for the previous works [27] was used for the current fixed parameter analysis for obtaining the  $\nu$ MH sensitivity. Apart from the detector response, the following important changes were implemented: (a) statistical fluctuations were taken into account and (b) integer number of events in every bin were considered.

The data set were simulated assuming that normal hierarchy is the true hierarchy using the best fit parameters, as shown in table 6.3.3. The mean of the fit  $\chi^2$  with the wrong model (i.e. the inverted hierarchy) is more than the mean of the fit  $\chi^2$  with the correct model (i.e. the normal hierarchy). If these two mean chi squares are called as  $\langle\chi_{false}^2\rangle$  and  $\langle\chi_{true}^2\rangle$  then the sensitivity of ruling out the wrong hierarchy is seen to be  $\sim \sqrt{\langle\chi_{false}^2\rangle - \langle\chi_{true}^2\rangle}$ .

The analysis was carried out for 10 years of exposure for 50 kton ICAL detector. We took 9 bins of energy between [0.1 – 50] GeV and 45 non uniform  $\cos\theta$  bins between  $[-1, +1]$ . We found that  $\sim 95\%$  of the  $\mu^-$  bins and  $\sim 88\%$  of the  $\mu^+$  bins have at least an event.

Previous works were based on functional smearing of NUANCE level muon data with tabulated values of detector efficiency, resolution etc. A consequence of this is  $\chi_{true}^2 = 0$ , an assumption that is removed in the current work. Also, 1000 kiloton-years of observed data were scaled down to 10 years in this analysis, which resulted in fractional number of observed events in every bin. Such idealizations were removed in the current analysis. The table below shows the outcomes of different runs of the program.

Number of $\mu^-$	Number of $\mu^+$	Total	$\chi_{false}^2$	$\chi_{true}^2$	$\Delta\chi^2$
5848	1567	7415	846.155	841.865	4.290
5781	1494	7275	840.287	837.229	3.058
5725	1533	7258	900.497	909.839	2.602
5851	1505	7356	833.540	823.924	9.616
5824	1555	7379	822.628	816.201	6.427

Table 4.: Outcome of different simulation runs

Hence, the  $\Delta\chi^2$  of the  $\nu$ MH sensitivity of the detector for ten years of exposure was found to be  $\Delta\chi^2 \sim 4.5$ . This is less compared to the results reported by Ghosh et al [27] who obtained  $\Delta\chi^2 \sim 7.0$ . The deterioration is expected as more realistic detector effects were considered in this analysis.

## 1.5 SCOPE OF IMPROVEMENTS

There are two possible directions of improvement for obtaining a better sensitivity. First, one can try to implement Kalman smoothing algorithm to ‘smooth’ the fitted track. In principle, this should give better charge identification efficiency and better momentum resolution, as the fitted track is more ‘smooth’ now, for one to estimate the curvature. It is also important to single out the events that are coming out or going into the detector dead spaces. We have already implemented a method to do this, but the conditions need optimization.

Secondly, the binned  $\chi^2$  analysis has a serious problem. The current oscillation analysis code is written in such a way that only rectangular bins in  $P_\mu - \cos \theta_\mu$  plane are possible to house the selected  $\mu^-$  and  $\mu^+$  events. A flexible algorithm is required to accommodate  $\mu^-$  and  $\mu^+$  according to their relative prevalence. Not only that, a polar binning scheme might be tried  $(r, \alpha) = f(P_\mu, \cos \theta_\mu)$  so that almost equal numbers of events can be made to reside in every bin. A typical choice of the polar equations might be:  $r = \sqrt{P_\mu^2 + \cos^2 \theta_\mu}$  and  $\tan \alpha = \frac{\cos \theta_\mu}{P_\mu}$ , but this is subject to further studies.

Implementation of these might improve the projected  $\nu$ MH sensitivity of ICAL detector. But it is difficult to predict by what amount the sensitivity will get better.

## 1.6 ACKNOWLEDGEMENTS

I am grateful to Dr. Wolfgang Wittek, whose help was invaluable in implementing the  $\frac{\partial (\frac{q}{p})_{l+d}}{\partial (\frac{q}{p})_l}$  in the propagator matrix of the Kalman filter. Also, I am indebted to Tarak, Ram and Vipin for their valuable suggestions and helps at various moments.

Part I.

Neutrino Physics and  
Perspective of INO-ICAL

---

## THESIS INTRODUCTION

---

### 2.1 INTRODUCTION

The quest for unification of fundamental interactions in physics has intrigued the best physicists almost for two hundred years. The journey started with Faraday and Maxwell's efforts on the unification of electricity and magnetism and the identification of light as an electromagnetic wave. Their works established the base of the modern day physical theories. Subsequent groundbreaking contributions from Einstein, Planck, Rutherford, Heisenberg, Schrödinger, Dirac, Pauli and Feynman made physics reach the height that has never been achieved before. Relativity and quantum mechanics discovered by these great scientists changed our views of nature and its laws in a permanent basis. Not only they helped us understand the nature in a better fashion, also they gave birth to several other pertinent questions. Answering these required advent of standard model of particle physics along with modern experimental techniques. The technological growth has been immense in last fifty years, due to the improvement of particle accelerators and detectors in high energy physics experiments. Today most of the predictions of the standard model of particle physics, that attempts to understand *all* known interactions except gravity, have been verified to extremely good accuracy. The final missing link of the theory was the discovery of the Higgs boson that supposedly endows all fundamental particles with masses. In July 2012, CMS and ATLAS collaboration from Large Hadron Collider discovered a boson state that resembles the standard model Higgs boson within experimental limits. It is really great to be present at this historical landmark of physics.

However, the quest towards a theory of everything has not stopped. Although the standard model is known to be correct to a high degree of accuracy, the particle physicists know already that it does not provide the complete picture. It cannot answer why there exist exactly three generations of quarks and leptons, how to fit gravity in the framework of particle physics etc. It also cannot explain the neutrino mixing and oscillation.

In fact, in present times, neutrinos are the only probes for the physics beyond standard model. Standard model of particle physics assumes the neutrinos to be massless. However, neutrino oscillation, which has been observed almost fifteen years back by many experimental collaborations, requires neutrinos to have masses. So, the standard model, where neutrinos are massless, does not provide a consistent description of neutrinos.

Today we know that there are three active neutrino flavors:  $\nu_e$ ,  $\nu_\mu$  and  $\nu_\tau$  and that they are connected to three neutrino mass eigenstates:  $\nu_1$ ,  $\nu_2$  and  $\nu_3$  via a unitary mixing matrix. The parameters of this matrix are three mixing angles  $\theta_{12}$ ,  $\theta_{13}$  and  $\theta_{23}$  and a CP violating Dirac phase  $\delta_{CP}$ . The masses of the three mass eigenstates are traditionally denoted by  $m_1$ ,  $m_2$  and  $m_3$ . With the neutrino oscillation experiments carried out so far, the mixing angles and the mass squared differences (i.e.  $\Delta m_{ij}^2 = m_i^2 - m_j^2$ ) of the mass eigenstates have been estimated up to some accuracy. But many other parameters

of the phenomenology of neutrino physics are still unknown. For example, the sign of  $|\Delta m_{32}^2| = |m_3^2 - m_2^2|$ , the value of  $\delta_{CP}$  and the correct octant of  $\theta_{23}$  etc. are other unknown parameters which must be determined. It is also not known if neutrinos are the antiparticles of their own. We must understand these properties to have a better handle on the physics beyond standard model.

Since, neutrinos respond only to weak interactions, their detection is rather difficult. Typically, gigantic detectors are used (for example, Super Kamiokande) to detect only a handful of neutrinos events per day. Also, advanced detection technologies are employed. India has taken part in this worldwide quest by proposing the INO project, where efforts will be made (a) to resolve the neutrino mass hierarchy problem and (b) to check if the neutrinos are their own antiparticles. For the former, a giant magnetized iron tracking calorimeter (ICAL) detector will be built underground; for the latter, dedicated groups of experimental physicists will try to observe neutrino-less double beta decay which is a test for Majorana nature of neutrinos (i.e. if they are their own antiparticles).

ICAL detector will observe atmospheric neutrinos coming from a wide range of momenta  $P$  and direction (given by  $\cos \theta$ , where  $\theta$  is the zenith angle at the location of the detector). It will have the capability of observing neutrinos coming through the core of the earth. The probability of oscillation depends on the distance traveled by the neutrino, its energy, presence of matter and also on true mass hierarchy chosen by the nature. Hence, the profile of the events in the  $P - \cos \theta$  plane will be different, depending upon the hierarchy chosen by the nature. Therefore, it is important to be able to accurately estimate the momentum and direction of the events from the electronic signals observed in the detector. In this thesis, the corresponding methods of reconstructions have been developed.

---

 NEUTRINO PHYSICS
 

---

## 3.1 INTRODUCTION

Neutrinos are one of the fundamental particles in nature having peculiar properties. Their existence was first postulated by Pauli [29] in attempting to explain the beta decay of a neutron  $n$  to a proton  $p^+$  and a  $\beta$  particle ( $e^-$ ):



which seemed apparently to be a two body decay. Not only neutrons, nuclei of other heavier atoms also undergo  $\beta$  decays. Since, the recoil energy of the parent nucleus is small ( $\sim$  keV) compared to the total  $Q$  value of the reaction ( $\sim$  MeV), the kinetic energy acquired by the electron is approximately equal to the  $Q$  value [30]. In this specific example of  $\beta$  decay of a neutron, the kinetic energy of the electron becomes  $\approx 0.7823$ MeV. That is, *all* neutrons undergoing the decay produce electrons with the same kinetic energy (as neutron and proton masses are constants). Hence, the experimenter would expect to observe a peak in the distribution of the electron energy at  $\approx 0.7823$ MeV. If  $\beta$  decays of other nuclei are observed, the expected peak will be approximately equal to the  $Q$  value of the corresponding reaction. This value is referred to as end point energy of the electrons. However, a continuous energy spectrum was observed, when the real experiment was carried out with different nuclei. This is shown in the following figure 3.1. It appeared initially that the principle of conservation of energy was at stake

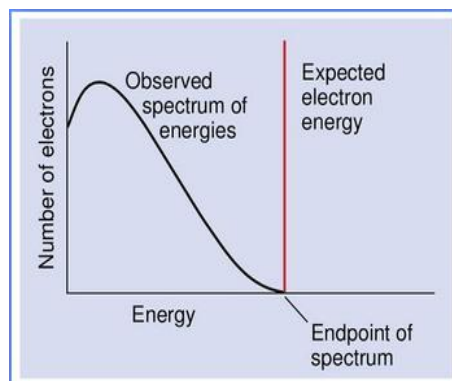


Figure 3.1.:  $\beta$  decay electron energy spectrum

in case of beta decay. Niels Bohr even suggested that perhaps energy conservation did

not hold inside the atomic nucleus. Pauli, however, in an attempt to save the principle of conservation of energy, postulated that perhaps there is a third undetected particle was coming out of the interaction. He called this uncharged (and perhaps massless) particle as a neutrino. This explanation was not very satisfactory to most of the scientists, but it motivated Fermi to write a consistent theory of nuclear beta decay, which can explain the continuous spectrum of energy of the electrons emitted during the beta decay. However, unless the particle was detected, all these efforts would have been meaningless. Finally, Reines and Cowan detected neutrino just outside a nuclear reactor in 1956, and the validity of the proposal of Pauli was established. Neutrinos were found to interact only through weak interactions with very small cross sections [31]. In last sixty years, fascinating evolution of neutrino physics has been observed. It started with Madam Wu's [32] experiment that showed that the parity symmetry is maximally violated in weak interactions. The impact of the result on theoretical development of standard model was immense, because theoreticians had to rewrite the standard model Lagrangian such that the parity violation fits naturally in the theory. Around the same time, Goldhaber [33] showed that neutrinos are left handed particles. Between 1960-2000 two more *types* of neutrinos were discovered,  $\nu_\mu$  and  $\nu_\tau$  in BNL [34] and in Fermilab [35]. The discovery of tau neutrino completed standard model framework consisting of twelve fundamental particles which cannot further be divided. This set comprises six quarks and six leptons, corresponding anti-particles and bosons, as shown in the following figure 3.2.

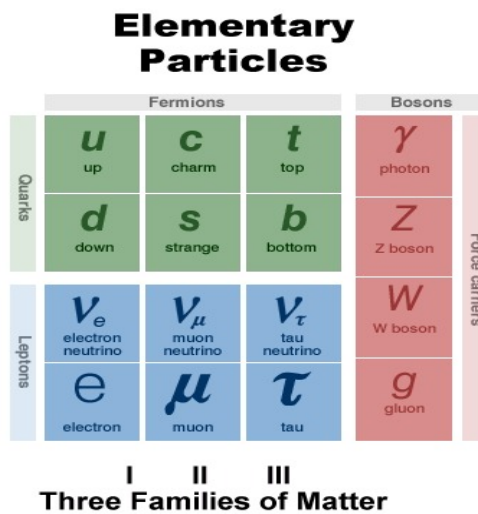


Figure 3.2.: Fundamental building blocks of nature

Apart from these, some scientists were carrying out observations of the neutrinos arriving the earth from the sun. They were trying to match the observed neutrino flux with expected flux, calculated from the standard solar model. From Chlorine experiment done at Homestake mines, Ray Davis and John Bahcall [36] reported that about two third of the neutrinos that they expected to reach the detector on earth from the sun, were missing. This observation led to serious doubts regarding the correctness of the experimental setup and the standard solar model. However, other experiments too reported similar observations as well (like SAGE and GALLEX) in the 1990's. On the other hand, standard solar model was also a reasonably good model otherwise and the

problem did not seem to be coming from that. The anomaly in the atmospheric neutrinos was established by 1985 by Super Kamiokande group. In the next section, we shall briefly review about these experiments and their major findings.

### 3.2 NEUTRINO DEFICIT EXPERIMENTS BEFORE 2000

Before 2000, most of the neutrino experiments were build to confirm or refute the claim of solar neutrino anomaly from Ray Davis's experiment. We briefly review these experiments in the following. Then, the atmospheric neutrino anomaly reported by the Super Kamiokande collaboration will be discussed.

#### 3.2.1 Chlorine experiment by Ray Davis

The Chlorine experiment was designed by Davis and Bahcall to detect the electron neutrinos coming from the sun. The sun produces copious amount of light and neutrinos when it shines, through the fusion of protons into Helium in its interior. There are many other mechanisms and the energy of the neutrinos produced in these interactions are shown in figure 3.3(a). Davis and his colleagues detected solar neutrinos by analyzing

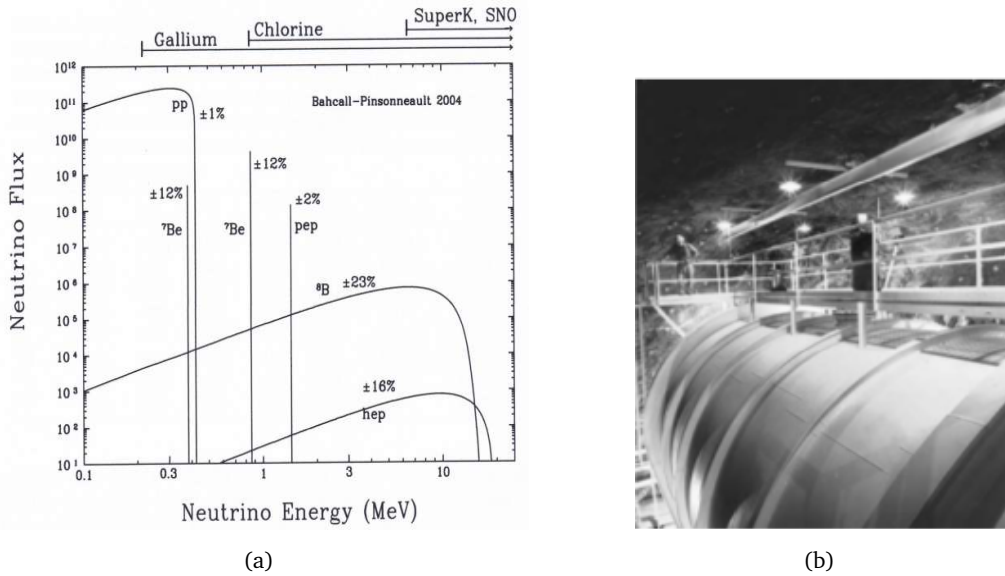
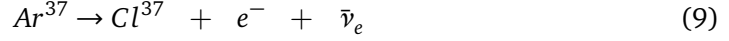


Figure 3.3.: (a) Neutrino spectrum of the sun for different solar reaction channels (b) Ray Davis's experimental setup at Homestake mine. Figure taken from [1].

Ar atoms produced in the interaction:



which had threshold of  $\sim 814$  keV. Therefore, this experiment was sensitive to pep, Be<sup>8</sup>, B<sup>8</sup> etc. channels of neutrino production, as seen from figure 3.3(a). These Ar atoms were radioactive and decayed to Cl with a half life of 35 days:



Davis was able to extract these Ar atoms and hence calculated the no. of observed neutrino interactions. It was seen [37] that measured flux of  $\nu_e$  was about one third of what was expected from the standard solar model.

### 3.2.2 SAGE and GALLEX

In the 1990's, SAGE experiment in Russia and GALLEX experiment in Italy independently verified the solar neutrino deficit problem. These experiment was also a radio-chemical experiment like the Chlorine experiment carried out by Ray Davis.

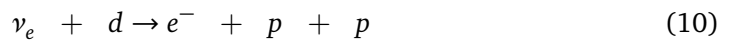
SAGE measured solar neutrinos from the inverse beta decay reaction  ${}^{71}\text{Ga}(\nu_e, e^{-}){}^{71}\text{Ge}$ . About 50 tons of liquid gallium was used as target in an underground laboratory at Baksan neutrino observatory, from where  $\nu_e$  induced  ${}^{71}\text{Ge}$  were extracted every month. From the radioactivity of  ${}^{71}\text{Ge}$ , it was possible to estimate the amount of  ${}^{71}\text{Ge}$  produced and hence the no. of neutrino interactions was calculated. GALLEX experiment also utilized the same reaction for this purpose. Since, the threshold of this reaction is small ( $\sim 233$ ) keV, it was possible to observe even low energy neutrinos (e.g. pp chain) coming from the sun. Both these experiments found deficit in the observed no. of neutrinos with respect to the expectation from the standard solar model [38], [39].

### 3.2.3 Super Kamiokande

Super Kamiokande detector is situated underground at Kamioka mine in Japan with a depth of 2700 mwe. It is a 50 kt water Cherenkov detector where the light produced in the  $\nu_e - e$  scatterings are detected with photo-multiplier tubes. It used a higher threshold to ensure that the electrons produced had small angle with respect to the parent neutrino. Therefore, it could observe the solar neutrinos coming only from  ${}^8\text{B}$  channel. This experiment found the observed flux to be about 46% of what was expected from the standard solar model [40].

### 3.2.4 SNO

The Sudbury neutrino observatory at Canada used heavy water for the detection of neutrinos. The use of  $\text{D}_2\text{O}$  instead of  $\text{H}_2\text{O}$  allows several nuclear reactions. The reaction that is sensitive to  $\nu_e$  only is:



This reaction has a threshold of 1.44 MeV. Apart from this, all flavors of neutrinos take part in the following elastic scattering process:



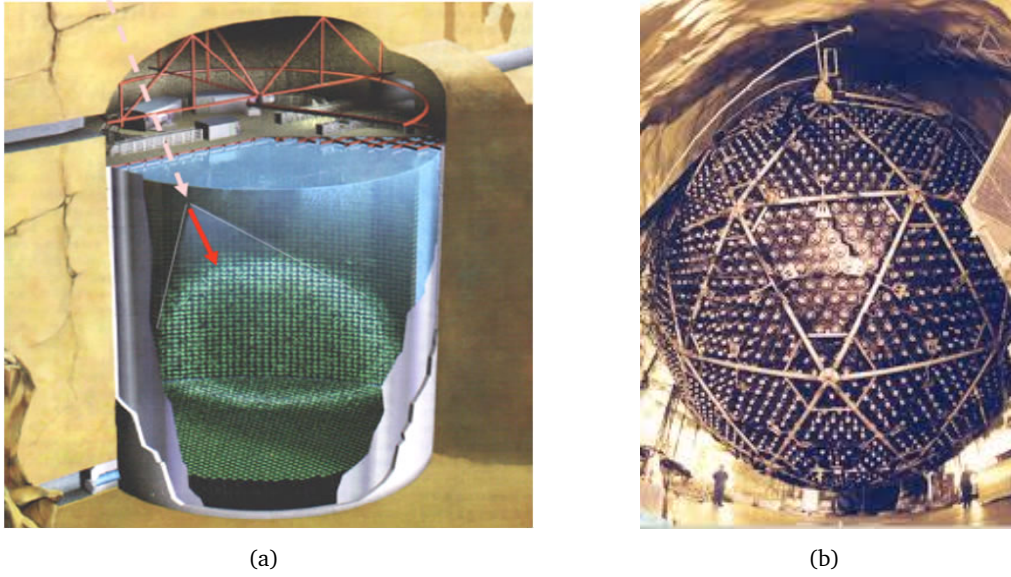
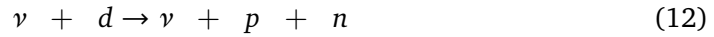


Figure 3.4.: (a) Giant cylindrical tank at Super Kamiokande and a prospective event  
 (b) Construction of heavy water Cherenkov detector at Sudbury neutrino observatory

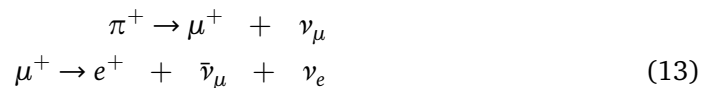
However, the cross section for this interaction is also dominated by  $\nu_e$ . Moreover, the experiment can also determine the total neutrino flux, independent of any oscillation, due to the flavor independent neutral current weak interactions:



which has a threshold of 2.225 MeV. It was found that the no. of events detected due to the flavor-blind reaction is in very good agreement with the standard solar model predictions. Thus, SNO data had ample reasons to believe that the neutrinos coming from the sun somehow change their flavors midway. SNO could observe all possible flavors, but the earlier experiments did not have this facility for which they reported the neutrinos arriving with different flavors as missing [41].

### 3.2.5 Atmospheric neutrinos: Super Kamiokande

Super Kamiokande collaboration also observed atmospheric neutrinos whose energy are of the order of GeV. These neutrinos are produced in the upper atmosphere from the decay of pions generated from the collisions of air nuclei with the cosmic rays. The pions decay as:



Thus, the expected no. of  $\nu_\mu$ s to be observed at the earth surface is about two times the no. of  $\nu_e$ s. In fact, the ratio should increase with energy due to time dilation of muon lifetime, as seen by an observer on the earth. Since, every charged current (CC)  $\nu$  event produces a lepton of the same flavor, we expect the ratio  $\frac{(\mu/e)_{obs}}{(\mu/e)_{expected}}$  to be equal to unity. However, it was found to be less than unity [42]. On the other hand, it was found that

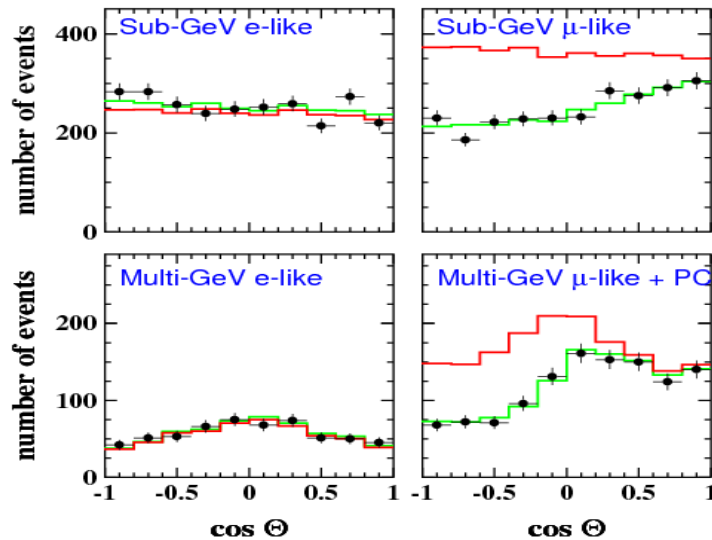


Figure 3.5.: Super Kamiokande:  $\nu_\mu$  deficit

the electron neutrinos coming from top and from bottom match expectation whereas the muon neutrinos coming from bottom (i.e. events that reach the detector after crossing through the earth) do not match predictions, as shown in figure 3.5.

### 3.3 EXPLANATION OF THE FINDINGS

In standard model of particle physics, neutrinos are assumed to be massless particles. But in 1968, Pontecorvo [43] showed that if neutrinos had mass, then they could change from one type to another. Thus, the missing solar neutrinos could be electron neutrinos that changed into other types along the way to Earth and therefore were not seen by the detectors in the Homestake Mine. Immediately after his proposal, Maki, Nakagawa and Sakata generalized the mixing and oscillation phenomenology between three neutrino flavors [44]. Whereas there were many speculations on what might have happened to the missing neutrinos, only the model of neutrino oscillation fitted the data of all

these experiments accurately. After almost forty years, the solution of the solar neutrino problem came from the KamLAND reactor neutrino experiment and SNO solar neutrino experiment in 2002. Therefore, we shall discuss next about the phenomenology of the neutrino oscillation.

### 3.3.1 Two neutrino mixing

In case the neutrinos have non-zero mass, it is possible to have mixing among the neutrino flavors. This means that the flavor states  $\nu_e$ ,  $\nu_\mu$  and  $\nu_\tau$  are not eigenstates of mass, but instead are linear combinations of three states:  $\nu_1$ ,  $\nu_2$  and  $\nu_3$  that are eigenstates of mass. Let us assume that these states have masses  $m_1$ ,  $m_2$  and  $m_3$ . Neutrinos are produced or detected as flavor states in weak interactions, but their propagation is controlled by the mass eigenstates. Although there are three active flavors of neutrinos, it is helpful to study the phenomenology of neutrino oscillation at first in case of two neutrino flavors. In this case, we assume that the flavor states are connected to mass states via a unitary mixing matrix, parametrized by a mixing parameter  $\theta$ :

$$\begin{pmatrix} \nu_\mu \\ \nu_e \end{pmatrix} = \begin{pmatrix} \cos \theta & \sin \theta \\ -\sin \theta & \cos \theta \end{pmatrix} \begin{pmatrix} \nu_1 \\ \nu_2 \end{pmatrix} \quad (14)$$

The mixing angle must be determined from an experiment. If  $\theta \neq 0$  each of the flavor states will be dependent on *all* the mass states. When, for example, a muon neutrino is produced with momentum  $p$  at time  $t = 0$ , the  $\nu_1$  and  $\nu_2$  components will have slightly different energies  $E_1$  and  $E_2$  due to their slightly different mass values  $m_1$  and  $m_2$ . Thus, their associated wave functions will have slightly different frequencies, giving rise to a phenomenon like *beats*, heard when two sound waves of slightly different frequencies superimpose [45]. As a result, the beam of  $\nu_\mu$  develop a  $\nu_e$  component whose intensity (probability of detection as  $\nu_e$ ) oscillates as the beam travels through space. Clearly, the component of original  $\nu_\mu$  is reduced correspondingly, to conserve the probability, leading to disappearance of muon neutrinos. This is shown below:

The evolution of a given flavor state with time is given as:

$$\begin{aligned} i \frac{d}{dt} |\nu(t)\rangle &= \hat{H} |\nu(t)\rangle \\ \Rightarrow |\nu(t)\rangle &= e^{-i\hat{H}t} |\nu(t=0)\rangle \end{aligned} \quad (15)$$

Now, as long as no interaction happens, the neutrino may be thought of as moving as a free particle in vacuum, where it is not affected by electromagnetic, strong or weak potential. Consequently, the Hamiltonian  $\hat{H}$  is given by:

$$\begin{aligned} H &= \sqrt{p^2 + m^2} \\ &\approx p + \frac{m^2}{2p} \end{aligned} \quad (16)$$

The evolution of mass states  $|\nu_1(t)\rangle$ ,  $|\nu_2(t)\rangle$  etc. are determined by this Hamiltonian. From Eq. (14), the time evolution of  $|\nu_\mu(t)\rangle$  is given by:

$$|\nu_\mu(t)\rangle = \cos \theta e^{-ipt} e^{-i\frac{m_1^2 t}{2p}} |\nu_1(t=0)\rangle + \sin \theta e^{-ipt} e^{-i\frac{m_2^2 t}{2p}} |\nu_2(t=0)\rangle \quad (17)$$

Hence, the probability that the neutrino flavor stays as  $\nu_\mu$ , after the neutrino has propagated a distance  $L$  in time  $t$  is given as the squared modulus of the corresponding amplitude:

$$\begin{aligned} P_{\mu\mu} &= |\langle \nu_\mu(t=0) | \nu_\mu(t) \rangle|^2 \\ &= 1 - \sin^2 2\theta \sin^2 \left( \frac{\Delta m^2 t}{4E} \right) \end{aligned} \quad (18)$$

where  $\Delta m^2 = m_2^2 - m_1^2$  and  $p \approx E$  for neutrinos with extremely tiny mass. It is seen from Eq.(18), that the amplitude of the oscillation is determined by the mixing angle  $\theta$  and the wavelength of the oscillation depends on  $\Delta m^2$ , energy  $E$ . In the natural units,  $c = 1$ . If  $\Delta m^2$ , length and energy are expressed in  $\text{eV}^2$ , km and GeV respectively, then we have:

$$P_{\mu\mu} = 1 - \sin^2 2\theta \sin^2 \left( \frac{1.27 \Delta m^2 L (\text{km})}{E (\text{GeV})} \right) \quad (19)$$

The  $\frac{L}{E}$  dependence of the phase in Eq.(19) is a characteristic signature of neutrino oscillation. The wavelength of the oscillation is dependent on  $\frac{E}{\Delta m^2}$  factor. In the following figure 3.6, the survival probability of a neutrino of initial flavor  $\alpha$  (transition from  $\nu_\alpha \rightarrow \nu_\alpha$ ) is shown, for  $\sin^2 2\theta = 0.83$  (corresponding to solar mixing angle). Clearly, no

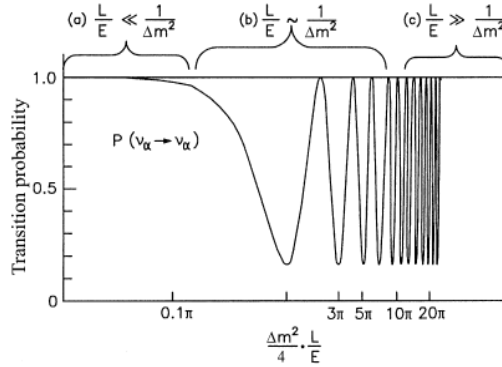


Figure 3.6.:  $L/E$  dependence of neutrino survival probability. Figure adopted from [1]

significant oscillation is observed when  $\frac{L}{E} \ll \frac{1}{\Delta m^2}$ , as the argument of the sine function is close to zero. Also, when  $\frac{L}{E} \gg \frac{1}{\Delta m^2}$ , the oscillation gets averaged out. But if  $\frac{L}{E} \sim \frac{1}{\Delta m^2}$ , some significant oscillation is expected.

### 3.3.2 Three neutrino mixing

Maki, Nakagawa and Sakata put forward the concept of mixing among the three neutrino flavors through a unitary mixing matrix in early 1960's. In this formalism, three neutrino flavors eigenstates are connected to three neutrino mass states via the  $U_{PMNS}^{3 \times 3}$  matrix, somewhat similar to  $CKM$  matrix for quarks. This matrix is parametrized by three mixing angles  $\theta_{12}$ ,  $\theta_{13}$ ,  $\theta_{23}$  and the CP-violating Dirac phase  $\delta_{CP}$  [46]. In matrix form, the connection is given by:

$$|\nu_\alpha\rangle = \sum_{i=1}^{i=3} U_{\alpha i} |\nu_i\rangle \quad (20)$$

where  $\alpha \in [e, \mu, \tau]$  denotes the flavor states and  $i \in [1, 2, 3]$  denotes the mass states. A schematic diagram of this three flavor mixing is shown in figure 3.7: The  $U_{PMNS}$  matrix

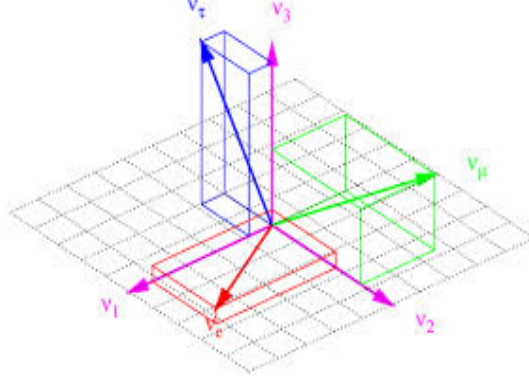


Figure 3.7.: Three neutrino flavor mixing

can be expressed as [1]:

$$U_{PMNS}^{3 \times 3} = \begin{pmatrix} 1 & 0 & 0 \\ 0 & c_{23} & s_{23} \\ 0 & -s_{23} & c_{23} \end{pmatrix} \begin{pmatrix} c_{13} & 1 & s_{13}e^{i\delta} \\ 0 & 1 & 0 \\ -s_{13}e^{i\delta} & 1 & c_{13} \end{pmatrix} \begin{pmatrix} c_{12} & s_{12} & 0 \\ -s_{12} & c_{12} & 0 \\ 0 & 0 & 1 \end{pmatrix} \quad (21)$$

where  $s_{ij}$  and  $c_{ij}$  refer to the sine and cosine of the mixing angle  $\theta_{ij}$ . In the three flavor case, the probability of vacuum oscillation is given by [7]:

$$P(\nu_\alpha \rightarrow \nu_\beta) = \delta_{\alpha\beta} - 4 \sum_{i>j=1}^3 \text{Re}(K_{\alpha\beta,ij}) \sin^2 \frac{\Delta m_{ij}^2 L}{4E} + 2 \sum_{i>j=1}^3 \text{Im}(K_{\alpha\beta,ij}) \sin \frac{\Delta m_{ij}^2 L}{2E} \quad (22)$$

where  $\delta_{\alpha\beta} = 1$  when  $\alpha = \beta$  and  $\delta_{\alpha\beta} = 0$  when  $\alpha \neq \beta$ ;  $K_{\alpha\beta,ij} = U_{\alpha i} U_{\beta i}^* U_{\alpha j}^* U_{\beta j}$  and  $\Delta m_{ij}^2 = m_i^2 - m_j^2$ . The two flavor oscillation formula, discussed before, is the limiting case where only one of the two  $\Delta m^2$  is under consideration. If the oscillation between anti-neutrino states are considered, the factor with  $\text{Im}(K_{\alpha\beta,ij})$  will have a negative sign instead of the positive sign in Eq.(22). Thus, if the  $U_{PMNS}$  matrix is complex, then it is possible to have  $CP$  violation [47] in leptonic sector of particle physics and this can be observed by measuring the  $CP$  asymmetry term in the oscillation experiments:

$$\begin{aligned} \Lambda_{\alpha\beta}^{CP} &= P_{\nu_\alpha \rightarrow \nu_\beta} - P_{\bar{\nu}_\alpha \rightarrow \bar{\nu}_\beta} \\ &= 4 \sum_{i>j=1}^3 \text{Im}(K_{\alpha\beta,ij}) \sin \frac{\Delta m_{ij}^2 L}{2E} \\ &= 4 [\pm c_{12} s_{12} c_{23} s_{23} c_{13}^2 s_{13} \sin \delta] \sin \frac{\Delta m_{ij}^2 L}{2E} \end{aligned} \quad (23)$$

In Eq.(23),  $\pm$  sign denotes cyclic or anti-cyclic permutation of  $(\alpha, \beta) = (e, \mu), (\mu, \tau), (\tau, e)$ . To find if the neutrino oscillation was indeed a good explanation of the observed deficit

in the no. of  $\nu_e$  (solar) and that of  $\nu_\mu$  (atmospheric), the data was to be fitted with the predictions of this model. If the model fits well, the validity of the neutrino oscillation would be established and the allowed range of  $\Delta m_{ij}^2$  and mixing angles would give the values of the oscillation parameters. The oscillation hypothesis was indeed found to give good explanation for the solar and atmospheric neutrino anomalies reported by various experiments and the oscillation parameters were estimated from the KamLAND and Super Kamiokande experiments.

### 3.4 KAMLAND AND SUPER KAMIOKANDE

#### 3.4.1 KamLAND

Whereas SNO experiment had already reported with evidence [41] analyzing neutral current channels, the oscillation parameters responsible for solar neutrino problem were to be constrained. For this purpose, KamLAND detector was built to detect the reactor neutrinos delivered from the nuclear reactors in Japan and South Korea. The disappearance of the solar neutrinos is driven by the oscillations due to  $\nu_1$  and  $\nu_2$  states which mix by the matrix with  $\theta_{12}$  term. The existing data were consistent with  $\Delta m_{21}^2 \sim 10^{-5}$  with large mixing angle  $\theta_{12}$ . Using the two neutrino oscillation probability expression and the fact that the solar and the reactor neutrinos are of similar energies, it was found that to observe some oscillation, the baseline  $L \sim 100$  km (corresponding to case (b)  $\frac{L}{E} \sim \frac{1}{\Delta m^2}$  in figure 3.6).

The detector was an 1 kton liquid scintillator contained within a sphere. The reactors produce  $\bar{\nu}_e$  with energy  $E \sim 3$  MeV. The flux measured in the detector was about one third of the total flux coming from the reactors, consistent to solar neutrino data. The oscillation analysis gave the following values of the parameters  $\Delta m_{21}^2 = m_2^2 - m_1^2 \approx 7.6 \times 10^{-5} eV^2$  and  $\sin^2 \theta_{12} \approx 0.32$ . This was referred to as the Large Mixing Angle (LMA) solution in the literature [48]. This gave the solution of the solar neutrino anomaly that baffled physicists for about forty years.

#### 3.4.2 Super Kamiokande

Around the same time (1998), Super Kamiokande group published their result with evidences of neutrino oscillation between  $\nu_\mu$  and  $\nu_\tau$  flavors [8]. As reported earlier, the  $\nu_\mu$ s coming from the bottom (i.e. crossing through the earth) were found missing. This was because the neutrino oscillation probability is modified significantly when the neutrino is traveling through matter. The presence of the earth matter made the  $\nu_\mu$ s oscillate into  $\nu_\tau$ s. The data was found to be consistent with the parameters  $|\Delta m_{32}^2| \approx 2.4 \times 10^{-3} eV^2$  and  $\sin^2 \theta_{23} \approx 0.56$ . Whereas, the oscillation model led to a very good fit of the data, it was not clear if  $m_3^2 > m_2^2$  or  $m_2^2 > m_3^2$ . This degeneracy gave rise to the neutrino mass hierarchy problem, which remains unsolved till date.

### 3.5 MATTER EFFECTS IN NEUTRINO OSCILLATION

Previously, we have discussed the phenomenology of neutrino oscillation in vacuum. However, in many occasions, it becomes necessary to study neutrino oscillation in the

presence of matter. For example, when neutrino travels inside the sun or inside the earth. During the motion, they suffer from coherent forward scattering (without change in momenta) from the leptons in the medium. Since, common matter has only electrons, it is  $\nu_e$  which can interact with them through both charged current (CC) and neutral current (NC) interactions. However, since there is no  $\mu^-$  or  $\tau^-$  in normal matter, the  $\nu_\mu$  and  $\nu_\tau$  can only respond to the NC scatterings. This leads to the following effects on the evolution of neutrino states. It can be shown that in vacuum, the evolution of the flavor states can be expressed as:

$$\begin{aligned} i \frac{d}{dt} \begin{pmatrix} \nu_e \\ \nu_\mu \end{pmatrix} &= \left[ \begin{pmatrix} c\theta & s\theta \\ -s\theta & c\theta \end{pmatrix} \begin{pmatrix} -\Delta & 0 \\ 0 & +\Delta \end{pmatrix} \begin{pmatrix} c\theta & s\theta \\ -s\theta & c\theta \end{pmatrix}^\dagger \right] \begin{pmatrix} \nu_e \\ \nu_\mu \end{pmatrix} \\ &= \left[ \left( \frac{\Delta m^2}{4E} \right) \begin{pmatrix} -\cos 2\theta & \sin 2\theta \\ \sin 2\theta & \cos 2\theta \end{pmatrix} \right] \begin{pmatrix} \nu_e \\ \nu_\mu \end{pmatrix} \end{aligned} \quad (24)$$

where  $\Delta = \frac{\Delta m^2}{4E} \equiv \frac{m_2^2 - m_1^2}{4E}$  and the whole matrix inside the square bracket represents the Hamiltonian in vacuum. In presence of matter, the Hamiltonian is modified. If the flavor state is given by  $(\nu_e \quad \nu_\mu \quad \nu_\tau)^T$ , the corresponding terms to be added to this Hamiltonian are:

$$V = \begin{pmatrix} V_{CC} + V_{NC} & 0 & 0 \\ 0 & V_{NC} & 0 \\ 0 & 0 & V_{NC} \end{pmatrix} \quad (25)$$

where  $V_{CC} = \pm \sqrt{2} G_F n_e$  (+ve for  $\nu$ , -ve for  $\bar{\nu}$ ) and  $V_{NC} = -\sqrt{2} G_F n_n$  [49]; here  $G_F$  denotes the Fermi coupling constant and  $n_e$ ,  $n_n$  denote the density of electrons and neutrons in the matter. Therefore, in two flavor case, effective Hamiltonian in matter becomes:

$$\begin{aligned} \hat{H}_m &= \begin{pmatrix} c\theta & s\theta \\ -s\theta & c\theta \end{pmatrix} \begin{pmatrix} -\Delta & 0 \\ 0 & +\Delta \end{pmatrix} \begin{pmatrix} c\theta & s\theta \\ -s\theta & c\theta \end{pmatrix}^\dagger + \begin{pmatrix} V_{CC} & 0 \\ 0 & 0 \end{pmatrix} \\ &= \begin{pmatrix} -\Delta \cos 2\theta + V_{CC} & \Delta \sin 2\theta \\ \Delta \sin 2\theta & \Delta \cos 2\theta \end{pmatrix} \\ &:= \begin{pmatrix} -\Delta \cos 2\theta + V_{CC}/2 & \Delta \sin 2\theta \\ \Delta \sin 2\theta & \Delta \cos 2\theta - V_{CC}/2 \end{pmatrix} \\ &= \Delta \begin{pmatrix} -\cos 2\theta + A & \sin 2\theta \\ \sin 2\theta & \cos 2\theta - A \end{pmatrix} \end{aligned} \quad (26)$$

where we have subtracted a constant multiple of identity matrix

$$\begin{pmatrix} V_{CC}/2 & 0 \\ 0 & V_{CC}/2 \end{pmatrix}$$

between the second and third equality which does not have any effect on the dynamics. The term  $A$  is given by:

$$A = \pm \frac{2\sqrt{2} G_F n_e E}{\Delta m^2} \quad (27)$$

The solution of the corresponding Schrödinger equation is simple if the matter density is constant. In that case, we can diagonalize  $H_m$  to obtain the mixing matrix and mass eigenstates in matter via a rotation matrix. If we denote the effective mixing angle in

matter as  $\theta_m$  and the effective difference of squared masses as  $\Delta m_m^2$ , we can write the Hamiltonian in matter using the same form as the vacuum Hamiltonian (Eq.(24)):

$$\hat{H}_m = \left( \frac{\Delta m_m^2}{4E} \right) \begin{pmatrix} -\cos 2\theta_m & \sin 2\theta_m \\ \sin 2\theta_m & \cos 2\theta_m \end{pmatrix} \quad (28)$$

and this leads to the usual functional dependence of the oscillation probability:

$$P(\nu_e \rightarrow \nu_\mu) = \sin^2 2\theta_m \sin^2 \left( \frac{\Delta m_m^2 L}{4E} \right) \quad (29)$$

Equating their corresponding terms in Eq.(26) and Eq.(28), we have:

$$\Delta m_m^2 = C \Delta m^2 \quad (30)$$

$$\sin 2\theta_m = \sin 2\theta / C \quad (31)$$

$$C = \sqrt{(\cos 2\theta - A)^2 + \sin^2 2\theta} \quad (32)$$

Under the resonance condition  $A = \cos 2\theta$ , the oscillation may be significantly enhanced and may lead to complete inversion of flavor. This is known as the MSW effect [7], after Mikhaev, Smirnov and Wolfenstein. From the fact that  $\Delta m_{21}^2 \sim 10^{-5} \text{ eV}^2$  and  $\theta_{12} \sim 30^\circ$ , one can show that the neutrino energy must be  $\sim 1 \text{ MeV}$  at the solar core to have MSW resonance.

Oscillation probabilities for neutrino and antineutrinos can be different due to matter effects, because of the  $\pm$  sign in front of  $V_{CC}$ , even if there is no CP violation. The resonance condition occurs if  $A > 0$ , which in turn, depends on the sign of  $\Delta m^2$  (from Eq.(27)). This dependence on the sign of  $\Delta m^2$  can be used to determine the neutrino mass hierarchy. For example, long baseline accelerator neutrino experiments, which look for  $\nu_\mu \rightarrow \nu_e$  oscillations in the region of  $\Delta m^2 \sim \Delta m_{32}^2$ , are sensitive to the mass hierarchy through matter effects in the Earth if the baseline is sufficiently long ( $\sim 1000 \text{ km}$ ) and the energy is sufficiently high, so that matter effects are significant. In more concrete words, the factor  $L(\text{km})/E(\text{GeV})$  should be of the order of  $10^3$  such that  $\frac{L}{E} \sim \frac{1}{\Delta m_{32}^2}$ , because for atmospheric neutrinos,  $\Delta m_{32}^2 (\text{eV}^2) \sim 10^{-3}$  (see figure 3.6).

### 3.6 NEUTRINO OSCILLATION EXPERIMENTS AFTER 2000

It was clear by 2000-2002 that neutrino oscillation was the reason behind the anomalies found in the solar neutrino data and atmospheric neutrino data. After that most of the neutrino detectors were built to (a) measure the neutrino interaction cross sections, (b) determine the oscillation parameters which were unknown (like  $\theta_{13}$ ), (c) resolve the neutrino mass hierarchy etc. For about one and a half decade, some important discoveries were made in neutrino physics, apart from improving the oscillation parameters (precision measurement). In the following, we discuss about some of these experiments.

### 3.6.1 Experiments

#### 3.6.1.1 MINOS

MINOS is a long baseline accelerator neutrino experiment [50] operating at  $E \sim 0.5$  GeV. The near detector is at Fermilab at about a km away from the source and the far detector is located at Soudan underground laboratory about 735 km away from the source. The experiment mainly studies charged current quasi elastic interactions through a calorimeter composed of steel plates and solid scintillators. It confirmed the claim of neutrino oscillation by the Super Kamiokande group.

#### 3.6.1.2 LSND

LSND was a liquid scintillator neutrino detector located at LANL [51] that was aimed to look for the signature of neutrino oscillation in accelerator neutrinos. Their observations conflict that there exist only three flavors of neutrinos. The analysis of the data of this experiment gave rise to the concept of sterile neutrinos which are supposedly heavier neutrino states, but do not respond to the interactions mediated by the standard model.

#### 3.6.1.3 MiniBoone

To test the sterile neutrino hypothesis, the MiniBoone experiment [52] was designed. It uses  $\sim 1$  kton of mineral oil as target material. The neutrino interactions from carbon produces muons that gives Cherenkov light, to be detected with  $\sim 1300$  photo multiplier tubes. So far, it has not been able to reproduce the LSND anomaly.

#### 3.6.1.4 SciBoone

SciBoone was an accelerator neutrino experiment located at FNAL [53]. It was designed to estimate the neutrino and anti-neutrino interaction cross sections accurately on carbon and iron nuclei. They also measured the intrinsic properties of the Booster Neutrino Beam at Fermilab, which sends the neutrinos to MiniBooNE, improving the accuracy of the MiniBooNE results.

#### 3.6.1.5 MINER $\nu A$

MINER  $\nu A$  is a neutrino scattering experiment which uses the NuMI beamline at Fermilab [54]. It tried to measure low energy neutrino interactions both in support of neutrino oscillation experiments and also to study the strong dynamics of the nucleon and nucleus that affect these interactions. Solid scintillators were used for detection. The members of this collaboration used neutrinos to transmit a message (the word “neutrino”) through the presence (state 1) or the absence (state 0) of the neutrino pulse [55].

#### 3.6.1.6 NO $\nu A$

NO  $\nu A$  is a neutrino oscillation experiment designed to detect  $\nu_e$ s at an off axis detector, that presumably oscillate from  $\nu_\mu$  beam of FNAL [56]. By observing the no. of oscillated  $\nu_e$ s, NO  $\nu A$  attempts to measure (a) the mixing angle  $\theta_{13}$ , (b) neutrino mass hierarchy and (c) CP violating phase  $\delta$ .

### 3.6.1.7 *T2K*

T2K is a long baseline neutrino oscillation experiment where the off-axis muon neutrino beam is sent from Tokai (J PARC) to the detector system at Kamioka (295 km) [57]. The main goal of this experiment is to observe  $\nu_\mu \rightarrow \nu_e$  oscillation and the determination of the mixing angle  $\theta_{13}$ . The collaboration reported the observation of  $\nu_e$ s in July, 2013. Since, the oscillation is governed by  $\theta_{13}$ , it was clear that the mixing angle is not zero. This means that if the CP violating phase  $\delta$  itself does not turn out to be zero, then it should be possible to observe CP violation in leptonic sector (Eq.(23)).

### 3.6.1.8 *CHOOZ and Double CHOOZ*

CHOOZ was a long baseline reactor neutrino oscillation experiment in Chooz, France. Its major result was to set limits on the neutrino oscillation parameters responsible for changing electron neutrinos into other neutrinos. Specifically, it found that  $\sin^2 2\theta_{13} < 0.17$  [58]. The Double Chooz experiment continues to take data using the same lab space.

### 3.6.1.9 *Daya Bay*

Daya Bay is a reactor neutrino experiment in China [59]. The experiment studies neutrino oscillations and is designed to measure the mixing angle  $\theta_{13}$  using antineutrinos produced by the nearby reactors. In March 2012, the Daya Bay collaboration announced a  $5.2\sigma$  discovery of non-zero  $\theta_{13}$ . They reported that  $\sin^2 2\theta_{13} = 0.092 \pm 0.016(\text{stat}) \pm 0.005(\text{syst})$ .

### 3.6.1.10 *RENO*

RENO is a short baseline reactor neutrino experiment at south Korea [60]. The experiment was designed to either measure or set a limit on  $\theta_{13}$ . In April, 2012, the RENO collaboration reported a  $4.9\sigma$  observation of non-zero  $\theta_{13}$ .

### 3.6.1.11 *ICARUS*

The ICARUS experiment is located at Gran Sasso, Italy. It concerns the usage of Liquid Argon (LAr) detector for studies of neutrinos from CNGS beam [61]. The advantage of this LAr time projection chamber (TPC) is its excellent spatial and calorimetric resolution which makes possible a visualization of tracks of the charged particles.

### 3.6.1.12 *OPERA*

OPERA experiment attempted to detect  $\nu_\tau$ s oscillated from CNGS  $\nu_\mu$  beam. In May 2010, OPERA researchers observed the first tau neutrino candidate event [62] in a muon neutrino beam.

### 3.6.1.13 *BOREXINO*

BOREXINO was a liquid scintillator experiment located at Gran Sasso, Italy. It was designed to detect sub MeV solar neutrinos. Between 2007 and 2011, they reported the

observation of solar neutrinos, geoneutrinos coming from the interior of the earth and also the observation of  $^7\text{Be}$  and pep neutrinos.

#### 3.6.1.14 IceCube

IceCube is a neutrino telescope of one  $\text{km}^3$  dimension located in the deep underground at the south pole. It observes the very high energy neutrinos [63] with the Cherenkov radiation produced inside the ice. The light is detected by spherical optical sensors, equipped with photo multiplier tubes.

#### 3.6.2 Current status

The experiments put good constraints on the allowed parameter space of neutrino oscillation. With the global neutrino oscillation analysis from the data of all these experiment, one can obtain the best fit parameters. The present neutrino oscillation parameters, as reported in Neutrino 2014 conference [64], are shown in the following table 5. Here,  $\Delta m^2 = \left( m_3^2 - \left( \frac{m_1^2 + m_2^2}{2} \right) \right)$  with  $+\Delta m^2$  representing normal hierarchy (NH) and  $-\Delta m^2$  representing inverted hierarchy (IH).

Parameter	Best fit	1- $\sigma$
$\delta m_{21}^2/10^{-5} \text{ eV}^2$ (NH or IH)	7.54	7.32-7.80
$\sin^2 \theta_{12}/10^{-1}$ (NH or IH)	3.08	2.91-3.25
$\Delta m^2/10^{-3} \text{ eV}^2$ (NH)	2.43	2.37-2.49
$\Delta m^2/10^{-3} \text{ eV}^2$ (IH)	2.38	2.32-2.44
$\sin^2 \theta_{13}/10^{-2}$ (NH)	2.34	2.15-2.54
$\sin^2 \theta_{13}/10^{-2}$ (IH)	2.40	2.18-2.59
$\sin^2 \theta_{23}/10^{-1}$ (NH)	4.37	4.14-4.70
$\sin^2 \theta_{23}/10^{-1}$ (IH)	4.55	4.24-5.94
$\delta/\pi$ (NH)	1.39	1.12-1.77
$\delta/\pi$ (IH)	1.31	0.98-1.60

Table 5.: Neutrino oscillation parameters

#### 3.6.3 Open questions

However, the quest goes on. Because there are variety of questions still unanswered in this field. For example, the sign of  $|\Delta m_{32}|^2$  is not known yet and this leads to the neutrino mass hierarchy problem: the mass eigenstates might be arranged in any one of the two possible patterns, as shown in figure 3.8. The normal hierarchy (NH) corresponds to  $m_1 < m_2 < m_3$ , whereas the inverted hierarchy (IH) corresponds to  $m_3 < m_1 < m_2$ . Exploiting the fact that the matter effects experienced by the neutrinos and the anti-neutrinos are different, and that sign of  $A$  depends on the sign of  $\Delta m^2$  (Eq.(27)), it might be possible to resolve the mass hierarchy by designing very long baseline experiments [6]. Apart from the pattern of arrangement of the neutrino mass states, the absolute scale of

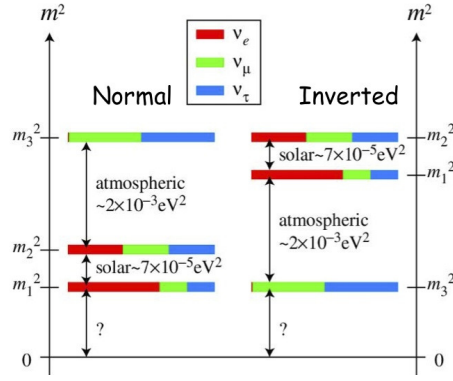


Figure 3.8.:  $\nu$  mass hierarchy problem

the masses is also not known. The mass generation mechanism of neutrino is another unknown issue. This is specially important, because it is a signature of physics beyond standard model. The violation of  $CP$  symmetry in leptonic sector is also to be tested. Therefore, this field requires more experiments to be built up with advanced equipments. Not only in high energy ( $> \text{GeV}$ ) end but also in low energy ( $\sim \text{MeV}$ ) experiments. For example, the observation of neutrinoless double beta decay, which is essentially a nuclear physics experiment at MeV range, would prove the Majorana nature of neutrinos; i.e. it would resolve whether or not the neutrinos are their own anti-particles. There are also attempts of direct mass measurement (or giving upper bound) of neutrinos through the experiments like KATRIN [65].

#### 3.6.4 India-based Neutrino Observatory

Indian scientists have adopted the India-based Neutrino Observatory project to contribute in the worldwide efforts on neutrino physics. This is a resurrection of experimental neutrino physics in the country after 1960's when the scientists detected atmospheric neutrino events in the Kolar gold field (KGF) mines. The proposed project has two major parts (a) the **Iron CALorimeter (ICAL)** detector to observe neutrino oscillation and (b) the **Neutrino-less Double Beta Decay (NDBD)** experiment.

The main project, ICAL detector, is a 50 kton magnetized iron tracking calorimeter and will observe the atmospheric neutrinos coming from all directions. This will be a long baseline detector to those neutrinos which are crossing through the core of the earth. For these neutrinos, the baseline  $L$  is of the order of the diameter of the earth. Therefore, ICAL will have access to the neutrinos of a wide range of baseline (10 – 12800) km.

ICAL will attempt to resolve the neutrino mass hierarchy problem, by observing the oscillation of the neutrinos. The main signal will come from the muon neutrinos, which will produce muons after interacting with the detector material. The track of the muon will bend in the magnetic field and by observing the curvature, it would be possible to know the charge and momenta of the muons. This will also give the information whether  $\nu_\mu$  or  $\bar{\nu}_\mu$  generated those  $\mu^-$ s or  $\mu^+$ s. To shield the background cosmic muons, the detector will be placed underground, within a cavern beneath the west Bodi Hills near Theni in south India. The experimental hall will have at least one kilometer solid rock coverage all around such that most of the cosmic muons are absorbed.

Apart from trying to resolve the neutrino mass hierarchy, the experiment will also carry out the precision measurement of the atmospheric neutrino oscillation parameters. Study of non-standard interactions and sterile neutrinos are also speculated. The R&D works for the detector is in progress. The present thesis is a part of these efforts only. The INO project, apart from ICAL, will also house other experiments like NDBD and DINO (Dark matter search in INO) etc.

---

 ICAL DETECTOR AT INDIA BASED NEUTRINO OBSERVATORY PROJECT
 

---

## 4.1 INTRODUCTION

The experiment aims to carry out the following programs through the ICAL detector at the INO project [5].

- validate the neutrino oscillation hypothesis with atmospheric neutrinos. This will require the observation of the deficit in the no. of muon neutrinos which come from bottom (i.e. through the earth matter) like the Super Kamiokande collaboration.
- perform precision measurements of atmospheric neutrino oscillation parameters.
- resolve the neutrino mass hierarchy problem by observing the matter effect on neutrinos and antineutrinos.
- verify the existence of the sterile neutrinos, probe nonstandard interactions etc.

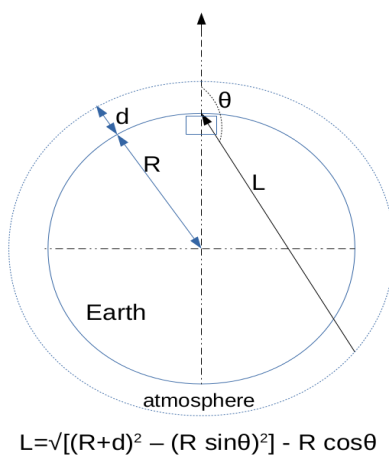


Figure 4.1.: ICAL detector and its window to atmospheric neutrinos

For these reasons, the detector must be built in such a manner that a significant no. of  $\nu$  events may be observed over a period of a decade or more. Hence, the target mass of the detector should be very large (say,  $\sim 50$  kton). The detector must also be able to distinguish neutrino events from antineutrino events and should have good resolutions for energy and direction estimation. This is to ensure the sensitivity of oscillation of  $\nu$  and  $\bar{\nu}$  by probing  $\frac{L}{E}$ . This is because,  $L$  depends on the zenith angle  $\theta$ , defined w.r.t the detector, as shown in figure 4.1.

## 4.2 ABOUT THE DETECTOR

The Iron CALorimeter detector is the main proposed experiment at the India-based Neutrino Observatory (INO) [5]. The detector will be placed in an underground cavern beneath the West Bodi Hills in the Theni district (Tamil Nadu) in south India. It will observe the neutrinos produced in the atmosphere that reach the detector from all directions. The neutrinos coming from the top will traverse only  $\sim 10 - 15$  km of atmosphere, whereas those coming from the bottom may traverse  $\sim 10000$  km through the earth matter. The neutrinos will interact with the passive material of the calorimeter and generate a variety of particles (leptons and hadrons). The detector will observe neutrinos by observing these secondary particles. This experiment will mostly be sensitive to  $\nu_\mu$  events which produce muons ( $\mu^\pm$ ). From the curvature of muon tracks in magnetic field, their momenta as well as charge will be estimated. In the ICAL detector, while it will be possible to measure the charge and momentum of the muon very accurately, energy deposited by other particles will be estimated reasonably well without identifying these particles individually. The detector will be placed underground such that the cosmic muons do not get misidentified as muons produced by  $\nu_\mu$  interactions.

## 4.3 ATMOSPHERIC NEUTRINO FLUX AT INO

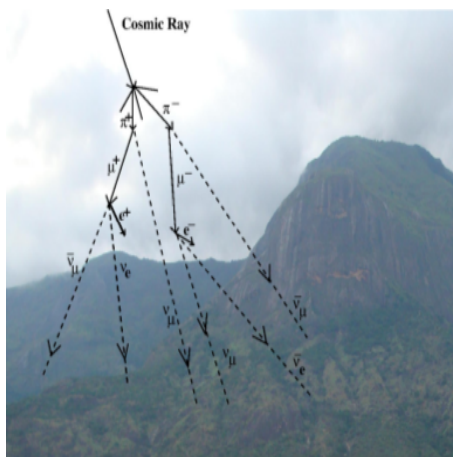


Figure 4.2.: Atmospheric neutrino and cosmic muon generation in atmosphere

Atmospheric neutrinos and cosmic muons are generated through the collision of cosmic protons with air nuclei in the upper atmosphere as described in 3.2.5. Among them, *only* neutrinos can penetrate through the mountain rocks, as shown in figure 4.2. The  $\nu$  flux falls with increasing neutrino energy  $E_\nu$ , and is symmetric in  $\cos \theta$  at higher energy, as seen in figure 4.3.

## 4.4 ICAL DETECTOR

The ICAL detector uses 50 kton of iron plates as passive elements and glass-made resistive plate chamber (RPC) detectors as active elements. Total 150 layers of RPC-s are sandwiched between 151 layers of iron plates, each of thickness 5.6 cm. There is 4

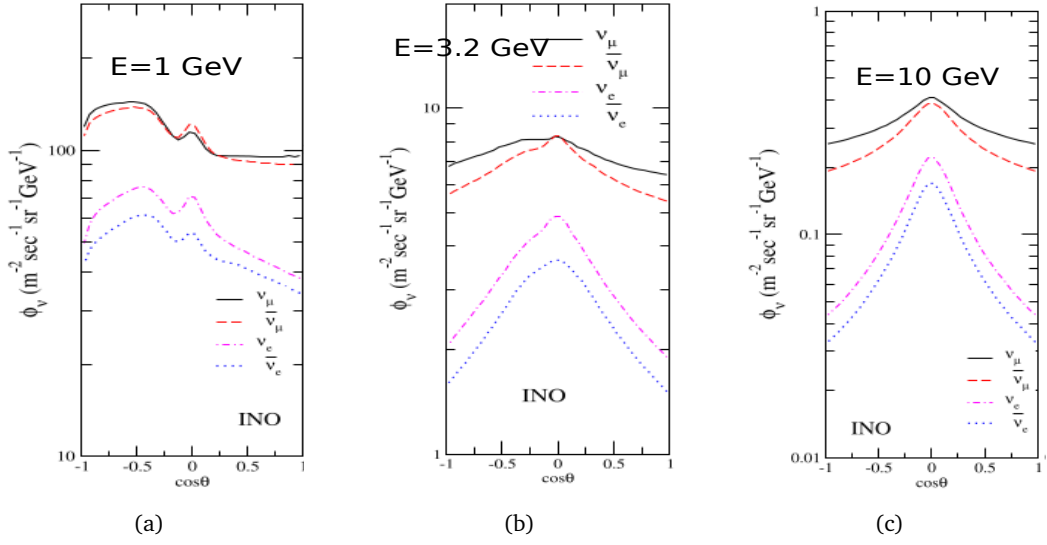


Figure 4.3.: Atmospheric neutrino flux at proposed INO site. Dependence on  $\cos\theta$  for (a)  $E = 1$  GeV, (b)  $E = 3.2$  GeV and (c)  $E = 10$  GeV. Figure taken from [2]

cm gap between two successive iron plates to accommodate the RPC layers. The total height of the detector is 14.5 m and its lateral dimension is  $48 \text{ m} \times 16 \text{ m}$ . The detector is subdivided into three modules, each with dimension of  $16 \text{ m} \times 16 \text{ m} \times 14.5 \text{ m}$ . The advantage of the modular structure is that on completion, a given module can start operating, while the construction of other modules is going on. Iron has been chosen as the passive material as it is dense, can easily be magnetized and is of low cost. The glass RPCs too are preferred to the bakelite RPCs [66] or the scintillator-PMT combinations because of lower costs. A schematic diagram of the detector and a local view of iron plate and RPC detector are shown in the following figures 4.4(a), 4.4(b). The distance between

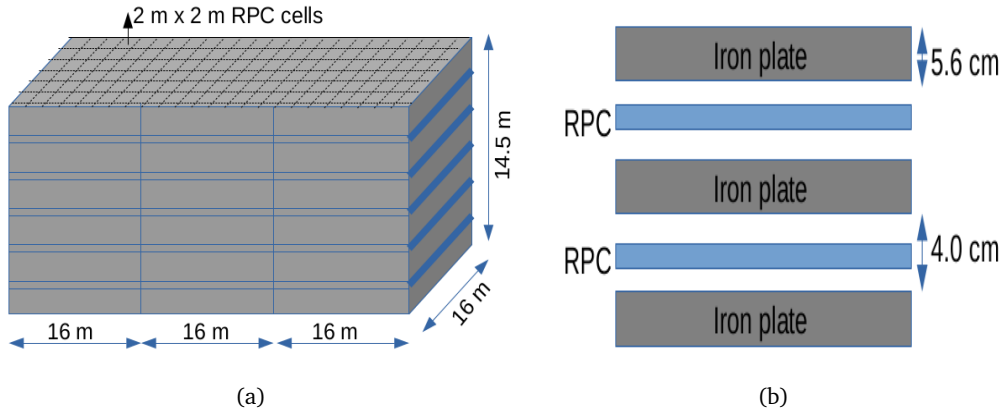


Figure 4.4.: (a) Layout of ICAL detector and (b) local view of the stack of iron plate and RPC detectors

the midpoints of every alternate RPC detectors is  $(2+5.6+2) \text{ cm} = 9.6 \text{ cm}$ . The lateral dimension of the RPC detector elements is  $(2 \text{ m} \times 2 \text{ m})$ . So, a given layer in a module accommodates total  $((16 \div 2) \times (16 \div 2)) \text{ RPCs} = 64 \text{ RPCs}$ . The iron structure is self

supporting with the layer above resting on the layer which is immediately below using iron spacers located every 2 m along  $x$ -direction. The details are shown in figure 4.5. This creates 2 m wide channels along  $y$ -direction for the insertion of RPC trays. Clearly, there are a total of 8 channels per module in a layer in one side.

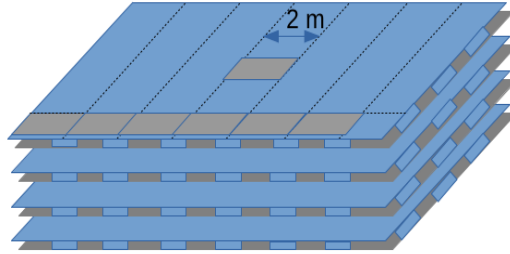


Figure 4.5.: ICAL detector and its window to atmospheric neutrinos

The whole detector setup will be surrounded by an external layer of scintillation detector or gas proportional counter. It will act as a veto layer to identify the muons which enter the detector from outside.

#### 4.5 ACTIVE DETECTOR ELEMENTS: RPC

The active detector to be used in ICAL is the RPC detector (made of commercial glass). RPC is a type of spark chamber with glass electrodes of bulk resistivity of the order of  $\sim 10^{12} \Omega\text{cm}$ . A suitable gas mixture is enclosed between the two glass electrodes which are separated by 2 mm from each other with the help of button spacers. These spacers are arranged in a regular fashion, such that the width of the gap between the glass plates remains uniform across the RPC. This allows the thickness of the gas mixture to be uniform across RPC and consequently the response of the different portions of the RPC also remains uniform. In all three modules of ICAL, a total of 28,800 RPCs are going to be used. In the following figures 4.6(a) and 4.6(b), the structure of an RPC and its cross sectional view is shown. From figure 4.6(a), it is seen that the glass plates sit on a T shaped 2 mm thick spacer on the edge of RPCs. The outer surfaces of the glass plates are painted with uniform graphite coating. This is needed to apply uniform electric field across the RPC area, by connecting the coating to external high voltage, as seen in figure 4.6(b). The copper pick up strips, arranged in  $x$  and  $y$  directions, are separated from graphite coating via insulating material. The strip width of the RPC detector to be used in ICAL is 2.8 cm, in both  $x$  and  $y$  sides. Therefore, the location of a hit due to a particle at a given plane will be known within a square of  $(2.8 \times 2.8) \text{ cm}^2$ . The intrinsic timing resolution of the detector is about 1 ns.

##### 4.5.0.1 *Avalanche mode of operation*

In ICAL, the RPC detectors will be operated in the avalanche mode. When a charged particle with reasonably high energy passes through the gas mixture trapped within the glass plates, it ionizes the gas. The resulting ions and electrons drift in the opposite directions, due to the polarity of the applied voltage. This primary ionization and resulting

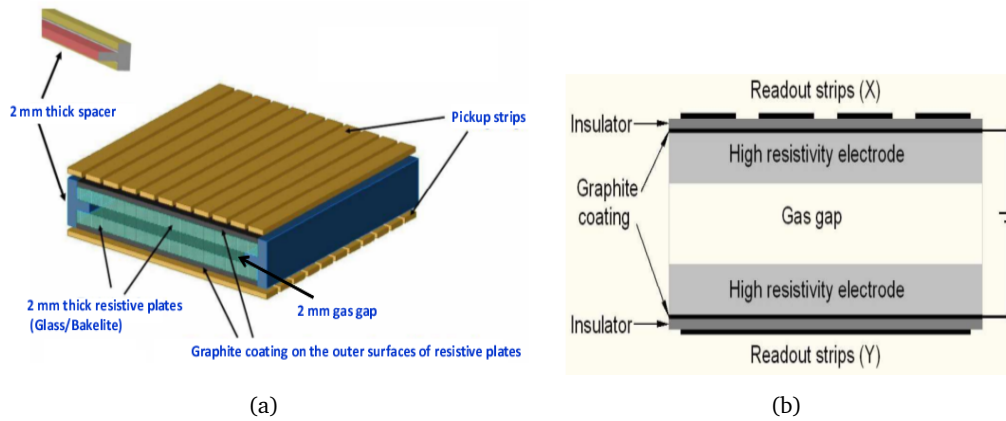


Figure 4.6.: (a) Structural view of an RPC (b) Cross sectional view. Figures adopted from [3], [4]

drift create further ionization and multiplication of charges across the electrodes. The operation mode is referred to as the avalanche mode [67] and is determined by the Townsend and attachment coefficients [12]. The motion of these charges constitute a local current that induces signal at the copper pick up strips. The signal is registered immediately, by a chain of electronic pathway to a computer. The development of the avalanche is shown in the four phases of the following figure 4.7. The pick up signal

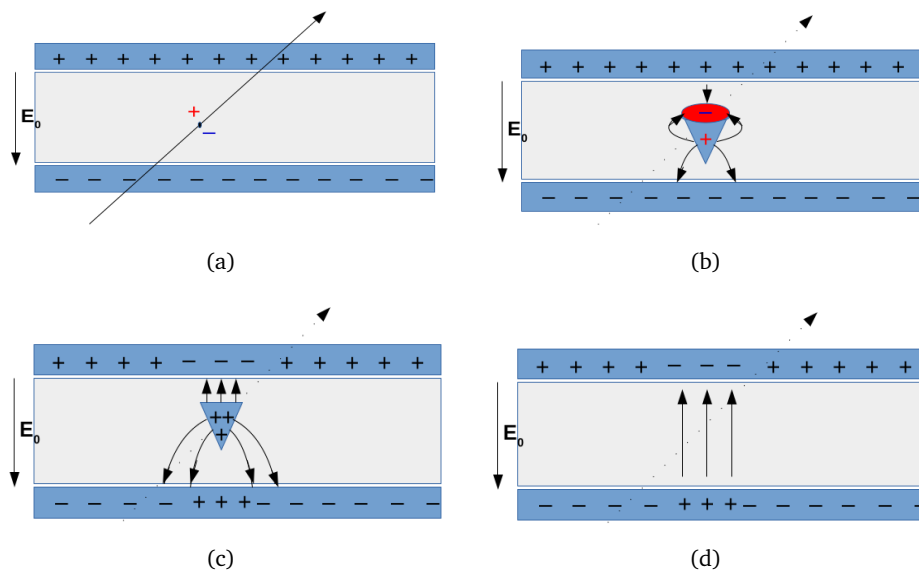


Figure 4.7.: (a) ionization due to passage of high energy particle, (b) initiation of an avalanche, (c) electrons reach the anode much faster than the ions could reach cathode, due to higher drift speed, (d) charges in the resistive layer influence the field in a small area around the position where the avalanche is developed

in the avalanche mode is only a few millivolts; so, external preamplifier circuits are used to amplify the signal by a factor of  $\sim 80$ . For the operation of RPCs in ICAL, a gas mixture of tetrafluoroethane (also called: R-134a), isobutane and  $SF_6$  is used in a

ratio of 95.5:3.9:0.60. R-134a is an eco-friendly substitute of freon. Isobutane is used to absorb photons resulting from the recombination processes.  $\text{SF}_6$  serves as the quenching gas. RPCs may also be operated in the streamer mode, in which a greater value of voltage difference is applied across the electrodes. This leads to large value of RPC-gain and localized discharges (streamers) between the electrodes. In this case, the signals are already amplified, but glass RPCs are not suitable for this mode of operation, as it might cause etches on the glass surface. Bakelite RPCs are better for streamer mode of operation.

In general, the gain of a detector is defined as  $M \equiv \frac{n}{n_0} = e^{(\alpha-\beta)x}$ , where  $\alpha$  is the first Townsend coefficient (no. of ionization/length) and  $\beta$  is attachment coefficient/length. For avalanche mode  $M < 10^8$  and degeneration due to aging is very little.

#### 4.6 ICAL MAGNET

The iron used as the passive element of the ICAL detector will be magnetized so that  $\nu$  and  $\bar{\nu}$  induced events can be separated from each other by looking at the curvature of the  $\mu^\pm$  tracks in the detector. To achieve that, every module of ICAL will be equipped with four sets of current carrying coils to generate a solenoidal magnetic field within the detector. About 60 kA current will be drawn to magnetize the iron core to  $\sim 1.5$  T. In the figure 4.8(a), we show the coil slots in the detector that accommodate the current coils. The current carrying coils will run through the coil slots completing a toroidal

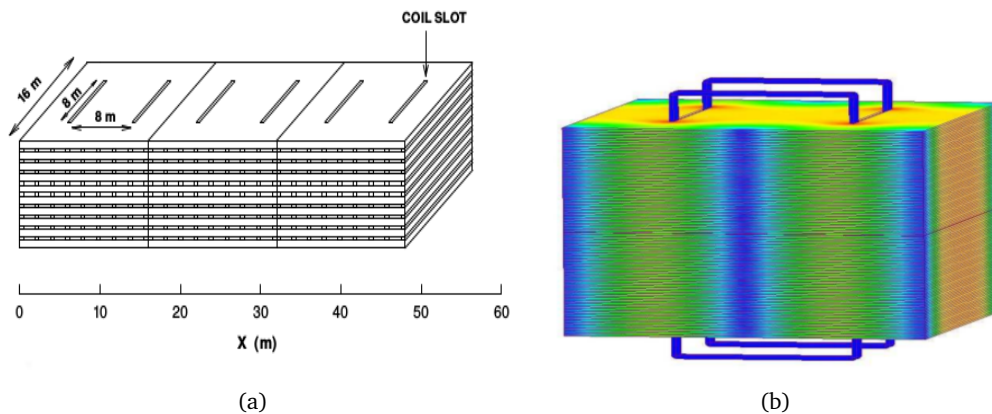


Figure 4.8.: (a) Slots for current coils in ICAL detector (b) One module of ICAL with coil inserted. Figures adopted from [5]

structure. With the proposed structure, this will be the biggest electromagnet in the world. Magnetic field so produced will be homogeneous along the y direction, parallel to the current slots. However, the field will very rapidly drop to small values at corner regions of the modules. So far, the behavior of the magnetic field has been simulated, using a commercial software called Magnet 6.0. The characteristics of the simulated field will be shown in the following chapters.

Part II.

# ICAL Simulation and Reconstruction Framework

---

## GEANT4 DETECTOR SIMULATION AND DIGITIZATION

---

### 5.1 INTRODUCTION

The analysis of real data collected at the ICAL detector can only begin when the detector is already constructed and at least one of the three detector modules is fully operational. The detector is hoped to be built in next few years within a cavern under the West Bodi Hills at the Tamil Nadu-Kerala border in South India. Therefore, all current physics analysis efforts of ICAL detector rely upon detector simulation. The GEANT4 [68] toolkit has been used to set up a framework for the fast simulation of ICAL. The main purpose of the simulation program is to simulate the tracks of different particles (generated in a neutrino event) through the detector. The program is configured to read data from NUANCE [69] in ASCII format, or from GENIE [70] in ROOT format. However, the user can also ask GEANT4 to generate tracks of muon or pion events and to simulate their signature in side the ICAL detector.

The program has the following key components: (a) virtual construction of the calorimeter along with the implementation of the inhomogeneous magnetic field map, (b) simulation using some GEANT4 physics list and digitization of the signals, (c) reconstruction using the generated signals and (d) writing down all information to an output file. The main topic of this thesis centers around the development of the reconstruction techniques for neutrino events in ICAL detector. It is an involved topic and will be discussed in detail in next two chapters. In the current chapter, however, we shall discuss about (a) and (b) that are directly related to the GEANT4 simulation.

### 5.2 DETECTOR CONSTRUCTION

#### 5.2.1 Construction of Iron CALorimeter

The first step of performing the detector simulation is to construct the detector in virtual form. The detector is a tracking calorimeter, with glass made resistive plate chamber (RPC) detectors acting as active planes and 5.6 cm thick iron slabs acting as absorbing material. The detector comprises three modules, each of (16m × 16m × 14.5m) dimension and equipped with current coils (for generating magnetic field within iron slabs), as shown in figure 5.1(a). Every active plane of any module consists of 64 2m × 2m RPCs. The design of the calorimeter is coded with GEANT4 toolkit through the `Ical0DetectorConstruction` class with the necessary parameters defined in `Ical0DetectorParameterDef` class. The instantiation of the latter is done before in the *main* program and the basic values of the parameters are fed into the program. For

example, the thickness of an iron slab, number of iron slabs in a given module, width of the RPC pick up strips, number of RPCs along the  $x$  and the  $y$  sides of an active plane in a module, dimensions of the basic components of an RPC (gas mixture, glass, graphite, copper, myler, honeycomb etc.) and its effective area are defined in this routine. A cross sectional schematic view of an RPC detector is shown again in figure 5.1(b):

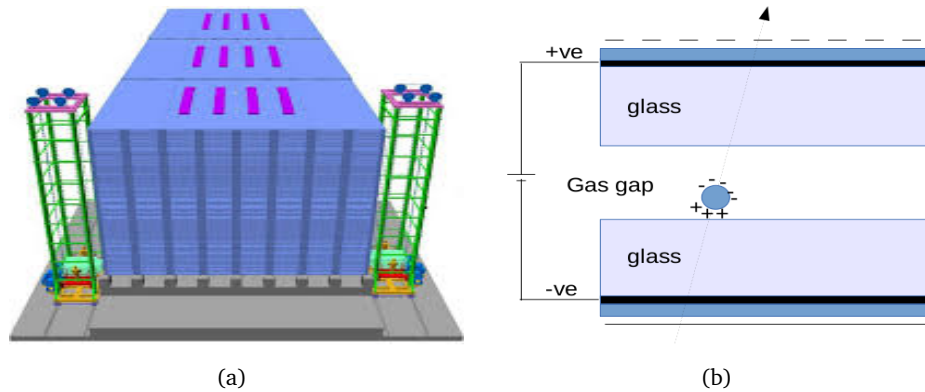


Figure 5.1.: (a) Schematic diagram of ICAL detector, (b) Cross sectional view of RPC detector

Hence, in `Ical0DetectorConstruction`, the construction of the detector is performed. First, the materials used for constructing the calorimeter are defined via GEANT4 library “G4Material.hh”. After that, various physical and logical volumes are defined. The materials for which default GEANT4 definitions are not available, were defined explicitly by providing effective atomic and mass numbers, densities, number of the component atoms or the fractions of component materials etc. Examples are `rpc gas` (including  $SF_6$ ), G10 etc. Once these are done, the GEANT4 ‘world volume’, ‘physical volumes’ and ‘logical volumes’ are defined step by step. The detector components, including the sensitive RPC detector elements, are placed at their scheduled positions. Current carrying coils are also accommodated within the frame as seen in figure 5.1(a).

There is a provision to write down the detector geometry map in a machine readable gdml file. It contains the intricate details of the materials used in construction and their boundaries. One can make use of the ROOT based TGeoManager class during reconstruction processes to find out the material and its properties at any given coordinates inside the detector. This helps in estimating the magnetic field at a location, deciding the size of a tracking step etc.

### 5.2.2 Implementation of Magnetic field

Rectangular current carrying coils (figure 5.1(a)) in ICAL detector turns the inactive iron into an electromagnet. The magnetic field map within iron has been simulated [71] by a finite element method based software Magnet 6.26 [72]. One has to give the material and dimensions of the current carrying coil and the material to magnetize (iron, in our case) as inputs to the software. Then, the  $x$ ,  $y$  and  $z$  components of the magnetic field within iron slab can be extracted at a user-chosen position. The output comes as a table in ASCII format, which can grow rather large in size if very fine resolution is sought. So, the information has been coded in a ROOT file, whose size is much less. This conversion

to ROOT reduces the file size almost to  $1/3^{rd}$  of the earlier ASCII file size. The doctoral works described in this thesis were done with magnetic field data extracted every 5cm in all directions. The  $B_z$  component of the magnetic field being very small ( $\sim 0.001$  T), it was neglected from all further considerations. Also, in ICAL simulation, the field fringing outside the iron slabs are completely neglected.

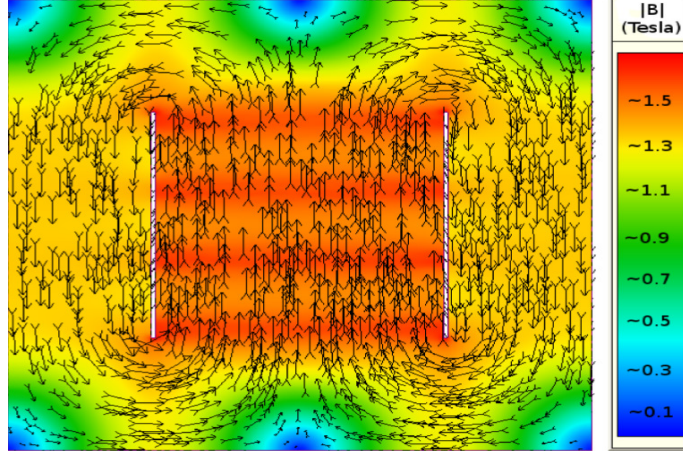


Figure 5.2.: ICAL inhomogeneous magnetic field map

For interpolation of the  $(B_x, B_y)$  components of the magnetic field in  $(x, y)$  directions, a two dimensional polynomial-function based interpolation program is used. The corresponding routine [Ical0FieldPropagator](#) was developed previously in TIFR. This code is implemented in ICAL code for performing the interpolation. For most of the regions of the detector, this routine works fine (because, the design of the current coils produces uniform magnetic field in most of the regions of the detector). However, there are regions where the magnetic field changes its sign or drops to a very small value, within a very short distance ( $\sim 10$  cm) as seen in figure 5.2. In these places, the interpolation routine fails completely. A Numerical Recipe [73] based 2D spline interpolation program was tried to counter the problem, but it did not improve the situation significantly. It was inferred that at such problematic locations, the magnetic field interpolation must be performed with a very fine mesh size, possibly of the order of 1 mm.

### 5.3 GEANT4 SIMULATION

The framework of the GEANT4 simulation is implemented in the ICAL code in such a manner that the user interacts with a easy-to-edit input configuration file to communicate with the main program. For example, the user may choose to simulate  $N$  number of single muon events of 5 GeV/c momentum randomly inside the detector. These user chosen inputs are read through the [Ical0PrimaryGeneratorAction](#) class. The interfacing of the neutrino event generators (e.g. NUANCE or GENIE) with ICAL simulation program (hereafter referred to as the ICAL code) is also performed through this class. Prior to the simulation of the  $i^{th}$  particle in a given event, the input information of the particle (e.g. its GEANT4 ParticleID, momentum, polar and azimuthal angles, coordinates of event vertex etc.) are set to GEANT4 by G4ParticleGun. These properties are treated as the attributes of a single G4Event. Then, the simulation process is started. The

process uses G4SimpleRunge library to find the trajectory of the particle in small GEANT4 steps through the detector. It calculates the magnetic field at every step using the 2D interpolation from [ICal0FieldPropagator](#) class. In a typical charged current neutrino event, there exist more than one final state particles. Each of these are simulated from the same vertex one at a time, but in the order opposite to the one listed in the input file. This is referred to as *last in, first out*. The state of the simulated particle at any point can be accessed from a GEANT4 step (G4Step) of GEANT4 based [ICal0UserSteppingAction](#) class. A flow chart of the ICAL simulation program is shown in the following figure 5.3.

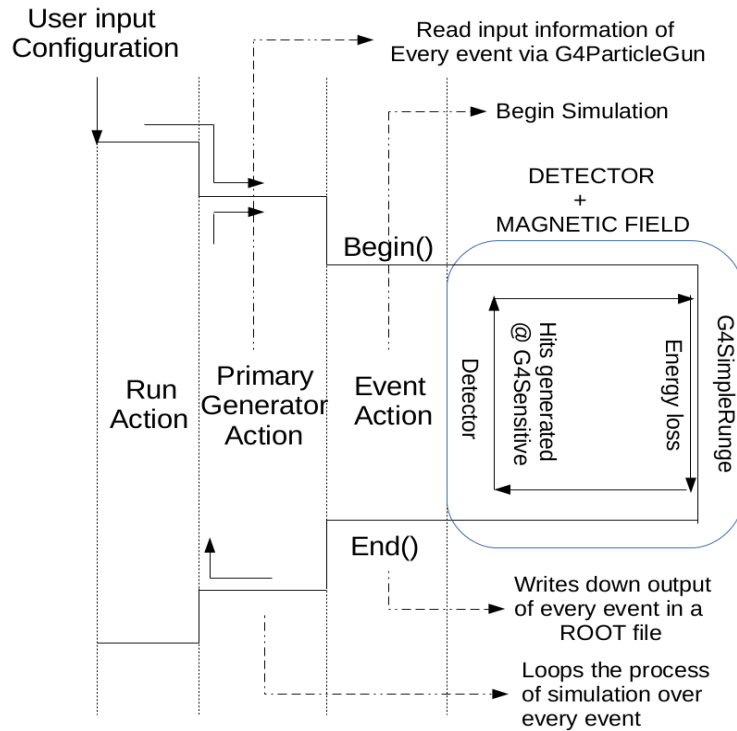


Figure 5.3.: ICAL GEANT4 simulation flow chart

### 5.3.1 Signal generation at sensitive detector

As the particle crosses the RPC detectors, it ionizes the gas and signals are generated. The exact location of the signals cannot be pin-pointed, due to finite spatial resolution of the detector. One can access the particle coordinates within the accuracy permitted by the strip width of RPC. In the ICAL simulation, the strip width has been taken as 2cm. So, given that a particle hits an RPC at a point and generates a signal, the exact location of the hit may be known within 2cm accuracy of  $i^{\text{th}}$  strip in  $x$  direction and 2cm accuracy of  $j^{\text{th}}$  strip in  $y$  direction. Once the simulation of an event is finished, the measured data will be composed of two sets:  $X[Z] := \{(x_1, t_1), (x_2, t_2) \dots (x_n, t_n)\}$  and  $Y[Z] := \{(y_1, t'_1), (y_2, t'_2) \dots (y_n, t'_n)\}$ . These signals come from measurements done along various  $Z$  planes of the detector. The timing measurements ( $t_i$ ) of signals in  $X$  and  $Y$  sides are independent. We only expect that for a given hit, the  $Z$  planes of  $X$  and  $Y$  sets will be the same, measurements along  $x$  and  $y$  directions will come from the

same RPC and their timing values will be very close to each other, if not identical. The difference in time is expected because the ICAL RPC design allows independent time measurements in  $X$  and  $Y$  directions, and the timing resolution of RPC is  $\sim 1 - 1.5$  ns.

In a given event there can be as many as hundreds of measurements, specially if the event is associated with many hadrons. To keep track of all these signals, useful or not, we digitize them. This basically means to keep track of all the relevant integral coordinates associated with the measurement. For example, it may occur at  $97^{th}$   $Z$  plane of the central module of ICAL detector; at the  $m^{th}$  RPC in  $x$  side, at the  $n^{th}$  RPC in  $y$  side; at the  $i^{th}$   $x$ -strip and  $j^{th}$   $y$ -strip in that RPC. Each measurement can be assigned a unique identification number for a given event using shift bit register method. Thus, the data arrives the experimenter in this coded form and he/she must decode it back to obtain the raw data.

The user can access the signals generated in RPC through the [ICal0Cal0SD](#) class. In fact, the digitization and coding of the signals generated in RPC are also done in this program only. There is provision to enable noisy strips that would randomly create some hits (representing electronic noise) in the detector. The simulation has been done such that the hit detection efficiency of the RPC detector is zero near its edges ( $\sim 8$  cm from the edges has been made inactive). This is done followed by the laboratory observations done at TIFR. This way, a framework for a realistic simulation has been employed in ICAL code.

---

TRACK RECONSTRUCTION I: PATTERN RECOGNITION

---

The RPC detectors, employed at the Iron CALorimeter, register hits when the high energy charged particles pass through their active regions. Apart from the charged particles, many times the electronic noises also yield stray hits. To remove such noise hits of lower pulse heights, a signal threshold has been suggested. If the pulse height is less than 20 millivolt, the hit is taken to be coming from electronic noise. The hits with higher pulse heights have been found to be coming from genuine high energy cosmic muons by laboratory tests of RPC stack at TIFR. Hence, unless the height of the pulse of a given hit crosses the threshold of 20 millivolt, the corresponding hit is not taken into consideration. The only information which is stored is whether or not a hit has been registered at a given RPC strip at some point of time. The information is at the digital level and no analogue information about the pulse height/shape or charge/energy deposit is kept. Therefore, the hits due to muons are identical to the hits due to hadrons and noise. This feature makes the job of event reconstruction more difficult, because adequate no. of correctly identified hits are essential for optimum performance of muon track fitting/hit-energy calibration of hadrons. Incorrect identification leads to poor estimation of muon track curvature and poor momentum estimation. Hence, a robust algorithm is necessary that can (a) separate the hits due to muons from those due to hadrons to a good accuracy and (b) form the tracks, presumably coming from muons. Algorithms that perform (a), i.e. assign a group of measurements to individual particles, are referred to as pattern recognition programs [74, 75]. This is followed by (b) track finding [14]. In ICAL simulation these two things are done together.

These algorithms vary from one experiment to another because the design of the detector, observed interactions, hit distribution and the reconstruction techniques are different in every experiment. In ICAL detector, the charged current weak interactions due to the muon neutrinos of energy range  $E_\nu > 0.5$  GeV will be observed. In this broad energy range, there is a nuance of neutrino interaction types (e.g. quasi elastic, single pion, resonant, diffractive, deep inelastic scatterings). The spectrum of energy of the neutrinos, no. of hadrons in the final state of interactions, energy spectrum of the final state particles vary widely in all these different types of interactions. The track finder/pattern recognition algorithm must be able to cope up with hits coming from all such neutrino events; for instance, (a) the events are at very high zenith angles ( $\theta_\nu \rightarrow 90^\circ$ ) in which tracks are almost parallel to detector planes (with very less no. of measurements) and the hadron showers spread across the RPCs, and (b) the events are almost perpendicular to the detector planes ( $\theta_\nu \rightarrow 0^\circ$  or  $180^\circ$ ) in which sometimes the portions of the tracks disappear due to passage through the vertical column of inactive regions of the detector. We wish the algorithm to yield the optimum performance in all these cases for  $\theta_\nu \in [0, 180^\circ]$ .

The existing [InoTrackFinder](#) code was based on [14] used in MINOS experiment. However, the performance of the program was not validated before for full neutrino event reconstruction. In the case of full event reconstruction, the program has to deal with the hits due to muons and the hits due to hadrons, as said before. When this was attempted, the performance of reconstruction was seen to worsen a lot as compared to the case where no hadrons were simulated. In fact, the no. of fitted muon tracks were found to increase by  $\sim 10\%$ , whereas majority of these tracks were contributed by pions ( $\pi^\pm$ ) or protons ( $p^+$ ). Hence, the program was revised and was rewritten in the form of a new C++ class: [InoPatternRecognition](#). The basic outline of the algorithm is the same as in [InoTrackFinder](#), but the implementation has been made ingeniously. Once a track is already formed, it is fitted with a Kalman filter based fitting program and the track parameters are obtained. This will be covered in detail in the next chapter. In the present chapter, the pattern recognition program will be described in detail and its performance will be shown.

## 6.1 A BRIEF OUTLINE OF THE ALGORITHM

The algorithm processes all the available hits (which have pulse heights greater than a predefined threshold) in an event and inspects all possible combinations of these hits to form an identifiable track. Initially smaller track segments are prepared; formation of a final track is contingent upon smooth associations among these small segments. The unsuccessful attempts for forming even the small track segments mean to be dealing with hits due to hadrons, as usually, hadrons form shower of hits. The successful association of track segments followed by appending one segment to another, lead to increase in the length of the chain of the segments and finally, a seed [InoTrack](#) is formed. The formed track when tested is found to be consisting of hits mostly from muon. This track is fitted as a muon track.

The figure 6.1(a) shows a typical neutrino event generated by NUANCE generator. As the final state particles are simulated through the detector, the measurements are done along their paths. These measurements (hits) are denoted by the small red boxes in this figure. The diffused cloud of red boxes represents the hits due to hadrons close to the vertex of the up-going event. On the other hand, the encircled hits on the longer track are due to the muon. The pattern recognition algorithm separated the possible muon hits from possible hadron hits in this event. The set of muon hits were used to fit the muon track. The hits along the fitted muon track is designed with black triangles (direction of the apex of these triangles gives the direction of the motion of the muon, as provided by the fitting algorithm).

Since, almost all the neutrino interactions happen inside iron plate (of thickness 5.6cm) and there is no way to find the point of generation of the cloud of hits due to hadrons, there is practically no access to the event vertex. Hence, the track finder algorithm does *not* start processing hits from the vertex. It also does not start from the rear end of the track, as a nice trajectory such as one in figure 6.1(a), does not exist always. Instead, it takes the whole set of measurements and starts processing them in the way explained in the following sections.

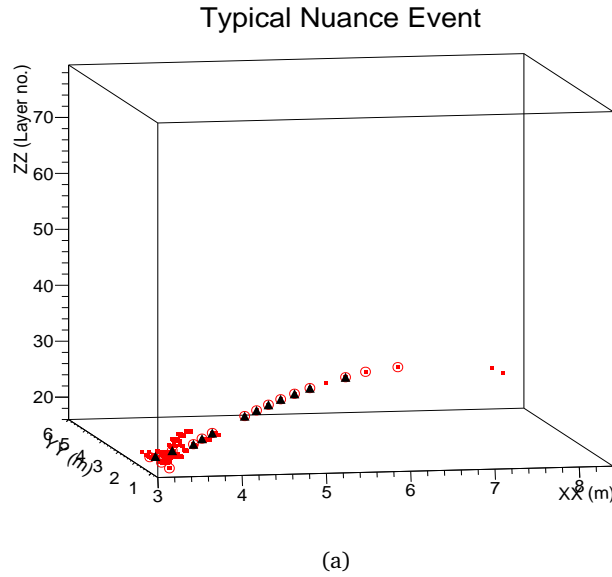


Figure 6.1.: Muon track and hadron shower of a typical NUANCE event

### 6.1.1 Forming Hits and Clusters

As explained in 5.3.1, the program works on two sets of independent measurements:  $X[Z] := \{(x_1, t_1), (x_2, t_2) \dots (x_n, t_n)\}$  along various  $Z$  layers  $\in [1, 150]$ ; and  $Y[Z] := \{(y_1, t'_1), (y_2, t'_2) \dots (y_n, t'_n)\}$ , again along various  $Z$  layers  $\in [1, 150]$ . To form a set of proper  $(x, y)$  measurements, we check the associations of each  $(x_i, t_i)$  measurement with all  $(y_j, t'_j)$  measurements. Meaningful ordered pair results when the  $x$  measurement and the  $y$  measurement belong to the same  $Z$  plane, same RPC and if the difference in timing in  $x$  channel and in the  $y$  channel is no bigger than 1ns. Under these conditions, an **InoHit** is formed. All these hits are stored in a hit bank. If in a given  $Z$  plane more than 6 hits are found, it is assumed that the plane contains a hadron shower. The hits in this plane are no longer used in the track finding.

So, all other regular planes have no. of hits  $\leq 6$ . Now, if a few hits in a layer are very much closeby (within a separation of 3 strip-widths), it makes sense to *cluster* them and consider the cluster as a single object. Distant stray hits are clustered as well. This reduces the no. of objects to be dealt with in every  $Z$  plane for formation of triplets, segments etc. with practically no loss of information. If the formation of triplets etc. were to be done with hits, the process would be computationally intensive and the chances of errors would be more. Thus, a typical **InoCluster** has one or a few hits (close to each other). At any point of time, individual hit(s) of a cluster may be accessed to know its (their) whereabouts (position, timing etc).

In figure 6.2(a), hits in all the  $Z$  planes except the one marked by a red cross ('X') are used. The abandoned plane clearly has more than 6 hits and can be said to be having a shower of hits. It is practically impossible to identify the hit due to muon among all the hits in the shower. One can try to make an educated guess about the *right* hit from the hits in the immediate next layers (up and down). However, often these layers too contain showers, unlike what is shown in the figure 6.2(a). Even if there are no showers in the immediate next planes, the inclusion of the hits in the abandoned plane leads to

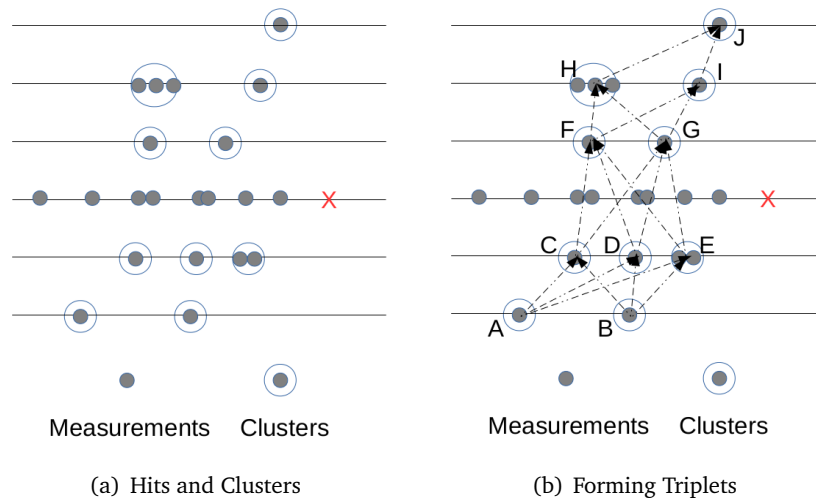


Figure 6.2.: formation of (a) Hits and Clusters and (b) Triplets

considerable ambiguity regarding the proper combination of hits and clusters, as we shall see next. The clusters, formed by close enough hits, are denoted by bigger circles in the figure.

### 6.1.2 Forming Triplets

The next step towards forming a track is to check all possible combinations of clusters. The process is illustrated in figure 6.2(b). Each cluster in a layer is connected to all possible clusters in the immediately next layers. Slopes of all these small line segments are calculated. A set of *any three* clusters in three consecutive planes with measurements are allowed to form a *triplet*, only if the difference in the slopes of constituent small line segments (joining two clusters) is less than  $15^\circ$ . Triplets represent the closest approximation to straight line segments having three points on it. Referring to figure 6.2(b), the following combinations of clusters form triplets: A-C-G, B-D-G, C-F-H, C-G-I, D-G-I, G-I-J among 28 possible combinations. Unless each of these possibilities is tested individually, the possible combination of the appropriate clusters along the muon track cannot be identified. Forming triplets from clusters also reduces the no. of to be dealt with objects. The triplets are the basic building blocks of an [InoTrackSegment](#) object. Hence, all triplets are filled into a vector [Triplets](#) of type *pointers to [InoTrackSegment](#) class*.

### 6.1.3 Joining Triplets and Forming Segments/Track-lets

The next step is to start forming a chain of triplets which will look like a segment of a track (track-let) from the set of all available triplets. An arbitrary element of the vector [Triplets](#) is first assigned to: [ChainTriplets](#), a pointer to [InoTrackSegment](#) class. The association of this triplet with every other triplet (called [TestTriplet](#), belonging to [Triplets](#) vector) is checked. The [TestTriplet](#) with appropriate association is appended to existing [ChainTriplets](#), thereby increasing the length of the chain. In the next iteration the association of this [ChainTriplets](#) is tested with every *unused* triplets; and the right

association again increments the length of **ChainTriplets**. The process continues until all the triplets are exhausted.

### 6.1.3.1 Conditions for acceptable association of triplets

Three situations that may arise are shown in figure 6.3(a), 6.3(b) and 6.3(c). In the first case, the rear end of the first segment has  $Z$  coordinate greater than the  $Z$  coordinate of the front end of the second triplet. If overlapping of *two* clusters are found between the two segments, only then the **TestTriplet** is appended to the **ChainTriplet**. The condition ensures that the directions of the two segments are more or less the same.

In the second case, the  $Z$  coordinate of the rear end of the first segment is the same as the  $Z$  coordinate of the front end of the second segment. As shown here 6.3(b), there may or may not be overlapping of single cluster between the segments in this case. The **TestTriplet** is appended to the **ChainTriplet**, if (a) the last cluster of first segment is identical with the first cluster of the second segment and (b) the slope of the rear end of the first segment is close to the slope of the **TestTriplet**. The relative angular separation between two segments must be less than  $15^\circ$ .

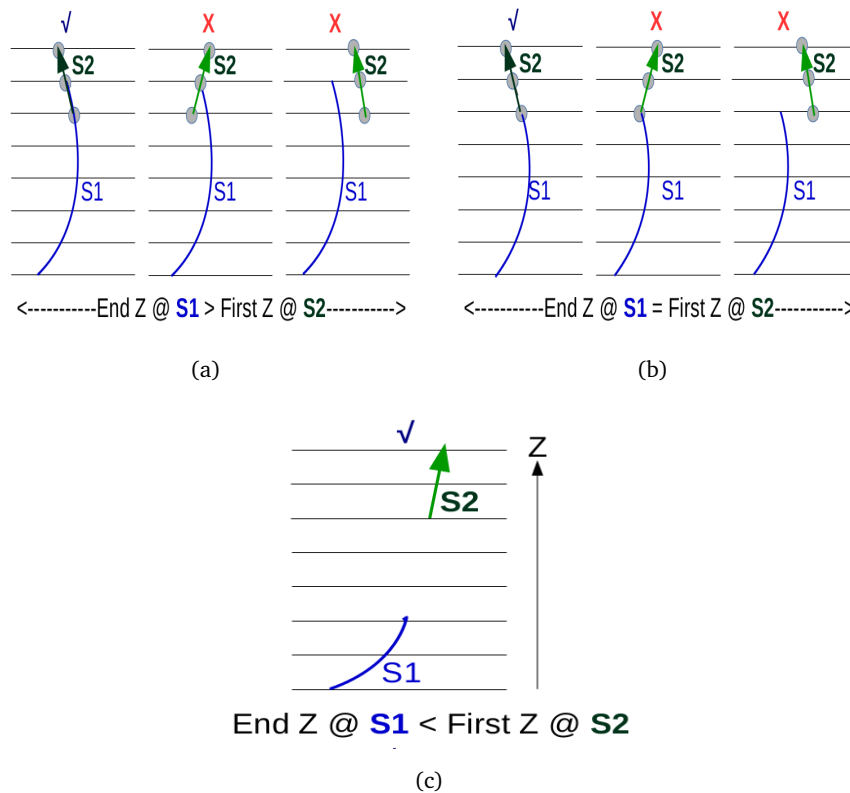


Figure 6.3.: formation of (a) Hits and Clusters and (b) Triplets

The third possible situation appears if the  $Z$  coordinate of the rear end of the first segment is less than the  $Z$  coordinate of the front end of the second segment. In this case, there is a region along the track where no measurements were available (typically due to passage of particles through inactive regions of the detector). In such case, if the slopes of the two segments are not very different, the **TestTriplet** is appended. Once the segment **ChainTriplets** has at least 5 clusters, an **InoTrack** is formed and it is overwritten

repeatedly as long as the length of **ChainTriplets** increases. Usually only a few no. of segments are formed with all the available clusters.

In figure 6.3(a), 6.3(b) and 6.3(c), these association techniques are illustrated. The existing **ChainTriplets** is represented by **S1** and the triplet under examination is denoted by **S2**. If the association is successful (unsuccessful), the corresponding figure is marked with a  $\checkmark$  ( $\times$ ).

#### 6.1.4 Forming a track and shower

With these few track segments, a longer **InoTrack** is formed. If two or more tracks results, then the one with greater length of chain is selected as the muon track. This track is used for track fitting assuming that all its constituent hits were due to muon. The whole process is illustrated in figure 6.4(a).

The left over hits in the shower-planes, in unsuccessful triplets and in track segments are assumed to be due to particles other than muon. Usually, they are  $\pi^\pm$ ,  $e^-$  and  $p^+$ . So, all these hits taken together, are said to form hadron shower.

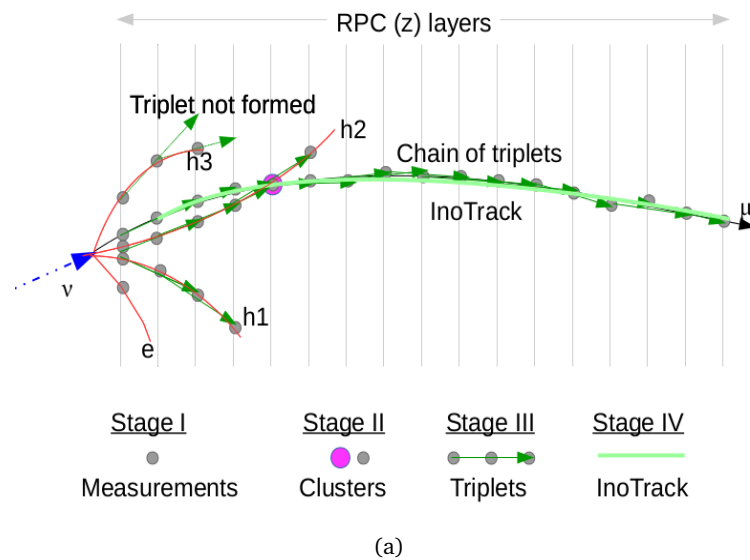


Figure 6.4.: Muon track and hadron shower of a typical NUANCE event

## 6.2 SETTING THE PROPERTIES OF THE SEED TRACK

The sensitivity of the experiment depends directly on the performance of reconstruction algorithm. The most important aspect of reconstruction is track fitting; and estimation of charge, momentum and direction of the out-going particle (muon, in case of ICAL). To perform the fit, a recursive least square method (Kalman filter) is employed. This will be described in detail in the next chapter 7. Here, it suffices to say that the filter starts with a seed track, formed by the pattern recognition program. To start the fitting, certain properties of the seed track are needed. These are discussed in the following.

### 6.2.1 *Z direction of motion*

In ICAL, the adopted convention is to fit the track starting from terminal close to the event vertex and reaching up to the rear end of the track. In order to do that, we need to identify whether the muon is up-going or down-going. Unless the muon track is almost horizontal (i.e. almost parallel to the RPC planes), this direction also represents the direction of motion of the parent neutrino (whether up-going or down-going). This is an important issue, because if wrong direction is given as input to the Kalman filter, the charge is wrongly reconstructed by virtue of the Lorentz force law.

The direction of a muon (whether up-going or not) is determined from the timing data of the clusters (forming the muon track). Once an event occurs and the trigger [76] criterion is satisfied, the clock is set on. It starts registering the timing data zero upwards, for all legitimate hits in that event. If the timing of the  $X$ -signal is different from that of  $Y$ -signal in a given hit, the average value of the time stamps is taken while constructing the [InoCluster](#). The direction of the [InoTrack](#) is determined from the sign of  $dT/dZ$  where  $T(Z)$  denotes the set of timing data measured along different  $Z$  coordinates of the clusters along the track. The first derivative of  $T(Z)$  would reveal whether or not timing data increased as  $Z$  coordinates increased in this event.

It was chosen to fit  $T(Z)$  with a linear function  $f(Z) = a + bZ$ . The corresponding least squares fitting formulae are readily available [77]. The expression of the slope for  $n$  measurements (clusters) along the track is given by:

$$b = \frac{dT}{dZ} = \frac{n \sum_{i=1}^n Z_i T_i - \sum_{i=1}^n Z_i \sum_{i=1}^n T_i}{n \sum_{i=1}^n Z_i^2 - (\sum_{i=1}^n Z_i)^2} \quad (33)$$

The direction of the muon is given by the sign of  $\frac{dT}{dZ}$ . Unless very small no. of measurements ( $< 7-8$ ) are available, this model works fine. If a non-linear function  $f(Z) = a + bZ + cZ^2 + \dots$  were used, perhaps the fit would be better. But the calculation of slope would be ambiguous due to explicit dependence of  $\frac{dT}{dZ}$  on  $Z$ .

### 6.2.2 *Vertex position of the seed track*

The end of the track closer to the event vertex is identified once the direction of the muon track is found. Now, the fitting process requires a vertex position of the seed to start with. Usually, the experimenter employs a pattern recognition routine to find out the cluster nearest to the vertex (he does not have access to the true vertex position). The position of this cluster, which belongs to the formed track, is taken as the vertex position of the seed track. In this work, the position of the lowermost (or, uppermost) cluster of the [InoTrack](#) has been used as the starting position of the up-going (or, down-going) seed track.

### 6.2.3 *Calculation of $t_x$ and $t_y$*

To employ the prediction formulae, the fitting program also needs the slope of the seed track near the point where it starts operating. In ICAL, the slopes  $t_x = \frac{dX}{dZ}$  and  $t_y = \frac{dY}{dZ}$  are calculated at the event vertex, from the projections of the track on  $X-Z$  and  $Y-Z$  planes respectively. Clusters in the immediate neighboring  $Z$  planes are used to calculate

the slopes locally. A linear fitting function  $X = X_0 + t_x Z$  (similarly,  $Y = Y_0 + t_y Z$ ) is used to fit the relevant portion of the curve projected on  $X - Z$  ( $Y - Z$ ) plane. Although the fitting program presently starts from the event vertex, options have been kept to find the local slopes at any cluster on the track. The calculation of  $t_x$  is given by:

$$t_x = \frac{dX}{dZ} = \frac{n \sum_{i=1}^n Z_i X_i - \sum_{i=1}^n Z_i \sum_{i=1}^n X_i}{n \sum_{i=1}^n Z_i^2 - (\sum_{i=1}^n Z_i)^2} \quad (34)$$

For  $t_y$ , similar expression is used. The slope at the vertex/rear end of the track is found from five nearest clusters (including itself) along the track. If slope is sought at a point in the middle of the track, say at  $i^{th}$  plane, the calculation has to be performed with the positions of the 5 clusters between  $(i-2)^{th}$  plane and  $(i+2)^{th}$  plane (including themselves).

#### 6.2.4 Fully/partially contained events

The following conditions were developed to separate the partially contained (PC) events from the fully contained (FC) events, assuming that the event vertices are all confined within the detector. The events can escape the detector only from the top/bottom planes or from side boundaries. Those [InoTracks](#) that have maximum/ minimum  $Z$  coordinate within two layers from the top/bottom  $Z$  boundaries, are supposed to be PC events. On the other hand, if the terminal  $X(Y)$  position of an event, extrapolated through two more  $Z$  layers, leads to a point outside the detector boundary, that event is also taken to be a PC event. In all the other cases, events are assumed to be FC.

#### 6.2.5 Events in dead/inactive space

There also exist events for which the muon tracks come out of/ go into the vertical inactive spaces in the detector. This typically happens at the boundary of two RPCs. It is not possible to know what length they traverse inside that region. It was seen that these tracks pass almost vertically through the edge of the RPCs, just before getting lost. This observation was employed to single out such events through a function [InoPatternRecognition::IfInDeadSpace\(\)](#). Separation of these events are vital, as they are fitted nicely otherwise, with momentum estimated less, compared to the true value. Inclusion of these events worsens the accuracy of the momentum estimation.

#### 6.2.6 Calculation of standard error of measurements

The filtering process requires the measurement error. As the exact position of a hit is not known within an RPC-strip, it makes sense to *assume* that the whole stretch of the strip is equally likely to get struck by the particle. In other words, the probability of being hit by a charged particle is uniform across the width of the strip. If the RPC strip width is

given by  $a$ , the corresponding standard deviation is given as  $\sigma(x) = a/\sqrt{12}$ , as shown below:

$$\begin{aligned}
\sigma^2(x) &= \frac{\int_{-a/2}^{a/2} \rho(x)(x-\bar{x})^2 dx}{\int_{-a/2}^{a/2} \rho(x) dx} \\
&= \frac{C \int_{-a/2}^{a/2} x^2 dx}{C \int_{-a/2}^{a/2} dx} (\because \bar{x} = 0, \rho(x) = C) \\
&= \frac{a^2}{12}
\end{aligned} \tag{35}$$

### 6.3 PERFORMANCE OF THE PROGRAM

The performance of the pattern recognition program must be validated by quantifying its ability (a) to separate the hits due to muons from those due to hadrons, (b) to provide meaningful inputs to the Kalman filter and (c) to reject the background neutral current events. In this work, neutrino events were generated with NUANCE [69]  $\nu$  event generator, using atmospheric neutrino flux at Super Kamiokande site provided by the Honda group [78], as the flux at INO site was still not available. The following results were obtained for charged current events of neutrino energy  $E_\nu \in [0.5 - 100]$  GeV.

Before the performance plots are shown, it is helpful to have a picture of the neutrino input data set which was used in this work. The following figure 6.5(a) shows the NUANCE level 2 D distribution of momentum (GeV/c) and  $\cos \theta$  of neutrinos (black

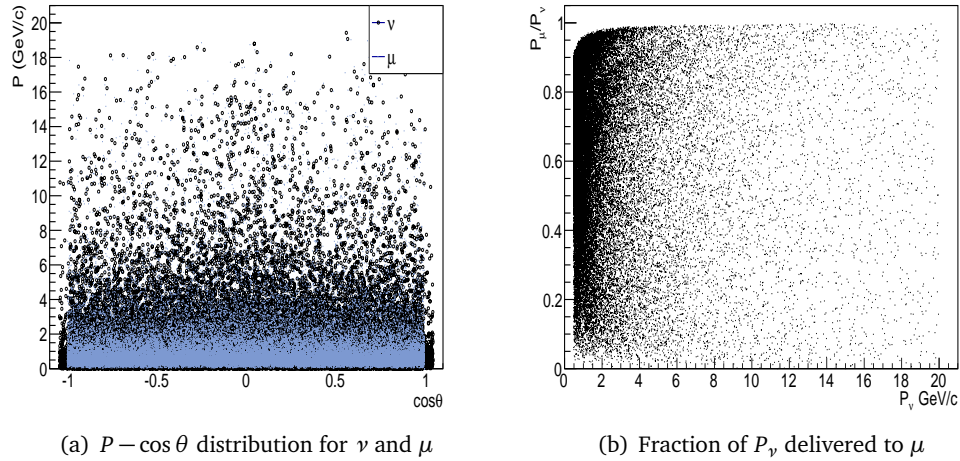


Figure 6.5.: (a) Distribution of neutrinos/muons in  $P - \cos \theta$  plane and (b) fractional momentum delivered to muons vs incident neutrino momentum

circles) and muons (blueish gray dots). The dense accumulation of events *below* 2 GeV/c (for *all* values of  $\cos \theta$ ) shows that majority of the events are very low energy events. This is expected since the atmospheric neutrino flux reaches maximum beneath  $p_\nu = 1$  GeV/c. The fraction of the neutrino momentum that is delivered to the muon is shown in figure 6.5(b), as a function of incident neutrino momentum. Thus, for a considerable

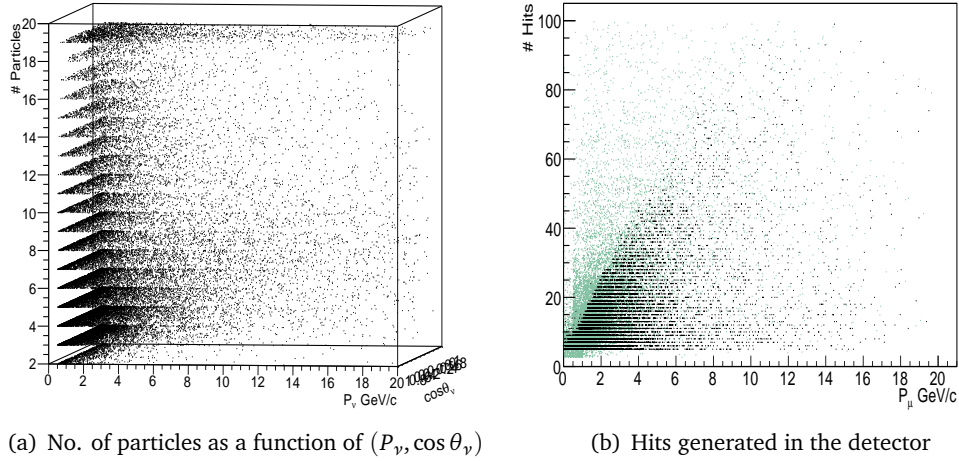


Figure 6.6.: (a) No. of final state particles, produced in the neutrino interactions, shown as a function of  $P_\nu$  and  $\cos \theta_\nu$ , (b) no. of hits in the detector generated by these particles.

no. of charged current events, muons carry only a fraction of the neutrino energy. The rest of the energy is shared among all the other particles, produced in the interaction. Typically these particles are  $p^+$ ,  $\pi^\pm$  and photons ( $\gamma$ ). The no. of all final state particles ( $\mu$  and others) is shown in figure 6.6(a), as a function of  $P_\nu$  and  $\cos \theta_\nu$ . It is interesting to note that there may be  $> 15 - 20$  particles produced in events with lower incident momentum  $P_\nu \sim 1 - 5$  GeV/c. Among these, the particles which have electric charge, generate hits in the detector if they have sufficient energies. Specifically, particles in the near-horizontal direction (i.e. particles that are produced almost parallel to active  $Z$  planes of the detector) result in a lot of hits because of the cross talks among the RPC channels. Large no. of hits is also expected in an event if there are *many* particles in the final state. The no. of hits due to muons is usually a fraction of all possible hits in an event. In the figure 6.6(b) the hits due to muons (black dots) and the total no. of hits (green dots) in every event have been shown. The diffused distribution of hits with increasing muon momentum  $P_\mu$  reflects a wide variation in the no. of hits at any given  $P_\mu$ .

### 6.3.1 Neutral current background rejection performance

In neutral current events, there are no muons and thus, no tracks are expected. Usually, these events are characterized by the absence of track like objects and diffused hadron shower. They can be easily separated from most charged current events with a muon track. However, in few cases energetic protons of neutral current events give short tracks. In such cases, the pattern recognition program cannot distinguish them from muon tracks in other charged current events. With the pattern recognition program, that allows a track to be formed if there are *at least* five clusters in five different layers, 1.7% neutral current events lead to such short tracks. It is observed that if a cut of 7  $Z$  layers is devised, the background reduces to  $\sim 0.05\%$ . However, this would also remove a large no. of muon tracks coming of charged current events (as can be seen from figure 6.6(b)).

Anyway, the full NUANCE data sample comprises the charged current and neutral current events in  $\sim 100 : 40$  ratio. Therefore, the overall background due to neutral current events in a mixed data sample would be  $\sim 0.7\%$ .

### 6.3.2 Degree of muon-hadron separation

One method to assess the goodness of the pattern recognition program is to quantify the degree of correct identification of muon hits among all the hits used to form the ‘muon track’. The histogram of the ratio of the *no. of correctly identified muon hits* to the *no. of all hits included in the track* is plotted in the following figure 6.7(a). On the other hand, the histogram of the *fraction of genuine muon hits, incorrectly included in the hadron shower*, is shown in figure 6.7(b).

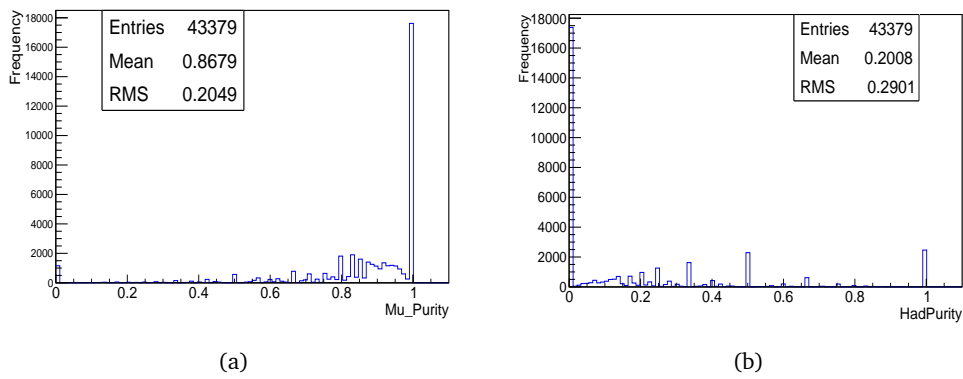


Figure 6.7.: Performance of the pattern recognition program: (a) degree of correct identification of muon hits in a muon track and (b) fraction of incorrect inclusion of muon hits in hadron shower

### 6.3.3 Estimation of correct direction of the particle

Since the time resolution of the RPC is rather poor ( $\sim 1$  ns), the identification of correct Z direction of motion is not so easy. A typical example is shown in the table:

Plane no.	X strip no.	Y strip no.	time(ns)
35	660	454	1.3
36	660	455	-0.1
37	660	457	1.3
38	660	459	3.7
39	660	460	2.0
40	659	462	0.5
41	658	463	-0.3
45	656	466	1.6

Clearly, it is not possible to guess the correct direction just by a mere glance at the data. With the process described in 6.2.1, it is seen that  $> 96\%$  cases, one can find the correct direction. However, the process does not work (a) if the measured data do not exhibit *any* monotonicity at all along the track (i.e. fluctuates w.r.t. the  $Z$  planes); or (b) if the  $Z$  direction of motion of the track is flipped due to bending in magnetic field. In this case also, setting a cut-off of higher no. of layers reduces the total no. of events; and hence, is not a practical solution.

#### 6.3.4 Properties of seed track: input to track fitter

If the input variables to the Kalman filter are close to the true values, that leads to better performances of the filter and vice versa. Inputs  $(x, y, t_x, t_y)$  which are away from true values, tend to drive the track fitting in wrong direction, picking up values of magnetic field at wrong places etc. This affects the process of track reconstruction. In the following figures 6.8(a), 6.8(b), 6.8(c) and 6.8(d), the residual (difference between the properties at the vertex of the genuine muon track and the seed track) distributions are shown.

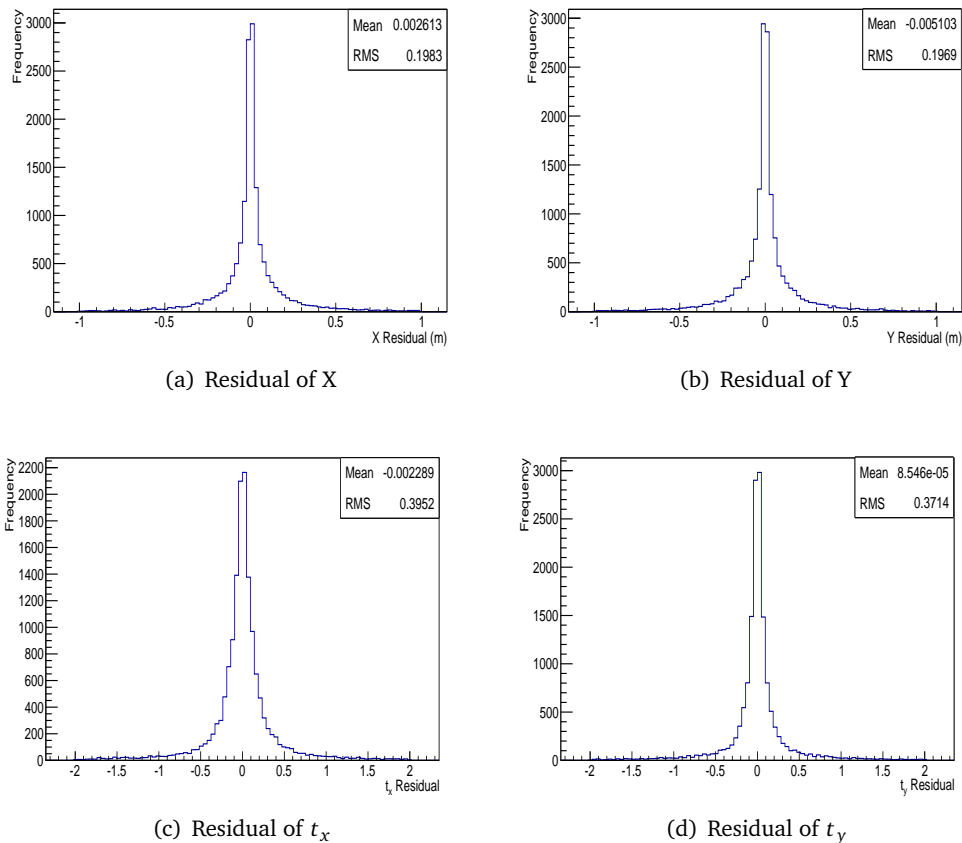


Figure 6.8.: Residuals distributions of (a)  $X$ , (b)  $Y$ , (c)  $t_x$ , (d)  $t_y$ .

The seed values estimated by the program were used for track fitting. This is described in detail in the following chapter.

---

## TRACK RECONSTRUCTION II: TRACK FITTING

---

The data measured in HEP experiments in the form of electronic signals typically come from the particles generated in some scattering processes/interactions. Kinematic properties of these particles must be estimated and energy-momentum conservation laws must be applied to understand the interactions better or to test some hypotheses. This estimation may involve reconstruction and/or calibration techniques depending upon the type of the detector. When it is possible to identify and form one or more tracks in an event, they are reconstructed using some standard procedure. When that is not possible, the kinematic observables can be calibrated against the measured electronic form of data.

For the charged current (CC)  $\nu_\mu$  interactions in ICAL, it is possible to have tracks in the detector. Almost in all cases, these tracks come from muons. The job of the pattern recognition program is to isolate the measurements along the track from hadron shower, and to form a seed track. In the preceding chapter, it was seen that the corresponding program developed for INO-ICAL can separate the hits due to muons from the hits due to hadrons, to some accuracy and can form a seed track if different conditions (section 6.1) are met. The measurements done along the seed track are fitted with some model and the optimum set of track parameters (charge of the particle, its momentum and direction at various  $Z$  layers etc.), that best explains the measured data, is determined. Muon ( $\mu$ ) tracks can thus be reconstructed with reasonably good momentum and direction resolution. However, the same cannot be done with the hadron shower. They can at the best be calibrated with poorer energy resolution [13]. Thus, more accurate information can be found from the reconstruction of muon tracks only and hence, it is very important.

During track finding, the hits were processed from a geometric perspective. But, for track fitting, the motion of the particle through the detector needs to be considered. Thus, the issues like bending of the track in the magnetic field, energy loss and multiple (Coulomb) scattering etc. are taken into account. A recursive least square fitting technique, called as Kalman filter [79] is employed to process the measured data in conjunction with these physical information (bending in magnetic field, energy loss etc.) to determine the state of the particle at various points along the track. Even from a set of incomplete and noisy measurements, the filter can extract the momentum and direction of the particle with good enough accuracy. For a linear system, Kalman filter estimates have zero bias and minimum variance [80]. However, the problem of tracking in HEP experiments is described by nonlinear equations, as we shall see later. In this case, an extended form of linear Kalman filter is applied and the performances are near-optimal.

In this chapter, we shall describe the Kalman filter package implemented in reconstruction framework of ICAL code. In section 7.1, a qualitative picture of the process will be shown. Many important concepts like track model, weighted averaging of data and

prediction, filtering, smoothing etc. will be introduced in this section. Then, each of these concepts will be dealt in detail in the following section 7.2. The implementation of these to ICAL will be the subject of section 7.3. In the next section 7.4, the performances of this package will be described for single muon events, generated by GEANT4 toolkit [68]. In the second part of this section, the performances of reconstruction for full neutrino events (generated by NUANCE [69]) will be discussed. This will validate the full reconstruction program (pattern recognition as well as the track fitter) for full neutrino events. These results will be the groundwork of the neutrino mass hierarchy sensitivity analysis. In the last part of this section, the hadron energy calibration of the (CC)  $\nu_\mu$  events will be shown. The dependence of the track fitting performances on the magnetic field, RPC strip-width etc. in ICAL will be described in the following section 7.5. Although they were not used for the physics analyses, still they help to assess the kind of efforts needed for improved reconstruction. We shall conclude with a section 7.6 where the structure of the reconstruction program will be described through flow charts.

### 7.1 QUALITATIVE PICTURE OF THE PROCESS

In the problem of track fitting, the state of the dynamical system (particle in motion) at every measurement site is specified by a set of five numbers [80] known as a track model. Usually, this set contains the information about the instantaneous position, direction and momentum. Depending on the structure of the detector and the observed tracks, an experiment chooses a representation of the track model to work with. In some cases, the no. of elements in the track model can also be different from five [16]. All the information about the particle motion can be extracted from the track model, which is also called a state vector in the Kalman filter terminology. In the context of INO-ICAL, the elements of the state vector are specified at fixed  $Z$  coordinates, at various layers of sensitive detectors. A convenient choice of the state vector is  $(x(z), y(z), t_x(z), t_y(z), q/p(z))$ , where  $x(z)$  and  $y(z)$  denote the position,  $t_x$  and  $t_y$  denote the instantaneous slopes in  $X-Z$  and  $Y-Z$  planes and  $q/p(z)$  denotes the signed inverse momentum at every  $Z$  layer.

For track fitting, a theoretical model of the evolution of the state vector is constructed. If the state is specified at a given measurement site, this model *extrapolates* the state to future measurement sites. Thus, the construction of  $\chi^2$  between the prediction and the measurement becomes possible. The Kalman filter equations are calculated by minimizing this  $\chi^2$ . Let us illustrate the idea with the help of the following figure 7.1.

In this figure, the sensitive detectors (RPCs) are represented as vertical planes (colored in gray) parallel to each other. The measurements, shown with black boxes, are fitted with a theoretical model that takes into account the bending of the track in the magnetic field, the energy loss, multiple Coulomb scattering etc. The predictions of this model at every  $Z$  plane with measurements are denoted by red colored stars. The filtering is performed at every measurement site in the forward direction (i.e. in the direction of motion). In this figure, if we assume that the particle moves to the right, and the direction of its motion is correctly found by the track finder 6.2.1, then the prediction and filtering would be performed also towards the right, starting from the leftmost measurement. The choice of the direction of filtering is nothing but a convention. One can also perform the filtering process towards the left without any harm. But, in ICAL the first convention has been used. When the filtering is finished for all the measurements in the seed track,

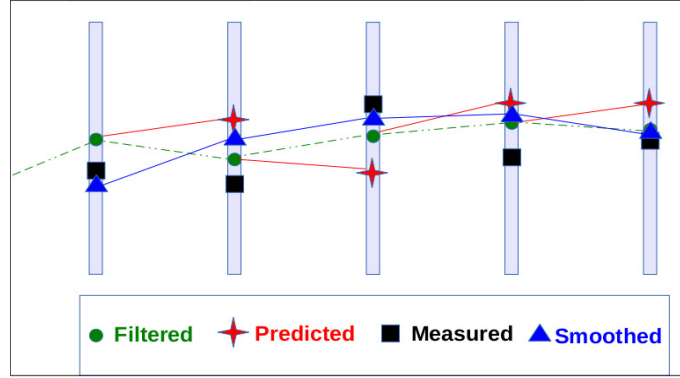


Figure 7.1.: Qualitative view of Kalman filtering and smoothing procedure

they are fitted in the reverse direction. This process, known as smoothing, is denoted with blue triangles in the figure 7.1. The smoothing process is supposed to *smooth* the filtered track. At the end of the smoothing, one reaches the measurement site which is perhaps the closest measurement to the event vertex and also obtains a near optimal estimate of the parameters of the track (e.g. charge, momentum, direction) and their errors.

Let us assume that the particle position is experimentally measured at  $x_m$  with an error of  $\sigma_m$  at some sensitive detector; and that the theoretical model predicts that the particle position at  $x_p$  with an error  $\sigma_p$ . Then, it is straightforward to verify that the weighted average ( $x_f$ ) of the prediction ( $x_p$ ) and the measurement ( $x_m$ ) is given by:

$$\begin{aligned}
 x_f &= \frac{\frac{1}{\sigma_p^2}x_p + \frac{1}{\sigma_m^2}x_m}{\frac{1}{\sigma_p^2} + \frac{1}{\sigma_m^2}} \\
 &= \frac{\sigma_m^2}{\sigma_p^2 + \sigma_m^2}x_p + \frac{\sigma_p^2}{\sigma_p^2 + \sigma_m^2}x_m \\
 &= (1-K)x_p + Kx_m
 \end{aligned} \tag{36}$$

-where  $K$  is a +ve gain factor that decides the relative weights of the measurement ( $x_m$ ) and the prediction ( $x_p$ ) in the filtered estimate ( $x_f$ ). Notice that  $\sigma_p \rightarrow \infty$  implies  $x_f \rightarrow x_m$  and vice versa. This means that higher error in either of measurement or prediction forces the estimate towards the one with less error. The opposite case, i.e.  $\sigma_m \rightarrow \infty$  realizes when no measurement is available at a sensitive detector. In this case, the prediction  $x_p$  is the automatic choice for the estimate  $x_f$ . This averaging process shrinks down the error of the estimation as shown below:

$$\begin{aligned}
 \frac{1}{\sigma_f^2} &= \frac{1}{\sigma_m^2} + \frac{1}{\sigma_p^2} \\
 \text{i.e. } \sigma_f^2 &= \left(1 - \frac{\sigma_p^2}{\sigma_m^2 + \sigma_p^2}\right)\sigma_p^2 \\
 &= (1-K)\sigma_p^2
 \end{aligned} \tag{37}$$

One can easily check that the variance of the estimation  $\sigma_f^2 < \min(\sigma_m^2, \sigma_p^2)$ . Kalman filter in the context of track fitting does the same thing with 5 element state vector  $\mathbf{x}_k$  and 2 element measurement vector  $\mathbf{m}_k$  at every  $k^{\text{th}}$  measurement site. Weighted average of the prediction  $\bar{\mathbf{x}}_k$  and the measurement  $\mathbf{m}_k$  gives the filtered estimate  $\hat{\mathbf{x}}_k$ . The details is shown in the next section.

## 7.2 KALMAN FILTER FORMALISM IN HEP EXPERIMENTS

### 7.2.1 Nomenclature of quantities

The *true* state vector  $\bar{\mathbf{x}}_k$  contains *all* possible information about the particle as it passes through the detector. The elements of  $\bar{\mathbf{x}}_k$  evolves as the particle moves through the detector according to a systematic *equation of motion* and suffers from *random disturbances* like multiple scattering etc. We seek to obtain the best estimate of the true state vector  $\bar{\mathbf{x}}_k$  at a point from the information collected from multiple observation sites within the detector. The equation that describes the evolution of the state vector  $\bar{\mathbf{x}}_k$  at measurement site  $k$ , from the state vector  $\bar{\mathbf{x}}_{k-1}$  at measurement site  $(k-1)$  is given as:

$$\bar{\mathbf{x}}_k = f_{k-1}(\bar{\mathbf{x}}_{k-1}) + \mathbf{w}_{k-1} \quad (38)$$

where  $f_{k-1}(\bar{\mathbf{x}}_{k-1})$  is a non-linear state propagator function corresponding to a smooth deterministic motion assuming that the random process noise  $\mathbf{w}_{k-1}$  is absent. Typically,  $f_{k-1}$  contains the information about the energy loss and deflection of the particle in magnetic field. In a dense medium, the random process noise  $\mathbf{w}_{k-1}$  comes from multiple scattering and energy loss fluctuations [21]. Clearly,  $\mathbf{w}_{k-1}$  is also a 5 dimensional column vector, whose elements change in a random fashion. It is assumed that the process noise has no bias  $\langle \mathbf{w}_{k-1} \rangle = 0$  and has a covariance given as [15]:

$$Q_{k-1} = \langle \mathbf{w}_{k-1} \mathbf{w}_{k-1}^T \rangle_{5 \times 5} \quad (39)$$

Another aspect of the experiment is the measurement of the *observables* at sensitive planes of the detector. The digitized positions of the measurements at each  $k^{\text{th}}$  layer form the measurement vector  $\mathbf{m}_k$ . For example, in ICAL,  $\mathbf{m}_k = (x(z_k), y(z_k))^T$  at every sensitive layer  $z_k$  along the particle trajectory. The relation between the state vector and the measurement vector is called a *measurement equation*:

$$\mathbf{m}_k = h_k(\bar{\mathbf{x}}_k) + \mathbf{e}_k \quad (40)$$

where  $h_k(\bar{\mathbf{x}}_k)$  gives the true measurement in case the measurement noise  $\mathbf{e}_k$  is absent. In general,  $h_k(\bar{\mathbf{x}}_k)$  is also a nonlinear function. The noise is given by a 2 dimensional column vector  $\mathbf{e}_k$  whose elements represent intrinsic detector spatial resolution. We assume that the measurement noise is unbiased  $\langle \mathbf{e}_k \rangle = 0$ ; and its covariance is given by:

$$V_k = \langle \mathbf{e}_k \mathbf{e}_k^T \rangle_{2 \times 2} \quad (41)$$

With an estimate  $\mathbf{x}_k$  for the true state  $\bar{\mathbf{x}}_k$ , the estimation error covariance matrix is defined as:

$$C_k = \langle (\mathbf{x}_k - \bar{\mathbf{x}}_k)(\mathbf{x}_k - \bar{\mathbf{x}}_k)^T \rangle_{5 \times 5} \quad (42)$$

### 7.2.1.1 Nomenclature for routines

The algorithm is based on a set of routines. To follow them, it is important to understand the notations that express the underlying recurrence relations. The work begins with:

prediction: this step predicts the state vector at site ( $k'' > k$ ) based on the observations made at sites up to ( $k$ ):

$$\mathbf{x}_{k''(>k)}^k \mid \{\mathbf{m}_{k'}, k' \leq k\} : \text{future}$$

filtering: this step updates the predicted state vector at site ( $k$ ) based on the observations made at sites up to ( $k$ ) by adding the observation at site ( $k$ ):

$$\mathbf{x}_{k''(=k)}^k \mid \{\mathbf{m}_{k'}, k' \leq k\} : \text{present}$$

smoothing: this step improves the filtered state vector at site ( $k'' < k$ ) by using all the observations made at sites up to ( $k$ ):

$$\mathbf{x}_{k''(<k)}^k \mid \{\mathbf{m}_{k'}, k' \leq k\} : \text{past}$$

That is, the suffix ( $k''$ ) means *at the site* ( $k''$ ); the superfix ( $k$ ) means *from the measurements done up to the site* ( $k$ ). The mathematical formalism of the Kalman filtering will be explained using these notations in the rest of this chapter. The following examples will further clarify the matter:

$\mathbf{x}_k^i$	estimate of $\bar{\mathbf{x}}_k$ using measurements at sites up to ( $i$ ) <sup>th</sup> site.
$C_k^i$	covariance matrix for $\mathbf{x}_k^i$ , defined as $\langle (\mathbf{x}_k^i - \bar{\mathbf{x}}_k)(\mathbf{x}_k^i - \bar{\mathbf{x}}_k)^T \rangle_{5 \times 5}$
$\mathbf{r}_k^i$	residual of measurement, defined as $(\mathbf{m}_k - h_k(\mathbf{x}_k))$
$C_k^i$	covariance matrix for $\mathbf{r}_k^i$ .

When the superfix and the suffix are identical, the superfix will be omitted. For instance, the filtered estimate at site ( $k$ ) achieved from information of all the measurements done up to site ( $k$ ), is given by  $\mathbf{x}_k^k \equiv \mathbf{x}_k$ . Similar convention is adopted for all other vectors and matrices as well.

### 7.2.2 Prediction to next site with a measurement

Given a realistic estimate of the state vector at measurement site ( $k-1$ ), one would like to *predict* the state at the site ( $k$ ) containing the next measurement, according to Eq. (38). However, it is not possible to know the increment of every element of the state vector due to the random vector  $\mathbf{w}_{k-1}$ . The best one can do is to carry out the prediction using only the first term of the RHS of Eq. (38). Hence, the estimated/initialized state vector  $\mathbf{x}_{k-1}^{k-1} \equiv \mathbf{x}_{k-1}$  at site ( $k-1$ ) is extrapolated to:

$$\mathbf{x}_k^{k-1} = f_{k-1}(\mathbf{x}_{k-1}) \quad (43)$$

in the next measurement site ( $k$ ). Similarly, it can be shown that the extrapolated error covariance matrix at site ( $k$ ) is given by:

$$C_k^{k-1} = F_{k-1} C_{k-1} F_{k-1}^T + Q_{k-1} \quad (44)$$

where  $F_{k-1}$  is a  $5 \times 5$  propagator matrix defined as  $F_{k-1} = \frac{\partial f_{k-1}}{\partial \mathbf{x}_{k-1}}$ . From Eq. (44), it is seen that the predicted error matrix  $C_k^{k-1}$  at ( $k$ )<sup>th</sup> site is the sum of two terms. The term  $F_{k-1} C_{k-1} F_{k-1}^T$  describes how the errors at the ( $k-1$ )<sup>th</sup> site is propagated to the ( $k$ )<sup>th</sup> site by the propagator  $F_{k-1}$ . This is deterministic error propagation, because the propagated errors can be expressed in terms of magnetic field and energy loss of known behavior. The second term of Eq. (44) adds the contribution of random errors to the total propagated error. Hence, when the tracking algorithm reaches the ( $k$ )<sup>th</sup> site, the total predicted error matrix is *inflated* compared to its initial value.

### 7.2.3 Filtering the estimate at the current site

We want to update the predicted state vector  $\mathbf{x}_k^{k-1}$  [which is calculated from the observations made at sites up to ( $k-1$ )] at site ( $k$ ) by including the observation at site ( $k$ ). Thus, we want to get the optimal estimate of the state vector at site ( $k$ ) with all the information collected so far. To do that, the incremental  $\chi^2$  is defined between ( $k-1$ )<sup>th</sup> plane and ( $k$ )<sup>th</sup> plane, and is given by:

$$\Delta \chi^2 = (\mathbf{x}_k - \mathbf{x}_k^{k-1}) [C_k^{k-1}]^{-1} (\mathbf{x}_k - \mathbf{x}_k^{k-1})^T + (\mathbf{m}_k - h_k(\mathbf{x}_k)) [V_k]^{-1} (\mathbf{m}_k - h_k(\mathbf{x}_k))^T \quad (45)$$

The  $\Delta \chi^2$  is minimized w.r.t.  $\mathbf{x}_k$ , to obtain the optimal Kalman filtered estimate at  $k$ <sup>th</sup> plane, in terms of ( $5 \times 2$ ) Kalman gain matrix  $K_k$ , given as:

$$K_k = C_k^{k-1} H_k^T (H_k C_k^{k-1} H_k^T + V_k)^{-1} \quad (46)$$

where the projector matrix  $H_k$  is given by  $H_k = \frac{\partial h_k}{\partial \mathbf{x}_k^{k-1}}$ . In terms of Kalman Gain matrix  $K_k$ , the filtered state estimate for  $k$ <sup>th</sup> plane is:

$$\mathbf{x}_k = \mathbf{x}_k^{k-1} + K_k (\mathbf{m}_k - H_k \mathbf{x}_k^{k-1}) \quad (47)$$

Similarly, the Kalman estimate for filtered error covariance  $C_k$  is given by:

$$C_k = (I - K_k H_k) C_k^{k-1} \quad (48)$$

Then,  $\mathbf{x}_k$  and  $C_k$  are used for extrapolation from  $k$ <sup>th</sup> plane to ( $k+1$ )<sup>th</sup> plane. The process is continued till the rear end of the track is reached. Filtering these measurements at sites  $k \in [1, N]$ , one actually obtains the fitted track. The fitted state vectors at each of these measurement sites are supposed to be the optimal estimates. It is interesting to note the similarity of Eq.(47) with Eq.(36) and that of Eq. (48) with Eq.(37).

### 7.2.4 Smoothing the fitted track

After fitting the track in the forward direction the state vector at every ( $k$ )<sup>th</sup> site can be re-evaluated and improved by applying the filter to the measurements in the reverse

direction. This process is known as smoothing. These estimates are calculated at every  $(k)^{th}$  plane ( $1 \leq k < N$ ) from *all* the measurements done at *all* the measurement sites. It can be done in two ways:-

(a) Just by running the filter in the opposite direction. In this case, *all* intermediate calculations of prediction and filtering has to be redone.

(b) By using standard smoothing equations, obtained by merging one forward filter with one backward filter. In this case, one does not calculate propagator  $F_{k-1}$  or random noise matrix  $Q_k$  at every step. However, one needs to *store* these quantities while doing the filtering in the forward direction. Using these stored information only, one defines a smoother gain matrix:

$$A_k = C_k F_k^T (C_{k+1}^k)^{-1} \quad (49)$$

at every  $(k)^{th}$  site. A smoothed quantity at  $(k)^{th}$  site is found by using all the measurements done up to  $N^{th}$  site. So, a quantity  $p$  smoothed at  $(k)^{th}$  site will be denoted as  $p_k^N$  in the recurrence relations. In terms of  $A_k$ , the smoothed state is given by:

$$\mathbf{x}_k^n = \mathbf{x}_k + A_k (\mathbf{x}_{k+1}^n - \mathbf{x}_{k+1}^k) \quad (50)$$

The corresponding smoothed estimation error covariance matrix is given by:

$$C_k^n = C_k + A_k (C_{k+1}^n - C_{k+1}^k) A_k^T \quad (51)$$

### 7.3 KALMAN FILTER IN ICAL@INO

For track fitting in ICAL@INO, the standard framework of extended Kalman filtering has been adopted. The state vector  $\mathbf{x} = (x, y, t_x, t_y, q/p)^T$  is very convenient to work with in the rectangular Cartesian system used in ICAL. The rectangular geometry of ICAL detector helps in the choice of the coordinates. The measurement vector  $\mathbf{m}_k$  is defined as  $\mathbf{m}_k (x(z_k), y(z_k))^T$  at every measurement site  $z_k$ . The mean value of  $\mathbf{x}$  is extrapolated to the next layer using Eq. 43. The function  $f_{k-1}$  is actually the solution of the equation of motion of a charged particle in inhomogeneous magnetic field in a dense medium, where the particle loses its energy as it moves. Usually, in tracking problems the solution is determined from Runge Kutta 4 [18] method or using helix model [15]. Recently, analytic iterative solutions of the problem has been developed by Gorbunov et al. [18]. For prediction in ICAL, these solutions have been calculated and used in this work. Given the state vector at  $\mathbf{z}_o$ , one can find the state vector at  $\mathbf{z}_e$  after appropriately adding or subtracting the energy loss. Apart from the mean values of the state vector, its associated errors are also propagated from an older  $z$  layer to an extrapolated  $z$  layer, using the propagator matrix  $F = \frac{\partial f_k}{\partial \mathbf{x}_{k-1}}$ :

$$F_{k-1} = \begin{bmatrix} \frac{\delta[x(z_e)]}{\delta x(z_o)} & \frac{\delta[x(z_e)]}{\delta y(z_o)} & \frac{\delta[x(z_e)]}{\delta t_x(z_o)} & \frac{\delta[x(z_e)]}{\delta t_y(z_o)} & \frac{\delta[x(z_e)]}{\delta(\frac{q}{p}(z_o))} \\ \frac{\delta[y(z_e)]}{\delta x(z_o)} & \frac{\delta[y(z_e)]}{\delta y(z_o)} & \frac{\delta[y(z_e)]}{\delta t_x(z_o)} & \frac{\delta[y(z_e)]}{\delta t_y(z_o)} & \frac{\delta[y(z_e)]}{\delta(\frac{q}{p}(z_o))} \\ \frac{\delta[t_x(z_e)]}{\delta x(z_o)} & \frac{\delta[t_x(z_e)]}{\delta y(z_o)} & \frac{\delta[t_x(z_e)]}{\delta t_x(z_o)} & \frac{\delta[t_x(z_e)]}{\delta t_y(z_o)} & \frac{\delta[t_x(z_e)]}{\delta(\frac{q}{p}(z_o))} \\ \frac{\delta[t_y(z_e)]}{\delta x(z_o)} & \frac{\delta[t_y(z_e)]}{\delta y(z_o)} & \frac{\delta[t_y(z_e)]}{\delta t_x(z_o)} & \frac{\delta[t_y(z_e)]}{\delta t_y(z_o)} & \frac{\delta[t_y(z_e)]}{\delta(\frac{q}{p}(z_o))} \\ \frac{\delta[q/P(z_e)]}{\delta x(z_o)} & \frac{\delta[q/P(z_e)]}{\delta y(z_o)} & \frac{\delta[q/P(z_e)]}{\delta t_x(z_o)} & \frac{\delta[q/P(z_e)]}{\delta t_y(z_o)} & \frac{\delta[q/P(z_e)]}{\delta(\frac{q}{p}(z_o))} \end{bmatrix} \quad (52)$$

After the extrapolation step, the filter equations Eq. (47), (48) etc. are applied to find the optimal estimate. In the context of ICAL, the projector matrix  $H_k$  is given as [81]:

$$\begin{pmatrix} 1 & 0 & 0 & 0 & 0 \\ 0 & 1 & 0 & 0 & 0 \end{pmatrix}$$

and the  $(2 \times 2)$  measurement error matrix  $V_k$  is:

$$\begin{pmatrix} \sigma_x^2 & 0 \\ 0 & \sigma_y^2 \end{pmatrix}$$

where  $\sigma_x = \sigma_y = \frac{d}{\sqrt{12}}$ ,  $d$  being the strip-width of RPC detector 6.2.6. The Kalman estimate for filtered error covariance  $C_k$  is intentionally calculated as:

$$\begin{aligned} C_k &= (I - K_k H_k) C_k^{k-1} && \text{not to use} \\ &= (I - K_k H_k) C_k^{k-1} (I - K_k H_k)^T + K_k V_k K_k^T \end{aligned} \quad (53)$$

Evaluation of the filtered error by Joseph's form [82] has the advantage that this form is numerically more stable. If the error matrix is not updated by Eq. (53), is updated by Eq. (48), the intermediate calculations sometimes show -ve diagonal element in the error covariance matrix. It is a known issue in Kalman filter literature [83], [84] and is solved by using Joseph's form of the same equation.

### 7.3.1 Track following method

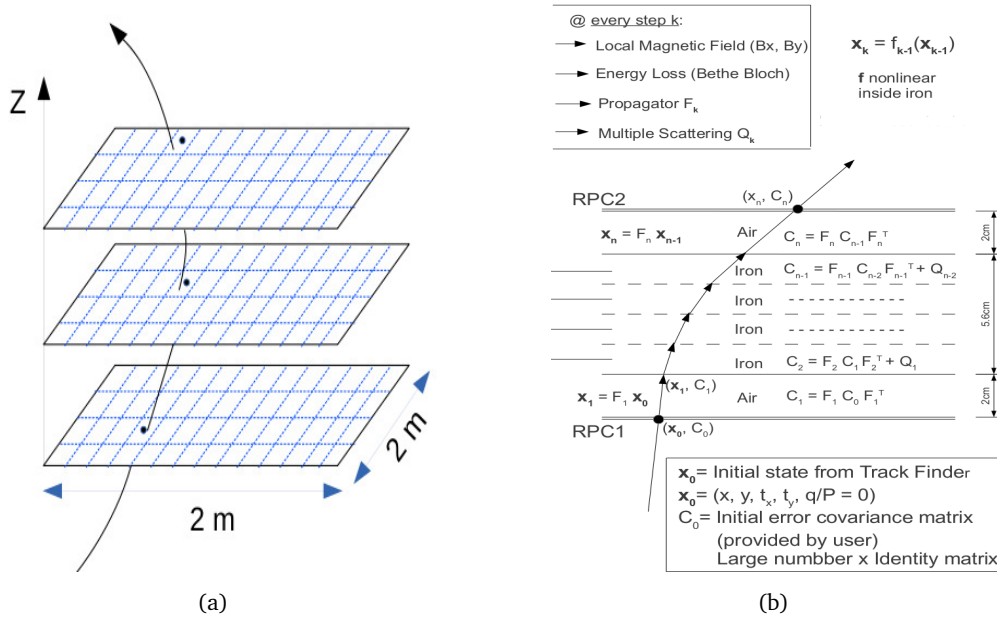


Figure 7.2.: (a) Schematic diagram of a track and (b) tracking steps between RPC planes

The figure 7.2(a) shows the schematic diagram of a track passing through a few sensitive detector layers. The course of track following is shown in figure 7.2(b). The coordinates of the InoCluster (formed from the digitized 'hit') found closest to the vertex

are used to initialize  $(x, y)$  elements of the filter. The slopes  $t_x$  and  $t_y$  near this vertex are calculated by using the method described in section 6.2.3). The element  $q/p$  is initialized to zero, thereby nullifying any initial bias. The error covariance matrix  $C$  is initialized to an identity matrix, multiplied by a huge number. This is done to ensure that the filter converges quickly. However, this type of initialization is seen to lead to numerical instability in some cases. This is also reported by the pioneer authors in this field [85]. It is seen that, the frequency of occurrence of this problem becomes less if the  $C$  matrix is initialized to a small identity matrix, with diagonal elements typically of the order of  $\sigma_x^2 = \sigma_y^2 = d/12$ . However, in this case the filter proceeds to the convergence rather slowly. After the filter starts working, the estimated momentum drops very slowly from very high initial values (as  $q/p$  is initialized to zero in the first place). This cannot be avoided even if one starts with a smaller estimate of initial momentum. The high value of tracking momentum makes the particle bend less in the magnetic field and deviates the particle from its true trajectory. The result is poor extrapolation and delay in convergence. Therefore, initialization with bigger values is adopted.

By taking steps  $\Delta z$  in  $z$  direction, the state vector  $\mathbf{x}(z + \Delta z)$  is predicted from the state  $\mathbf{x}(z)$ . In every step, first the local material and magnetic field is found; then, the step size is decided. Inside iron layers,  $\Delta z$  is set to 1 mm and in other materials  $\Delta z$  is set according to their widths. Energy loss of the particle in a step is calculated using Bethe Bloch formula [86] along with density effect corrections. The prediction of the  $q/P$  element of the state vector is done using the energy loss information in that material. In every step, the propagator matrix (Eq.(52)) and the random noise matrix are calculated locally, using the material and the magnetic field. They are used to propagate the errors associated with the state elements. Now, as tracking is done from one hit to the next through a series of thick and dense materials, Eq.(44) cannot be directly used between two hits. It has to be used repeatedly in each successive steps so that starting from  $(k-1)^{th}$  hit, the random error contribution to the total error at  $k^{th}$  hit becomes (Eq.(3.16) in [15]):

$$Q_{k-1} = \sum_{s=1}^{N-1} F_{m_s,k} Q_{m_s} F_{m_s,k}^T \quad (54)$$

In Eq.(54),  $F_{m_s,k}$  and  $Q_{m_s}$  are the Jacobian matrix and the noise matrix for a small step. This step is also explained in figure 7.2(b). Then, the Kalman gain matrix  $K_k$  (Eq.(46)) is calculated from  $C_k^{k-1}$ ,  $V_k$  and  $H_k$ . It is used for obtaining filtered state [from Eq.(47)] and updated error covariance matrix [from Eq.(53)].

After all the hits in the muon track candidate have been filtered, the hits are processed in the reverse order using the same algorithm. This procedure *smooths* the fitted track. The two methods indicated in section 7.2.4 were tested separately. The performances in these two methods are more or less the same. The processing of hits in the forward and backward directions, completes one iteration. We have used four iterations, though for  $> 90\%$  cases, the *fractional* change in the desired state vector estimate were seen to become  $< 10\%$  after the 2nd iteration. For tracks with only 4–5 hits convergence is not at all achieved after four iterations.

### 7.3.2 State and error propagation for $(x, y, t_x, t_y)$

We have calculated the expressions for  $x(z_e)$ ,  $y(z_e)$ ,  $t_x(z_e)$  and  $t_y(z_e)$  in terms of  $[x, y, t_x, t_y, q/P](z_0)$  and the magnetic field integrals, according to the model outlined in [18]. The analytic solutions were calculated up to the third order ( $n = 2$  in  $(q/P)^n$  with  $n = 0, 1, 2, 3, \dots$ ). They were utilized to find the derivatives required by the propagator matrix.

$$x(z_e) = x(z_0) + t_x dz + h(t_x t_y S_x - (1 + t_x^2) S_y) + h^2[t_x(3t_y^2 + 1)S_{xx} - t_y(3t_x^2 + 1)S_{xy} - t_y(3t_x^2 + 1)S_{yx} + t_x(3t_x^2 + 3)S_{yy}] \quad (55)$$

$$y(z_e) = y(z_0) + t_y dz + h((1 + t_y^2)S_x - t_x t_y S_y) + h^2[t_y(3t_y^2 + 3)S_{xx} - t_x(3t_y^2 + 1)S_{xy} - t_x(3t_y^2 + 1)S_{yx} + t_y(3t_x^2 + 1)S_{yy}] \quad (56)$$

$$t_x(z_e) = t_x + h(t_x t_y R_x - (1 + t_x^2)R_y) + h^2[t_x(3t_y^2 + 1)R_{xx} - t_y(3t_x^2 + 1)R_{xy} - t_y(3t_x^2 + 1)R_{yx} + t_x(3t_x^2 + 3)R_{yy}] \quad (57)$$

$$t_y(z_e) = t_y + h((1 + t_y^2)R_x - t_x t_y R_y) + h^2[t_y(3t_y^2 + 3)R_{xx} - t_x(3t_y^2 + 1)R_{xy} - t_x(3t_y^2 + 1)R_{yx} + t_y(3t_x^2 + 1)R_{yy}] \quad (58)$$

In the above expressions,  $h = \kappa(q/P)\sqrt{1 + t_x^2 + t_y^2}$  where  $\kappa = 0.29979 \text{ GeV}c^{-1}T^{-1}m^{-1}$  and  $t_x$  and  $t_y$  refer to  $t_x(z_0)$  and  $t_y(z_0)$  respectively. The factors  $S_{\dots}$  and  $R_{\dots}$  denote magnetic field integrals and  $dz$  denotes  $(z_e - z_0)$ . The  $B_z$  component of the ICAL magnetic field is zero and the field is in the  $xy$  direction:  $\vec{B} = B_x(x(z), y(z))\hat{x} + B_y(x(z), y(z))\hat{y}$ . The field integrals are defined as [18]:

$$S_{i_1 \dots i_k} = \int_{z_0}^{z_e} \int_{z_0}^{z_e} B_{i_1}(x(z_1), y(z_1)) \dots \int_{z_0}^{z_e} B_{i_k}(x(z_k), y(z_k)) dz_k \dots dz_1 dz \quad (59)$$

and

$$R_{i_1 \dots i_k} = \int_{z_0}^{z_e} B_{i_1}(x(z_1), y(z_1)) \dots \int_{z_0}^{z_e} B_{i_k}(x(z_k), y(z_k)) dz_k \dots dz_1 \quad (60)$$

where  $i_1, i_2, \dots$  etc denote  $x, y, xx$  etc. These integrals were evaluated along the approximate particle trajectory. If the step size within iron is made reasonably small, magnetic field may be assumed to be constant along the step  $dz$  and the calculation of the integrals becomes easier.

The field integrals  $S_{\dots}$  and  $R_{\dots}$  were evaluated assuming that  $B_i(x(z), y(z))$  vary very slowly along the track  $(x_{particle}(z), y_{particle}(z))$  and may be assumed to be constant when integrating with respect to  $z$ . This is true unless the particle is traveling almost

$S_x$	$S_y$	$S_{xx}$	$S_{xy}$	$S_{yx}$	$S_{yy}$
$\frac{1}{2}B_x dz^2$	$\frac{1}{2}B_y dz^2$	$\frac{1}{6}B_x^2 dz^3$	$\frac{1}{6}B_x B_y dz^3$	$\frac{1}{6}B_x B_y dz^3$	$\frac{1}{6}B_y^2 dz^3$
$R_x$	$R_y$	$R_{xx}$	$R_{xy}$	$R_{yx}$	$R_{yy}$
$B_x dz$	$B_y dz$	$\frac{1}{2}B_x^2 dz^2$	$\frac{1}{2}B_x B_y dz^2$	$\frac{1}{2}B_x B_y dz^2$	$\frac{1}{2}B_y^2 dz^2$

Table 6.: Magnetic Field Integrals

parallel to the detector plane ( $\theta \approx 90^\circ$ ). The field integrals are given in Table 6. The effect of fringe field just outside the iron layer has been neglected in this work.

We also included the transverse variation of the field as in [87] (first addendum). This is because an error in the position  $(x, y)$  leads to an error in the magnetic field. For example, error in  $B_x$  is:

$$\delta B_x \approx \frac{\partial B_x}{\partial x} \delta x + \frac{\partial B_x}{\partial y} \delta y \quad (61)$$

The same is true for  $B_y$  as well. This error in magnetic field gives an additional error of the direction of the track. As a result, there is an error  $\delta R_x$  in the integral  $R_x$ :

$$\begin{aligned} \delta R_x &= \int \delta B_x(x(z), y(z)) dz \\ &\approx \left[ \frac{\partial B_x}{\partial x} dz \right] \delta x + \left[ \frac{\partial B_x}{\partial y} dz \right] \delta y \end{aligned} \quad (62)$$

Hence, from Eq.(57), the error of  $t_x(z_e)$  (to the first order in  $h$ ) is given as:

$$\begin{aligned} \delta t_x(z_e) &= h \left[ t_x t_y \frac{\partial B_x}{\partial x} - (1 + t_x^2) \frac{\partial B_y}{\partial x} \right] dz \delta x \\ &+ h \left[ t_x t_y \frac{\partial B_x}{\partial y} - (1 + t_x^2) \frac{\partial B_y}{\partial y} \right] dz \delta y \\ &+ \left[ 1 + h \left( t_y \left( 1 + \frac{t_x^2}{T^2} \right) R_x - t_x \left( 2 + \frac{1 + t_x^2}{T^2} \right) R_y \right) \right] \delta t_x \\ &+ h \left[ t_x \left( 1 + \frac{t_x^2}{T^2} \right) R_x - t_y \left( \frac{1 + t_x^2}{T^2} \right) R_y \right] \delta t_y \\ &+ kT [t_x t_y R_x - (1 + t_x^2) R_y] \delta \left( \frac{q}{p} \right) \end{aligned} \quad (63)$$

where  $T = \sqrt{1 + t_x^2 + t_y^2}$ . Similarly, smooth deterministic errors in other parameters can also be evaluated. Then, it becomes a trivial task to obtain the first four rows of the propagator matrix Eq.(52). For instance, the term  $\frac{\delta[t_x(z_e)]}{\delta(\frac{q}{p}(z_0))}$  is equal to  $kT [t_x t_y R_x - (1 + t_x^2) R_y]$  (from Eq.(63)). Terms of the order of  $h^2$  were calculated using Mathematica [88].

### 7.3.3 Signed inverse momentum

In general, the rate of energy loss of high energy muon in a material is given by [89]:

$$\left\langle -\frac{dE}{ds} \right\rangle = a(E) + b(E)E \quad (64)$$

where  $E$  is the total energy,  $a(E)$  gives the energy loss due to ionization and  $b(E)$  denotes the energy loss due to the radiative processes-bremsstrahlung, pair production and photo-nuclear interactions. In fact,  $a(E)$  and  $b(E)$  vary slowly with increasing energy  $E$ . However, in the energy range of interest in ICAL, muon and other particles lose energy mainly through ionization. Hence, the second term in Eq.(64) is not necessary and the energy loss is given by the Bethe-Bloch energy loss formula [12].

$$\left\langle -\frac{dE}{ds} \right\rangle = Kz^2 \frac{Z}{A} \frac{1}{\beta^2} \left[ \frac{1}{2} \ln \frac{2m_e c^2 \beta^2 \gamma^2 T_{max}}{I^2} - \beta^2 - \frac{\delta(\beta\gamma)}{2} \right] \quad (65)$$

Different parameters in the RHS of Eq. (65) is explained in the following table 7:

<u>Symbol</u>	<u>Meaning</u>	<u>Units/Values</u>
$m_e c^2$	electron mass $\times c^2$	0.511 MeV
$r_e$	Classical electron radius $\frac{e^2}{4\pi\epsilon_0 m_e c^2}$	2.817 fm
$N_A$	Avogadro's number	$6.022 \times 10^{23} \text{ mol}^{-1}$
$Z$	Atomic number of the medium	-
$A$	Atomic mass of the medium	-
$K/A$	$4\pi N_A r_e^2 m_e c^2$	$0.307075 \text{ MeVg}^{-1} \text{cm}^2$ (for $A = 1 \text{g/mol}^{-1}$ )
$I$	Mean excitation energy	MeV
$\delta$	Density effect correction	MeV
$m$	Projectile mass	MeV
$T_{max}$	Maximum KE imparted to an electron in a single collision $T_{max} = \frac{2m_e \beta^2 \gamma^2}{1 + 2\gamma \frac{m_e}{m} + (\frac{m_e}{m})^2}$	MeV

Table 7.: Explanation of terms in Bethe Bloch formula

For muon track fitting, the prediction of the signed inverse momentum element,  $(q/P)$ , has been performed with Bethe-Bloch energy loss formula, for every material with density  $> 1.5 \text{ g/cc}$ . The corresponding error propagation has been done using techniques shown in EMC internal reports [20] (second addendum). However, the tracks have been assumed orthogonal to the detector planes there. This is not true in INO-ICAL detector which would observe the atmospheric neutrinos coming from all directions. So, the error propagation of  $q/P$  is done more rigorously.

We want to find out the error  $\delta(q/P)$  at a point  $(x(z+dz), y(z+dz), (z+dz))$  of the track in terms of the error  $\delta(q/P)$  at  $(x(z), y(z), z)$ . We can write:

$$\delta(q/P)_{\mathbf{r}(z+dz)} = \delta(q/P)_{\mathbf{r}(z)} + \delta[d(q/P)] \quad (66)$$

The first term in Eq.(66) refers to the error in the estimate of  $(q/P)$ , which was already there from  $((x(z), y(z), z))$ . The second term denotes the average systematic error that creeps in due to the incorrect estimation of  $q/P$  at  $(x(z+dz), y(z+dz), (z+dz))$  from that at  $((x(z), y(z), z))$ . It is possible to expand  $d(q/P)$  as:

$$\begin{aligned} d(q/P) &= (q/P)_{\mathbf{r}(z+dz)} - (q/P)_{\mathbf{r}(z)} \\ &= f(\mathbf{r}(z+dz)) - f(\mathbf{r}(z)) \end{aligned} \quad (67)$$

where  $f(\mathbf{r}) = q/P(\mathbf{r})$  (which is known as the range-momentum relation). Muon CSDA (Continuous Slowing Down Approximation) range in *iron* as function of muon momenta  $P$  is known in the form of a numerical table [90]. We evaluate  $d(q/P)$  in the track frame such that no cross term arises in the following expansion:

$$d(q/P) = f'(l)dl + \frac{1}{2}f''(l)dl^2 + \frac{1}{6}f'''(l)dl^3 + \dots O(4) \quad (68)$$

where the arc length along the track is denoted by  $l$ . In this equation, it is assumed that the higher order correction terms are negligibly small. This approximation does not hold good if the particle track is at a large zenith angle  $\theta > 60^\circ$ . In such cases, the derivatives of  $f(l)$  are small, of course; however, the factors containing  $dl$  and its exponents grow rapidly as  $|dl| \approx \frac{dz}{\cos\theta}$ . The error in  $d(q/P)$  can be given by (from Eq.(68)):

$$\begin{aligned} \delta[d(q/P)] &= \delta\{f'(l)dl\} + \delta\left\{\frac{1}{2}f''(l)dl^2\right\} + \dots \\ &= f''(l)\delta l dl + f'(l)\delta(dl) + \frac{1}{2}f'''(l)\delta l dl^2 + f''(l)dl\delta(dl) \\ &= \left\{f''(l)dl + \frac{1}{2}f'''(l)dl^2\right\}\delta l + [f'(l) + f''(l)dl]\delta(dl) \end{aligned} \quad (69)$$

One must find  $\delta l$  and  $\delta(dl)$  correctly to obtain the error  $\delta(q/P)_{\mathbf{r}(z+dz)}$  as a function of  $\delta(q/P)_{\mathbf{r}(z)}$  and others. The factor  $\delta l$  may be found from:

$$\begin{aligned} \delta(q/P)_l &= \delta f(l) \\ &= f'(l)\delta l \end{aligned} \quad (70)$$

Thus, we have:

$$\delta l = \frac{\delta(q/P)_l}{f'(l)} \quad (71)$$

The other term  $\delta(dl)$  cannot be taken directly from EMC report 80/15 as that calculation was done in SC frame  $(x_\perp, y_\perp, z_\perp)$  [21, 87] and we are working in a Cartesian reference frame. In Appendix, we show that the following holds in a Cartesian coordinate system [Eq.(101)]:

$$\begin{bmatrix} \delta x \\ \delta y \\ \delta z \end{bmatrix}_{\mathbf{r}(z+dz)} = \begin{bmatrix} 1 & d\phi & -\cos\phi d\theta \\ -d\phi & 1 & -\sin\phi d\theta \\ \cos\phi d\theta & \sin\phi d\theta & 1 \end{bmatrix} \begin{bmatrix} \delta x \\ \delta y \\ \delta z \end{bmatrix}_{\mathbf{r}(z)} + \begin{bmatrix} \delta(dx) \\ \delta(dy) \\ \delta(dz) \end{bmatrix} \quad (72)$$

in a Cartesian frame, where  $\theta$  and  $\phi$  are the zenith and azimuthal angles respectively. For ICAL experiment  $\delta z_z = \delta z_{z+dz} = 0$ , as the detector planes correspond to fixed  $z$  coordinates. Thus, from Eq.(72),  $\delta(dz) = -\cos\phi d\theta (\delta x)_z - \sin\phi d\theta (\delta y)_z$ . Then,  $\delta(dl)$  may be expressed as:

$$\begin{aligned} \delta(dl) &= \delta\left(dz\sqrt{1+t_x^2+t_y^2}\right) \\ &= T\delta(dz) + dz\left(\frac{t_x}{T}(\delta t_x)_z + \frac{t_y}{T}(\delta t_y)_z\right) \\ &= T[-\cos\phi d\theta (\delta x)_z - \sin\phi d\theta (\delta y)_z] + dz\left(\frac{t_x}{T}(\delta t_x)_z + \frac{t_y}{T}(\delta t_y)_z\right) \\ &= \kappa\frac{q}{P} dl[B_x (\delta x)_z + B_y (\delta y)_z] + dz\left(\frac{t_x}{T}(\delta t_x)_z + \frac{t_y}{T}(\delta t_y)_z\right) \quad (73) \end{aligned}$$

where the last equality follows from Eq.(100). Hence, from Eq.(69) and Eq.(71), we can express  $\delta[d(q/P)]$  in terms of  $\delta(dl)$  as:

$$\begin{aligned} \delta[d(q/P)] &= \left\{ \frac{f''(l)}{f'(l)} dl + \frac{1}{2} \frac{f'''(l)}{f'(l)} dl^2 \right\} \delta\left(\frac{q}{P}\right)_l \\ &\quad + [f'(l) + f''(l) dl] \delta(dl) \quad (74) \end{aligned}$$

Hence, the error propagation for  $q/P$  may be given as the following:

$$\begin{aligned} \delta(q/P)_{l+dl} &= \left[ 1 + \left\{ \frac{f''(l)}{f'(l)} dl + \frac{1}{2} \frac{f'''(l)}{f'(l)} dl^2 \right\} \right] \delta(q/P)_l \\ &\quad + \kappa(f' + f'' dl) f(l) T dl [-B_y (\delta x)_l + B_x (\delta y)_l] \\ &\quad + (f' + f'' dl) dz \left( \frac{t_x}{T} (\delta t_x)_l + \frac{t_y}{T} (\delta t_y)_l \right) \quad (75) \end{aligned}$$

For proper convergence of  $q/p$  element, accurate calculation of the term  $\frac{\partial(q/p)_{l+dl}}{\partial(q/p)_l}$  is very important. This term is calculated from Eq. (75) in the following way:  $\frac{\partial(q/p)_{l+dl}}{\partial(q/p)_l} = \frac{\delta(q/p)_{l+dl}}{\delta(q/p)_l}$ . Clearly, this requires calculations of  $f', f'', f'''$  etc. where the derivatives are calculated with respect to  $l$ . This requires range-momentum tables for all materials (used in ICAL) that have density  $> 1.5 \text{ g/cm}^3$ . These tables [19] were calculated from the PDG tables of energy loss for different materials (like iron [91]). First, the range  $R$  corresponding to a tracking momentum  $P$  is obtained for a given material using a ROOT based cubic spline interpolation routine. Hence, the value of the derivatives  $f', f''$  etc. are calculated thereat. The convergence of  $(q/p)$  to the desired values is very sensitive to the calculation of  $\frac{\partial(q/p)_{l+dl}}{\partial(q/p)_l}$  term. Hence, central difference formula of fourth order Richardson extrapolation method [92] has been used to calculate these derivatives.

### 7.3.4 Random error contribution

So far we have discussed the average deterministic error terms. However, as indicated in Eq.(44), we must also account for the random errors due to multiple scattering and energy loss straggling.

#### 7.3.4.1 Multiple scattering

The multiple scattering matrix accounts for the random variation of the track elements  $(x, y, t_x, t_y)$  over the average motion controlled by the magnetic field. In ICAL, the charged particles traverse through a series of dense thick materials (like glass, iron etc.) along their trajectories. For example, the thickness of the glass plate is (3 mm) and that of the iron plate is (5.6 cm). Thus, the particle is not only deflected to *some other* random direction, but is also driven away from the point of its expected arrival. By the time it comes out of the thick dense material, its direction and position is shifted as shown in the following figure 7.3. Although the exact deviation of the track at a given point

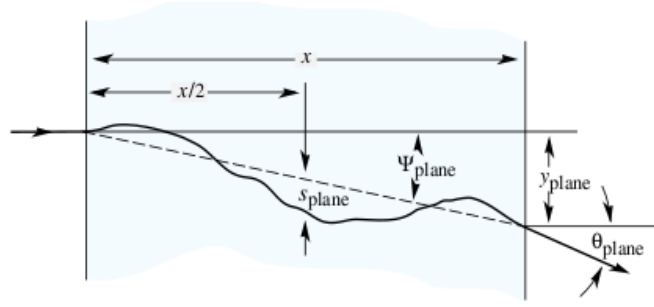


Figure 7.3.: effect of multiple scattering on a track

cannot be determined, it is possible to have a reasonable estimate of the variance of the deflection angle, caused by the scattering. A common practice in HEP track fitting is to use the Highland-Lynch- Dahl variance formula [93]. This formula gives the variance of the deflection angle due to scattering from a thin plane. Since the particle crosses through a finite thickness of the detector, the cumulative effect needs to be considered. The scattering contributes *random* errors to each of  $(x, y, t_x,$  and  $t_y$  at the end of a small tracking step within the thick material. The corresponding  $(4 \times 4)$  block of the full  $(5 \times 5)$  random error matrix is given as [94]:

$$Q_{(4 \times 4)}(l) = \begin{bmatrix} c(t_x, t_x) \frac{l^3}{3} & c(t_x, t_y) \frac{l^3}{3} & c(t_x, t_x) \frac{l^2}{2} D & c(t_x, t_y) \frac{l^2}{2} D \\ c(t_y, t_x) \frac{l^3}{3} & c(t_y, t_y) \frac{l^3}{3} & c(t_x, t_y) \frac{l^2}{2} D & c(t_y, t_y) \frac{l^2}{2} D \\ c(t_x, t_x) \frac{l^2}{2} D & c(t_x, t_y) \frac{l^2}{2} D & c(t_x, t_x) l & c(t_x, t_y) l \\ c(t_x, t_y) \frac{l^2}{2} D & c(t_y, t_y) \frac{l^2}{2} D & c(t_y, t_x) l & c(t_y, t_y) l \end{bmatrix} \quad (76)$$

where  $c(\alpha, \beta)$  represents the covariance between the elements  $\alpha$  and  $\beta$  and  $l$  denotes length of a small tracking step  $dz \sqrt{1 + t_x^2 + t_y^2}$ .  $D = +1(-1)$  depending on whether tracking is done in +ve(-ve)  $z$  direction. The elements  $c(t_x, t_x)$ ,  $c(t_x, t_y) \equiv c(t_y, t_x)$  and  $c(t_y, t_y)$  are given by [23], [94]:

$$\text{cov}(t_x, t_x) = (1 + t_x^2)(1 + t_x^2 + t_y^2)C_{MS} \quad (77)$$

$$\text{cov}(t_y, t_y) = (1 + t_y^2)(1 + t_x^2 + t_y^2)C_{MS} \quad (78)$$

$$\text{cov}(t_x, t_y) = t_x t_y (1 + t_x^2 + t_y^2)C_{MS} \quad (79)$$

where  $C_{MS}$  denote the Highland-Lynch-Dahl variance formula [93], [95], calculated based on Moliere's theory of multiple scattering. It is given by:

$$C_{MS} = \left(\frac{0.0136}{\beta p}\right)^2 \left(\frac{l}{l_{rad}}\right) \left[1 + 0.038 \ln\left(\frac{l}{l_{rad}}\right)\right] \quad (80)$$

where  $l$  is the step length and  $l_{rad}$  is the radiation length of the corresponding material.

However, the presence of logarithmic term in the variance formula (80) makes the calculation dependent on the chosen step length which is undesirable [21]. Hence, the variance estimated by Frühwirth et al. [24]:

$$C_{MS} = \frac{(0.015)^2}{\beta^2 p^2} \left(\frac{l}{l_s}\right) \quad (81)$$

where  $l_s$  is related to the radiation length of the material through the following relation:

$$l_s = l_{rad} \frac{Z+1}{Z} \frac{289Z^{-1/2}}{159Z^{-1/3}} \quad (82)$$

is independent of the issue and has been implemented in ICAL track fitting. The dependence shown in Eq. (82) is use to calculate the multiple scattering from dense components of RPC like glass, copper and aluminum etc.

#### 7.3.4.2 Energy loss straggling

The energy loss of the particle inside matter is not a continuous process. When a particle is made to traverse a finite depth  $d$  of dense material, the energy loss in every  $\delta x = d/N$  (where  $N$  is a large integer) length of material is not fully governed by the Bethe Bloch formula [12]. Instead, *the rate of energy loss* follows a Landau/Vavilov distribution [96]. Nevertheless, Bethe Bloch formula provides a reasonable estimate of the average energy loss. Therefore, it is fine to use the range-momentum tables (prepared assuming the validity of Continuous Slowing Down Approximation of the particle due to continuous loss of energy) to perform the prediction step 7.2.2. However, the random fluctuations of the energy loss (known as energy loss straggling) must be taken into account while propagating corresponding errors. This is done by using the covariance terms:  $Q[t, q/P]$ , where  $t \in (x, y, t_x, t_y, q/P)$  in the full random noise matrix:

$$\begin{bmatrix} Q_{x,x} & Q_{x,y} & Q_{x,t_x} & Q_{x,t_y} & Q_{x,q/p} \\ Q_{x,y} & Q_{y,y} & Q_{y,t_x} & Q_{y,t_y} & Q_{y,q/p} \\ Q_{x,t_x} & Q_{y,t_x} & Q_{t_x,t_x} & Q_{t_x,t_y} & Q_{t_x,q/p} \\ Q_{x,t_y} & Q_{y,t_y} & Q_{t_x,t_y} & Q_{t_y,t_y} & Q_{t_y,q/p} \\ \hline Q_{x,q/p} & Q_{y,q/p} & Q_{t_x,q/p} & Q_{t_y,q/p} & Q_{q/p,q/p} \end{bmatrix}$$

The first  $4 \times 4$  block in this matrix corresponds to Eq. (76). The term  $Q_{q/P, q/P}$  is related to the variance  $\sigma^2(E)$  of the truncated Landau distribution through [21]:

$$\begin{aligned} Q_{q/P, q/P} &= \frac{1}{P^4} \sigma^2(P) \\ &= \frac{E^2}{P^6} \sigma^2(E) \end{aligned} \quad (83)$$

The nature of fluctuations of the energy loss of a particle of charge  $z$ , mass  $m$  and velocity  $\beta c$  are given by the parameter  $k = \frac{\xi}{T_{max}}$  where  $\xi$  denotes the mean energy loss:

$$\xi = 0.1534 \frac{z^2 Z}{\beta^2 A} \rho d \quad \text{MeV} \quad (84)$$

here  $\rho, d, Z$  and  $A$  stand for density ( $\text{g}/\text{cm}^3$ ), thickness, atomic and mass number of the medium.  $T_{max}$  has been defined in table 7. It is seen that the value of  $k$  decides the shape of the straggling function. If  $k > 10$ , the distribution is Gaussian, with  $\sigma(E)$  given by:

$$\sigma^2(E) = \xi T_{max} \left( 1 - \frac{\beta^2}{2} \right) \quad (85)$$

However, as  $k \rightarrow 0.01$  (starting from  $k = 10$ ), the distribution gradually changes from Gaussian to Vavilov and when  $k < 0.01$ , then one has to consider Landau distribution. For ICAL experiment, the value of  $k$  is found to be  $< 1.0$ , such that  $\sigma(E)$  needs to be extracted from Vavilov-Landau domain. The problem is non-trivial, as the mean and the variance of Landau distribution is infinity [21]. Therefore,  $\sigma(E)$  is usually calculated by truncating the Landau distribution at some point.

Finally, we have evaluated  $\sigma(E)$  from the Urban model [25] by sampling the number of collisions suffered by the particle from a Poisson's distribution (parametrized by the mean excitation potential of the material, the fraction  $\alpha$  corresponding to the area of the truncated Landau distribution, and other parameters of the model). The fraction  $\alpha$  is found to span rather wide range (0.993-0.999) if we wish to obtain unit standard deviation of the  $q/P$  pull distribution in wide  $P_\mu$ - $\theta_\mu$  range.

The other covariance terms like  $Q_{x, q/P} \equiv \text{cov}(x, q/P)$  is derived as below:

$$\begin{aligned} \text{cov}[x, q/P] &\equiv \text{cov}[q/P, x] \\ &= \frac{\partial x(P)}{\partial P} \frac{\partial}{\partial P} \left[ \frac{q}{P} \right] \sigma^2(P) \\ &= -\frac{q}{P^2} \frac{\partial x(P)}{\partial P} \sigma^2(P), \end{aligned} \quad (86)$$

where  $x = x(P)$  is known from Eq.(55). Other cross terms were also evaluated this way using Eq.(56)-(58).

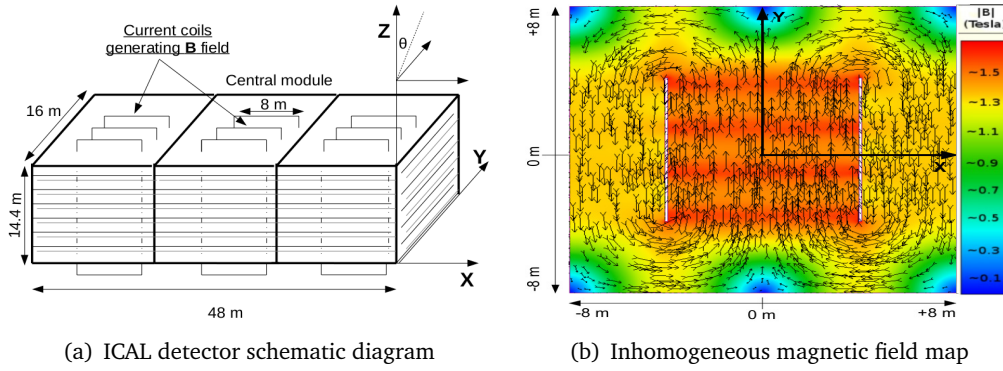
#### 7.4 TRACK FITTING RESULTS

The method described in the previous section has been implemented in the reconstruction program of INO-ICAL. The main purpose is to obtain optimal reconstruction of muons coming from (CC)  $\nu_\mu$  events generated by [69]. The performance of the reconstruction code will be described in this section. First, we shall take the trivial case that there is no

hadrons in the event. This will validate the Kalman filter only, because in this case the job of the track finder program is rather easy-it has nothing to separate the muon track from. We shall see both qualitative and quantitative aspects of this single muon reconstruction performance and explain some of the observations. Then, the more realistic case of muons coming of neutrino events will be dealt with. We shall show the performances of reconstruction of NUANCE generated atmospheric neutrino event reconstruction. This will be followed by a small discussion on the hadron energy calibration.

#### 7.4.1 Single muon results

##### 7.4.1.1 Goodness of fits



In this subsection, we show the quality of reconstruction of GEANT4 [68] generated single muon events whose vertices are confined within the ICAL detector (a schematic diagram of the detector is shown in figure 7.4(a)). The current coils shown in this figure generate inhomogeneous magnetic field 7.4(b) inside the iron slabs that act as the passive detector element of the calorimeter. The reconstruction program attempts to find the momenta of the muon tracks that are deflected by this magnetic field. To this end, 5000 Monte Carlo  $\mu^\pm$  tracks of generator level momenta  $p_\mu^{Gen} \in [1 - 10]$  GeV/c were simulated through the virtual detector at zenith angles  $\cos \theta_\mu^{Gen} = [0.95, 0.75, 0.55]$ . Their event vertices were smeared over a volume of (43 m  $\times$  14.4 m  $\times$  10m) around the center of the detector. This smearing includes a portion with inhomogeneous magnetic field 7.4(b) in the y direction.

The quality of the fit is expressed by the pull distributions and the reduced  $\chi^2$  distribution. The pull of a fitted parameter  $x$  is defined as:

$$P(x) = \frac{x_{reconstructed} - x_{simulated}}{\sqrt{C_{xx}}} \quad (87)$$

where  $\sqrt{C_{xx}}$  represents the filtered error at a point where the pull is calculated and is calculated from the diagonal elements of the final fitted estimation error covariance matrix. In ICAL, we are mostly interested in the reconstruction parameters near the event vertex; hence, the pull is evaluated there only. For good fit, the pull distributions should have mean at zero and standard deviation equal to unity. On the other hand, the  $\chi^2$  of a fitted track is calculated over all measurement sites ( $k$ ) and is given by:

$$\chi_p^2 = \sum_k (\mathbf{r}_k^{k-1})^T (R_k^{k-1})^{-1} (\mathbf{r}_k^{k-1}) \quad (88)$$

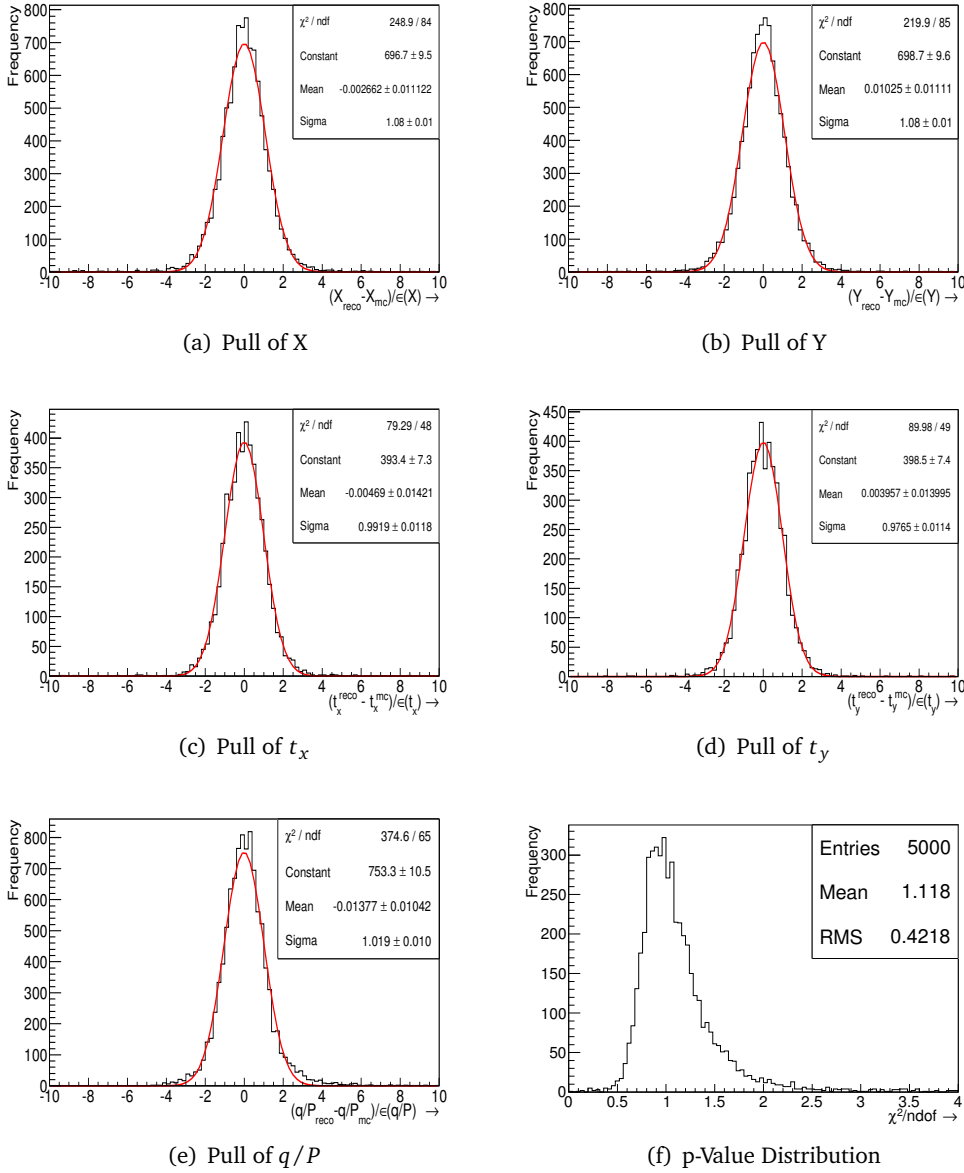


Figure 7.4.: Reconstructed muon of momentum 6 GeV/c at zenith angle  $18.2^\circ$  ( $\cos\theta=0.95$ ). Pull Distributions: (a) X, (b) Y, (c)  $t_x$ , (d)  $t_y$ , (e)  $\frac{q}{P}$  and (f)  $\chi^2/\text{ndof}$  distribution

where  $\mathbf{r}_k^{k-1}$  denotes the residual of the model prediction ( $\mathbf{r}_k^{k-1} = \mathbf{m}_k - H_k \mathbf{x}_k^{k-1}$ ) and  $R_k^{k-1}$  denotes the covariance matrix of the predicted residuals and is given by  $R_k^{k-1} = V_k + H_k C_k^{k-1} H_k^T$ . It is interesting to note that  $\chi_p^2$  is exactly equal to the  $\chi_f^2$  of the fits [85]. The  $\chi^2$  of the fit is calculated incrementally at every measurement site while doing the forward filtering. Then, the reduced  $\chi^2$  is obtained by dividing the total  $\chi^2$  so found by the no. free parameters. In this case, the no. free parameters is  $2N - 5$ , where  $N$  denotes the total no. of measurement sites. Each measurement site contributes two degrees of freedom; so, for  $N$  measurements,  $2N$  degrees of freedom exist. However, these are constrained by 5 equations used to initialize the filter. Hence, the no. of free parameters is  $2N - 5$ . Then, reduced  $\chi^2$  distribution is the distribution of  $\chi^2 / (2N - 5)$  for all events.

For good fits, the mean of this distribution is equal to unity. In figure 7.4, we show the pull distributions and the reduced  $\chi^2$  distribution for 5000 muons of  $P_\mu^{Gen} = 6$  GeV/c at  $\cos \theta_\mu^{Gen} = 0.95$ .

In figure 7.4 we show these distributions for  $\mu^-$  tracks of momentum 6 GeV/c at zenith angle  $\cos \theta = 0.95$ . The error of an element  $x$  has been represented by  $\epsilon(x)$  in these figures. Evidently, the means of the pull distributions are close to zero and their standard deviations are close to one. Similar performance is seen for a wide variation of input momenta and zenith angles.

However, since all the tracks do *not* have the same no. of measurements, the contributions of individual events to the reduced  $\chi^2$  plot 7.4(f) cannot be treated in the same footing. The following figure 7.5(a) shows the distribution of the no. of measurements (or, hits) along these 6 GeV/c muon tracks shot at  $\cos \theta_\mu = 0.95$ . Whereas 60–70 hits are expected from these muons (assuming Bethe Bloch energy loss), many of them give rather small no. of hits. Events with such low no. of measurements are: (a) affected by energy loss fluctuations, (b) partially contained events and (c) lost in the inactive space of RPCs. A still better way to gauge the performance of track fitting is to observe the deviation

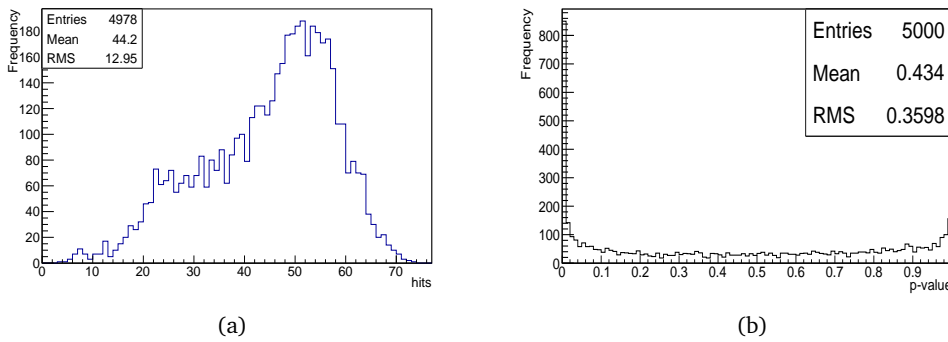


Figure 7.5.: (a) Distribution of hits, (b) p-value distribution @  $P_\mu = 6$  GeV/c at  $\cos \theta_\mu = 0.95$

of  $p$ -value. The  $p$ -value distribution of total  $\chi^2$  [histogram of TMath::Prob( $\chi^2$ ,ndof)] should be reasonably flat in the range  $[0.0 - 1.0]$ . This happens when the shape of the total  $\chi^2$  distribution approaches a true  $\chi^2$  probability distribution function. For this to happen, the prediction model should be good enough, the measurement errors should be Gaussian distributed and the measurements should be independent of each other. The  $p$ -value distribution for the same set of events is shown in figure 7.5(b). The distribution is seen to be more or less flat within the range  $[0.1 - 0.8]$ . However, the whole distribution between  $[0.0 - 1.0]$  is not uniform as: (a) the prediction model is not indefinitely accurate, (b) the measurements are not Gaussian and (c) are correlated. The peak at  $p \rightarrow 0^+$  comes from the events lying near the tail of the fitted reduced chi square distribution (see figure 7.6(a)) and the small heap at  $p \rightarrow 1^-$  comes from those events for which the measurements are correlated. This correlation creep in through the covariance matrix of predicted residuals  $R = HCH^T$  (where it is understood that the estimation error covariance is implicitly dependent on the random noise). Larger correlation leads to larger elements  $C_{ij}$  which in turn leads to larger  $R$ , thereby reducing the  $\chi^2$  (from the definition of  $\chi^2$  (Eq. (88))). Indeed we have seen that the heap becomes much smaller muon tracks with higher momenta  $[\geq 10$  GeV/c] for which the effect of

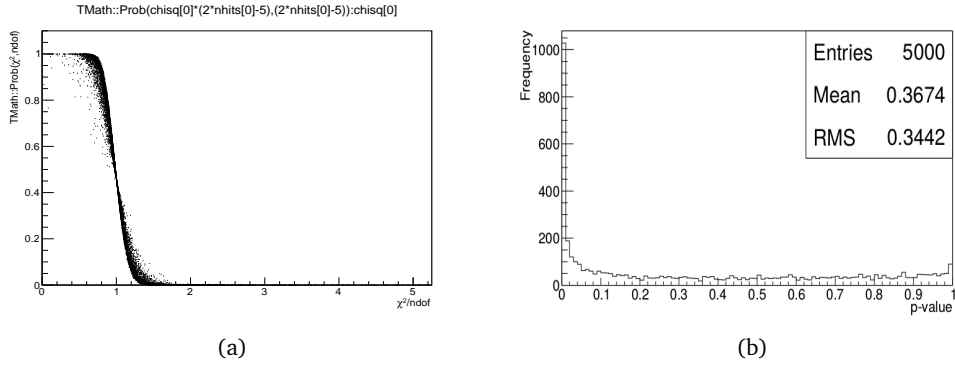


Figure 7.6.: (a) p-value vs  $\chi^2/\text{ndof}$  plot, (b) p-value distribution @  $P_\mu = 10$  GeV/c at  $\cos \theta_\mu = 0.95$

multiple scattering is less dominant. This is shown in figure 7.6(b). The heap increases in size at lower momenta  $P_\mu^{Gen} < 2 - 3$  GeV/c and higher zenith angle, represented by  $\cos \theta_\mu^{gen} < 0.65$ .

#### 7.4.1.2 Pull parameters at wide range of $P_\mu^{Gen} - \cos \theta_\mu^{Gen}$

Here we show the variations of the means and the widths of the  $q/P$  Pull distributions for various input  $P_\mu$  and  $\cos \theta_\mu$  values (figure 7.7(a), 7.7(b)). The continuous lines denote data for  $\mu^-$  and the dotted line denotes data for  $\mu^+$ . From figures 7.7(a) and 7.7(b), we

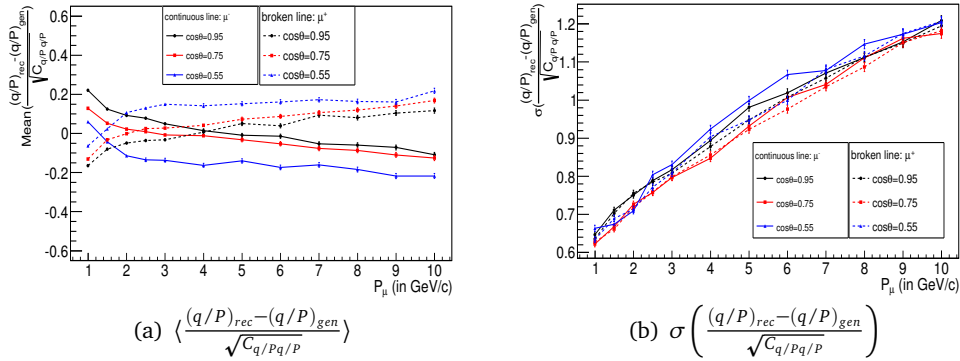


Figure 7.7.: Variation of Mean and Sigma of  $q/P$  Pull Distribution

see that the Kalman filter convergence of  $q/P$  element is more or less comparable for  $\mu^-$  and  $\mu^+$ . The mean shift for them is symmetric about zero. In fact, as the zenith angle  $\theta_\mu$  is increased, the accuracy of the  $q/P$  convergence worsens gradually. This behavior of the pull parameters is reasonable; because the track fitting performance should gradually worsen at lower  $P_\mu^{Gen}$  and higher zenith angle (represented by lower  $|\cos \theta_\mu^{Gen}|$ ), because of less no. of available measurements and dominant multiple scattering (since the particle has to traverse larger path length inside the material). This is also consistent with the observation made about the  $\chi^2$  probability ( $p$ -value) distribution.

#### 7.4.2 Performance from quantitative aspects

So far, we have seen the qualitative features of the reconstructed events. Let us now pay attention to aspects which more directly influences the neutrino oscillation analysis. The oscillation probability is dependent on  $\frac{L_\nu}{E_\nu}$  where  $L_\nu$  denotes the distance traversed inside the earth matter and  $E_\nu$  ( $\approx P_\nu$ ) is the neutrino energy (momentum). Now, the distance  $L_\nu$  depends on  $\cos \theta_\nu$ ; and the direction of the neutrino is highly correlated to the direction of the muon, as seen in figure 7.8(a). Hence, the accuracy and the precision of estimation of the reconstruction program is of prime importance here. For GEANT4 generated

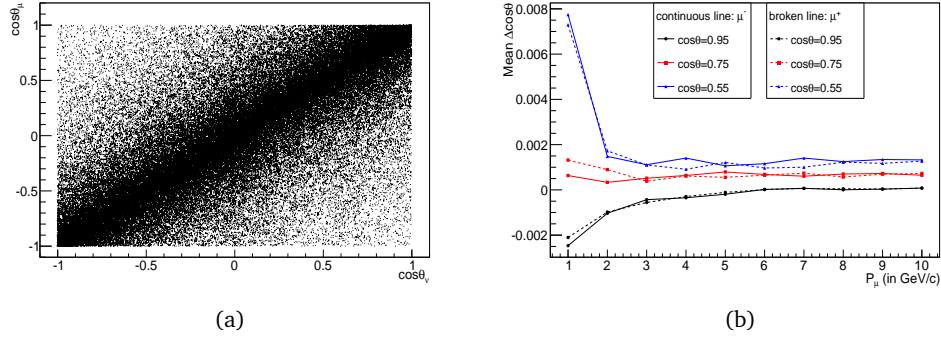


Figure 7.8.: (a) Correlation of the directions between incoming neutrino and outgoing muon (b) accuracy of reconstructed zenith angle for various  $P_\mu^{Gen}$ - $\cos \theta_\mu^{Gen}$  values

single muon Monte Carlo events, the accuracy of the angular estimation is shown in figure 7.8(b) for various input momenta and directions ( $P_\mu^{Gen} \in [1.0 - 10.0]$  GeV/c at  $\cos \theta_\mu^{Gen} = 0.95, 0.75$  and  $0.55$ ). The oscillation analysis is even more sensitive to the

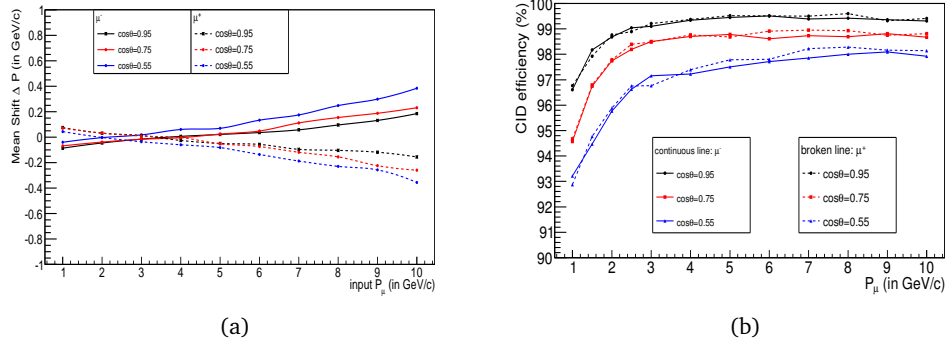


Figure 7.9.: (a) Mean shift in the reconstructed momentum distribution and (b) Charge identification efficiency in % for reconstructed events at various  $P_\mu$ - $\cos \theta_\mu$  values

accuracy of the momentum estimation. In the following figure 7.9(a), the deviation of the mean of the reconstructed momentum distribution from the generator level momentum value is shown, for  $\mu^-$  and  $\mu^+$  events with  $P_\mu^{Gen} \in [1.0 - 10.0]$  GeV/c at  $\cos \theta_\mu^{Gen} = 0.95, 0.75$  and  $0.55$ . The reconstruction shows gradual deterioration with

increasing zenith angle (decreasing  $|\cos \theta_\mu|$ ). The same behavior is seen in case of the charge identification efficiency, shown in figure 7.9(b). The % of correct charge identification increases with increasing generator level momenta for all angles, but it decreases for higher zenith angles for any given momentum. This can be explained by taking the effect of multiple Coulomb scattering into account. The tracks at lower momenta and higher zenith angles are affected more by the scattering (as seen in Eq. (80)). In such cases, the sagitta of the track due to magnetic field and that due to multiple scattering compete with each other. If the measurement is quite shifted with respect to the predicted position, the program cannot decide if the deviation is due to poor extrapolation or due to multiple scattering. Hence, poor momentum estimation with poor charge identification efficiency is observed. The problem is more harmful for two reasons: (i) one does not know *which* event has got its charge identified wrong and (ii) the flux of atmospheric neutrinos is higher at lower momenta and larger zenith angles only.

#### 7.4.3 Momentum and direction resolution

The precision of the estimations of momentum and direction are vital parameters, as far as the mass hierarchy sensitivity analysis is concerned. They depend upon *how well* the curvature of the tracks can be estimated and *how much* the tracks are affected by multiple scattering. The former is better estimated if the track length is longer, no. of measurements is greater and the spatial resolution is good (i.e. measurement error is less). Apart from this, the resolution of momentum also depends on the resolution of direction. The latter is given by the width of the  $\cos \theta_{rec}$  distribution. The momentum resolution is defined as:

$$\frac{\sigma(P)}{P} = \frac{\text{fitted width of the } P_{reco} \text{ distribution}}{P_{\mu}^{Gen}} \quad (89)$$

In the context of ICAL experiment, the momentum  $p(\mathbf{r})$  of the charged particle at  $\mathbf{r}$  is given by  $p(\mathbf{r}) = \kappa q |\hat{T} \times \mathbf{B}| R(\mathbf{r}) = \kappa q B \cos \theta R(\mathbf{r})$  where  $\hat{T}$  denotes an unit vector in the direction of motion and magnetic field  $\mathbf{B}$  is along the  $x - y$  direction (no  $z$  component). Clearly, the angle between  $\mathbf{B}$  and  $\hat{T}$  is complementary to the zenith angle  $\theta$ . If we assume that  $\mathbf{B}$  remains more or less constant around the track, then the momentum is a function of  $\theta$  and the radius of curvature  $R$ . From propagation of error formula, one can easily show that [97]

$$\begin{aligned} \left( \frac{\sigma(P)}{P} \right)^2 &= \frac{1}{R^2} \sigma^2(R) + \tan^2 \theta \sigma^2(\theta) \\ &= \left( \frac{\sigma(R)}{R} \right)^2 + \left( \frac{\sigma(\cos \theta)}{\cos \theta} \right)^2 \end{aligned} \quad (90)$$

The first term in Eq. (90) is dependent on the measurement of sagitta of the track and its associated error. In fact,  $\frac{\sigma(R)}{R} = \frac{\sigma(s)}{s}$ , where  $s$  denotes sagitta. The error in sagitta comes from the intrinsic spatial resolution (SR) of the detector  $\sigma_{xy}$  and from the multiple scattering (MS). Hence, the combined resolution is given by [97]:

$$\left( \frac{\sigma(P)}{P} \right) = \sqrt{\left( \frac{\sigma(P)}{P} \right)_{SR}^2 + \left( \frac{\sigma(P)}{P} \right)_{MS}^2 + \left( \frac{\sigma(\cos \theta)}{\cos \theta} \right)^2} \quad (91)$$

Since,  $|\cos \theta|$  becomes smaller as  $\theta$  becomes larger (say  $\theta \rightarrow 90^\circ$ ), the contribution of the last term becomes higher even if everything else remains the same. It is seen that the direction resolution (width of the  $\cos \theta_{rec}$  distribution) itself becomes poorer at higher  $\cos \theta^{Gen}$  values, as shown in figure 7.10(a). Hence, the relative contribution of  $\frac{\sigma(\cos \theta)}{\cos \theta}$

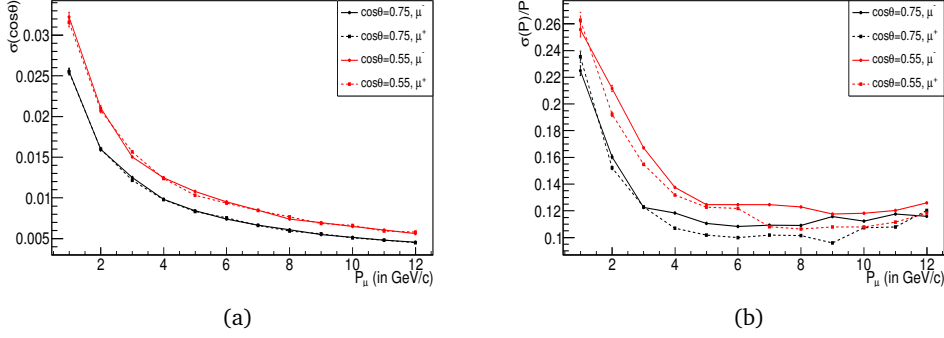


Figure 7.10.: Reconstructed (a) momentum resolution plot and (b)  $\cos \theta$  resolution plot

to the momentum resolution is higher for events at larger zenith angle.

The first term under the square root in the RHS of Eq. (91) is dependent on the spatial resolution of the detector. An crude estimate of this term is provided by Gluckstern's formula [98]:

$$\left(\frac{\sigma(P)}{P}\right)_{SR} = \frac{P}{0.3B} \frac{\sigma_{xy}}{L^2} \sqrt{\frac{720N^3}{(N-1)(N+1)(N+2)(N+3)}} \quad (92)$$

where  $\sigma_{xy}$  denotes the spatial measurement error,  $L$  stands for the total length of the track and the total no. of measurements is given by  $N + 1$ , from a track divided in  $N$  equal segments. Derivation of the formula is based on some assumptions like: track is perpendicular to the active detector plane, all the measurements are done at equal distances from each other etc. Although this formula is not applicable in ICAL (as the assumptions do not hold in most of the cases), still it provides a good approximation of  $\left(\frac{\sigma(P)}{P}\right)_{SR}$  and reveals some important features of track fitting:

(a) Higher  $N$  gives better momentum resolution from curvature method, compared to the case where less no. of measurements are available. If  $N$  is very high, the formula reduces to:

$$\left(\frac{\sigma(P)}{P}\right)_{SR} = \frac{P}{0.3B} \frac{\sigma_{xy}}{L^2} \sqrt{\frac{720}{N+5}} \quad (93)$$

(b) The same is true for a track with larger length  $L$ . In fact, the dependence is  $\propto \frac{1}{L^2}$ .

(c) The resolution improves with higher  $B$  and worsens with increasing  $p$  and spatial resolution  $\sigma_{xy}$ . In reality, the estimate is usually poorer as the (i) tracks are *not* perpendicular to the detector plane and (ii) measurements are not equidistant.

The second term under the square root in the RHS of Eq. (91),  $\left(\frac{\sigma(P)}{P}\right)_{MS}$ , represents the contribution of multiple scattering to the total momentum resolution. The sagitta due to multiple scattering is given by  $s_{MS}^{rms} = \frac{L}{4\sqrt{3}} \sqrt{C_{MS}}$  [96], where  $C_{MS}$  is given by Eq. (80). The contribution of multiple scattering term is found to be:

$$\left(\frac{\sigma(P)}{P}\right)_{MS} \approx \frac{0.05}{\beta B \sqrt{LL_{rad} \cos \theta}} \quad (94)$$

Clearly, at lower momenta, where  $\beta \ll 1$ , and at higher zenith angle, where  $\cos \theta \rightarrow 90^\circ$ , the total momentum resolution is dominated by the multiple scattering.

The content of the formula can be understood with some concrete example in the context of ICAL experiment. In ICAL simulation, the spatial resolution is  $\sigma_{xy} = 0.02/\sqrt{12}$  m. If a large no. of particles of  $P_\mu^{Gen} = 5$  GeV/c are shot at the direction  $\cos \theta_\mu^{Gen} = 0.75$  and if they generate  $\sim 31$  hits in the detector along average track length  $\sim 4.9$  m while passing through a region of uniform magnetic field of 1.25 T, then from Eq. (91), (92), (94) and figure 7.10(a), one finds  $\left(\frac{\sigma(P)}{P}\right)_{SR} \sim 1.45\%$ ,  $\left(\frac{\sigma(P)}{P}\right)_{MS} \sim 15.74\%$  and  $\frac{\sigma(\cos \theta)}{\cos \theta} \sim 1.33\%$ . Then, the combined momentum resolution is  $\frac{\sigma(P)}{P} \sim \sqrt{(1.45\%)^2 + (15.74\%)^2 + (1.33\%)^2} \sim 15.86\%$ . This estimate is of the order of the resolution data plotted in figure 7.10(b). However, the estimate in the figure is still better as the events actually passed through magnetic field of  $\sim 1.5 - 1.6$  T, Instead of 1.25 T. Also, when the  $P_{rec}$  distributions are fitted with Gaussian functions, the standard deviation of the fitted distributions are less compared to the original distribution.

We conclude this section by saying that the  $P_{rec}$  distributions, which were obtained by track fitting, are not ideal Gaussian distributions. Thus, when Gaussian functions are fitted to  $P_{rec}$  distributions to extract mean and sigma, usually the fit quality is not very good. The reason is that  $P_{rec}$  distribution is intrinsically not Gaussian [99] as it is not proportional to sagitta measurement.

#### 7.4.4 Improvements of the existing code

The existing reconstruction code had several issues related to track reconstruction. Among them, the most problematic was the issue of tracks being split while passing through the vertical stacks of the inactive spaces of RPCs. The Kalman filter was then applied to each of these smaller track-lets, inside the active region of the detector, to fit them individually. The result was that many single muon tracks were fitted with two or more sets of fit parameters. An example of this is shown in the following figure 7.11(a). The problem

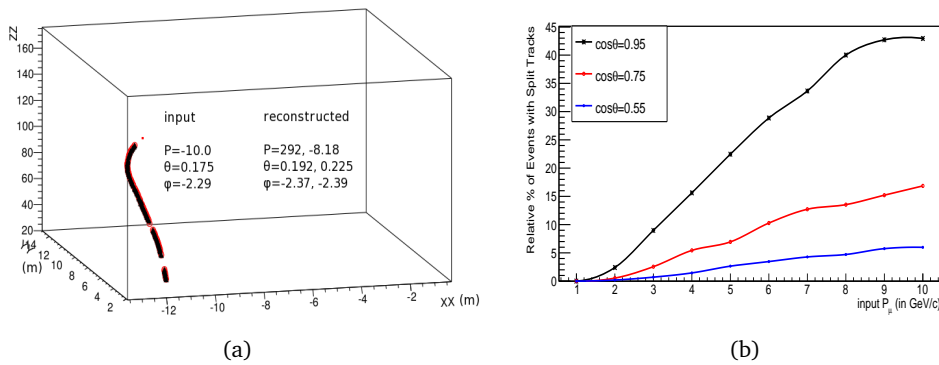


Figure 7.11.: (a) A track split near the border of two RPCs at  $x = 12$  m and (b) % of split events at different  $P_\mu^{Gen} - \cos \theta_\mu^{Gen}$

was seen to be frequent for higher energy events shot at higher  $\cos \theta$  values, as shown in 7.11(b). In most of these cases, the estimation of the track parameters were inaccurate, because of less no. of available measurements in each of these track-lets. For example, the  $P_\mu^{Gen} = 10$  GeV/c event, shown in figure 7.11(a), is reconstructed with two sets of fit

parameters which are not close to the generator level values. Events such as these led to long tails in the  $P_{rec}$  distribution which, in turn, led to worse momentum resolution.

The problem was initially rectified at track fitter level. After fitting the track-lets separately by the Kalman filter (developed in this thesis), the fitted state vectors were extrapolated through the inactive spaces of the detector using Eq. (55)- (58). If the extrapolated positions were found close enough to the measured cluster positions, then the two track-lets were joined. This approach, while quite straightforward, has a caveat in it. The charge estimation of a smaller track-let may be wrong, as it may not be possible for the program to estimate the correct sign of the curvature of an event from only a few measurements done along a small part of the event track. In this case, the extrapolation of  $\mathbf{x}$  may lead to a point quite far from the measured position. Such extrapolation is also no good in case the track momentum is small, as the Eq. (55)- (58) that contains the powers of  $q/P$ , start diverging. The extrapolation does not take into account multiple scattering as well.

Hence, a different approach was adopted. While developing the current track finder program the conditions were tuned such that when a triplet is separated from an existing segment by inactive spaces, the triplet is appended to the segment, if the direction of the triplet is close to the direction of the nearest part of the track segment. This has already been explained in case III (in figure 6.3(c) in the previous chapter). This approach is effective in atmospheric neutrino experiment like INO-ICAL, because the chance of misidentifying a track (from another event) to be a part of the current track of the current event is extremely small. Considering the fact that there will be only about 10-11 charged current events in a day in ICAL, the probability that two different events will fall in the same time window so that their tracks *seem* to be the part of a longer track is almost negligible. Anyway, the adopted solution is seen to reduce the tail in the reconstructed momentum distribution and hence, the resolution is improved. This is seen in the following figures 7.12(a) and 7.12(b). In fact, the efficiency of reconstruction,

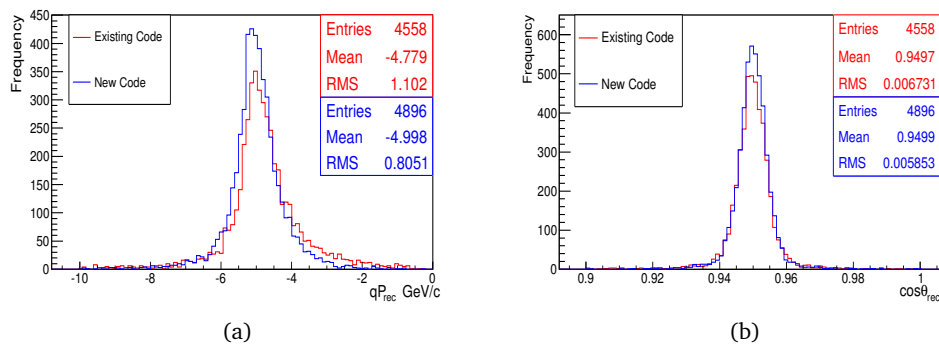


Figure 7.12.: Comparison of (a)  $P_{rec}$  (b)  $\cos \theta_{rec}$  distributions for  $P_{\mu}^{Gen} = 5 \text{ GeV}/c$  and  $\cos \theta_{\mu}^{Gen} = 0.95$

accuracy and precision of reconstruction of momentum and  $\cos \theta$  is also improved, as is seen from this plot.

Apart from the issue of the split tracks, the existing Kalman filter code implemented a simple propagator matrix [14] to carry out the error propagation (Eq. (44)) directly between the planes containing the measurements neglecting the intermediate variations

of magnetic field, tracking slopes and momenta. These simple treatments have been replaced with rigorous and computationally intensive calculations. In the existing Kalman filter the state extrapolation was done with the swimswimmer package, which had known issues at lower generator momenta [16]. However, the analytic formulae developed during the thesis work (Eq. (55)- (58)) has removed our dependency on swimswimmer package which was taken from MINOS experiment [14]. The performance of reconstruction is seen to improve at higher zenith angles as well, as is seen from the following table 8 where the comparison between the two codes is shown for  $P_\mu^{Gen} \in [1.0 - 10.0]$  GeV/c at  $\cos \theta_\mu^{Gen} = 0.75$ .

Code:-		Existing Code			Modified Code		
P(GeV/c)	$\cos\theta$	$rms(\theta_\mu)$	$rms(P_\mu)$	CID%	$rms(\theta_\mu)$	$rms(P_\mu)$	CID%
1.0	0.75	0.051	0.27	91.61	0.049	0.29	94.57
2.0	0.75	0.035	0.47	96.06	0.032	0.44	97.74
3.0	0.75	0.029	0.61	96.07	0.026	0.57	98.50
4.0	0.75	0.023	0.83	96.58	0.021	0.72	98.70
5.0	0.75	0.019	0.95	96.61	0.018	0.85	98.78
6.0	0.75	0.016	1.11	96.57	0.016	1.03	98.61
7.0	0.75	0.014	1.34	97.53	0.015	1.23	98.73
8.0	0.75	0.015	1.71	97.27	0.013	1.46	98.69
9.0	0.75	0.015	1.86	96.93	0.012	1.69	98.81
10.0	0.75	0.010	2.21	97.47	0.010	1.81	98.67

Table 8.: Comparison of the two codes at  $\cos \theta_\mu^{Gen} = 0.75$

#### 7.4.5 CPU Time

The time taken for the reconstruction of a muon track depends on the number of hits, as matrix inversions are performed at the site of every hit. Depending on the input  $P_\mu$  and  $\cos \theta_\mu$ , the number of hits vary widely. Tracks with same momentum in the vertical direction cross more number of layers than the tracks in horizontal direction. Similarly, tracks with higher input momenta cross more layers than those with lower input momenta. Typically, 1000 muon tracks of  $P_\mu^{Gen} = 5$  GeV/c at  $\cos \theta_\mu^{Gen} = 0.95$  are reconstructed in  $\sim 12$  minutes in a IC-i5 CPU.

#### 7.4.6 NUANCE event reconstruction performance

The track reconstruction program, developed during the thesis period, has been applied to reconstruct NUANCE level atmospheric neutrino events in the energy range  $E_\nu \in [0.5 - 100.0]$  GeV. The resulting final state particles comprise muons and other hadrons, depending on the type of the interaction. The muon momenta lie in a wide range  $P_\mu^{Gen} (0.0, 100.0)$  and they go in all directions between  $\cos \theta_\mu \in [-1, 1]$ . However, most muons have momenta  $\leq 2$  GeV/c, as seen from figure 6.5(a). Effectively a large no. of muons traverse a small no. of active RPC planes, because of lower momentum or larger zenith angle  $\cos \theta_\mu < 0.5$ . In a large fraction of cases, the no. of clusters in

the track is less than 5. These events could not be reconstructed (see the red dots in figure 7.13(a)). The black dots represent the reconstructed events in this figure. These

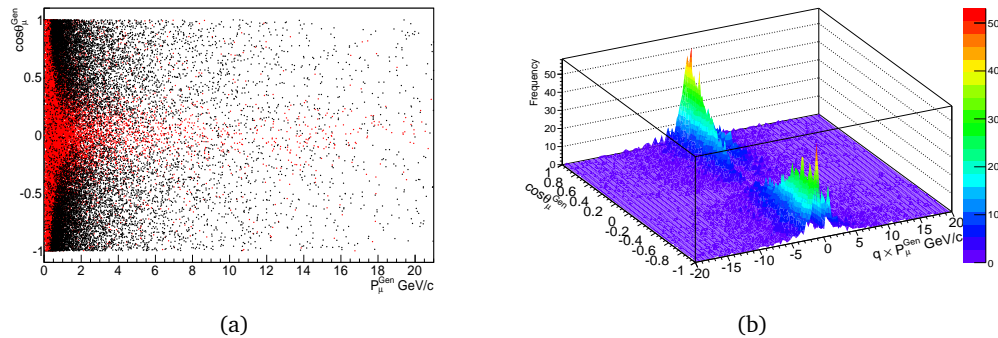


Figure 7.13.: (a)  $P_\mu^{Gen} - \cos \theta_\mu^{Gen}$  spectrum of reconstructed (black) and not reconstructed (red) events, (b) a surface plot of reconstructed events to express the relative abundance of events in  $P_\mu^{Gen} - \cos \theta_\mu^{Gen}$  plane

events are crowded near lower zenith angle (higher  $|\cos \theta_\mu|$ ) region of the plot. They can cross  $> 4$  no. of active planes rather easily compared to lower  $|\cos \theta_\mu|$  events. A surface plot of the reconstructed events is shown in figure 7.13(b). A monotonic decrease in the no. of reconstructed events is seen when  $|\cos \theta|$  is decreased. The steep decrease of the same along the  $P_\mu^{Gen}$  axis is due to the steep decrease of atmospheric neutrino flux with increasing neutrino energy. Among the reconstructed events, those with lower momenta ( $P_\mu < 1 \text{ GeV/c}$ ) and/or lower ( $|\cos \theta_\mu| < 0.5$ ) are affected more by multiple scattering, as seen from Eq.(94). So, the net charge identification efficiency and the momentum resolution etc. are poor for NUANCE generated neutrino events. However, the overall reconstruction is better compared to the existing reconstruction code (existing track-finder and track-fitter). This is shown in the following table 9: Let us here mention

Parameter	previously	currently	single $\mu$
Reconstruction efficiency	$\sim 40\%$	$\sim 40\%$	$\sim 40\%$
Charge id. efficiency	$\sim 80\%$	$\sim 88\%$	$\sim 93\%$
% Events with $p_{rec}$ better than 10% accuracy	$\sim 28\%$	$\sim 32\%$	$\sim 45\%$

Table 9.: NUANCE generated Muon reconstruction performance

that the entries in the table 9 are results of the Kalman filter itself. In fact, if Bethe Bloch energy loss is used for fully contained set of events, the fraction of events with momentum estimated within 10% accuracy increases to  $\sim 40\%$ . The final column of this table shows the corresponding estimates if *only* muons of every neutrino events are simulated. That is, if no hadrons in these events are simulated. This column is provided for comparison purposes only and *does not* represent the realistic detector performance.

### 7.4.7 Hadron energy calibration

Currently, the reconstruction program does not use the hits from an event in which there is no fitted track. This is because, there *could* many events that lead to shower of hits in the detector but no track. We have just seen in table 9 that  $\sim 60\%$  CC  $\nu_\mu$  events do not give any “reconstruct-able” tracks. It is important to realize that apart from these, there are many CC  $\nu_e$  events, NC events etc. also, which lead to shower of hits and no tracks in the detector. Thus, it is not possible to calibrate the hits in these events against  $(E_\nu - E_\mu)$ , because we do not know if the underlying event is a CC  $\nu_\mu$ , or CC  $\nu_e$  or usual NC events. On the other hand, if one calibrates the no. of hits against  $(E_\nu - E_\mu)$  for events with a reconstructed track, then  $> 98\%$  cases, one is dealing with hadron hits actually associated with a muon in a CC  $\nu_\mu$  event. The background of  $\sim 2\%$  comes from occasional tracks from NC events 6.3.1, occasional proton tracks from CC  $\nu_\mu$  events and occasional  $e^-$  tracks from CC  $\nu_e$  events.

The quantity that has been calibrated against  $(E_\nu - E_\mu)$  is simply the no. of hits identified as hits not belonging to the muon track. They may as well be loosely termed as ‘hadron hits’ where it is understood that these hits are ‘identified’ hadron hits and may not be the same as the genuine hadron hits in an event. We have already shown 6.3.2 that  $\sim 80\%$  cases, the pattern recognition program makes a correct decision about the identity of a hadron hit. This observable has been used to calibrate genuine hadron energy  $(E_\nu^{Gen} - E_\mu^{Gen})$ . It might be possible to use some derived observable (say, the size and shape of the ‘cloud’ of hadron hits) to calibrate the same and it could be insightful, but in this thesis the most simple observable (the no. of ‘hadron’ hits) has been used. The distribution of  $(E_\nu^{Gen} - E_\mu^{Gen})$  has been plotted for all reconstructed NUANCE events with a fixed no. of ‘hadron’ hits and has been fitted with a Vavilov distribution, as shown in figure 7.14(a). The procedure has been repeated until no. of ‘hadron’ hits in a given

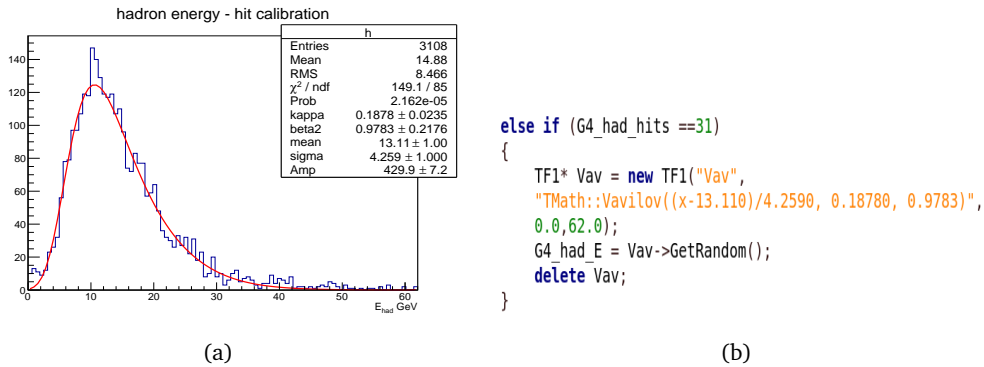


Figure 7.14.: (a) ‘Hadron’ hit-hadron energy calibration plot when no. of ‘hadron’ hits = 31, (b) corresponding hadron energy generation by ROOT based Vavilov random no. generator

event reaches 40. Beyond that, the no. of events are much less and the Vavilov fits do not converge properly. So, if in an event  $n$  no. of ‘hadron’ hits are observed, the corresponding hadron energy is *sampled* from a ROOT based Vavilov random number generator. This is shown in figure 7.14(b). The sampled energy is assigned to the energy of hadrons in the said event. The following table 10 shows the parameters for calibration

when  $n \in [31, 35]$ . The goodness of the Vavilov fits is also shown in terms of the  $\chi^2/\text{ndof}$ .

No. of hits	$\kappa$	$\beta^2$	mean	sigma	amplitude	$\chi^2/\text{ndof}$
31	0.1878	0.9783	13.11	4.259	429.9	149.1/85
32	0.1510	0.9836	13.22	4.477	402.1	81.2/85
33	0.1284	0.9999	13.47	4.458	374.2	116/85
34	0.1413	1.000	14.19	4.802	345.8	70.24/82
35	0.1454	0.9999	14.83	4.829	323.6	110.3/83

Table 10.: Hadron Hit energy calibration table for no. of hits  $\in [31, 35]$

## 7.5 INFLUENCE OF OTHER FACTORS

The quantitative aspects of reconstruction are the most important factors for the success of the ICAL experiment. However, it is clear from table 9, the reconstruction program is not performing great in this respect, though it improved the performance significantly compared to the existing code. But to improve it further, perhaps one needs to experiment with several detector parameters, like RPC strip width, magnetic field and thickness of iron plates. These parameters should be adjusted in such manners, that length  $L$  becomes higher, no. of measurements  $N + 1$  becomes higher, measurement errors become lower and magnetic field is higher. This is seen from Eq. (92) and from Eq. (94).

It has been verified that increasing the maximum magnetic field from  $\sim 1.5$  T to  $\sim 2.0$  T does not help as such to increase the percentage of reconstructed events with momentum estimated within 10% accuracy. This statement is valid for NUANCE events. For GEANT4 generated single muon events the momentum resolution becomes much better. NUANCE level muons are dominated by multiple scattering. Thus, slight increase of magnetic field is not that much effective in case of these events.

On the other hand, increase of the RPC strip width from 2.0 cm to 3.0 cm is seen to reduce efficiency of reconstruction for the NUANCE events from  $\sim 40\%$  to  $< 35\%$ . In fact, the charge id efficiency is also seen to go worse.

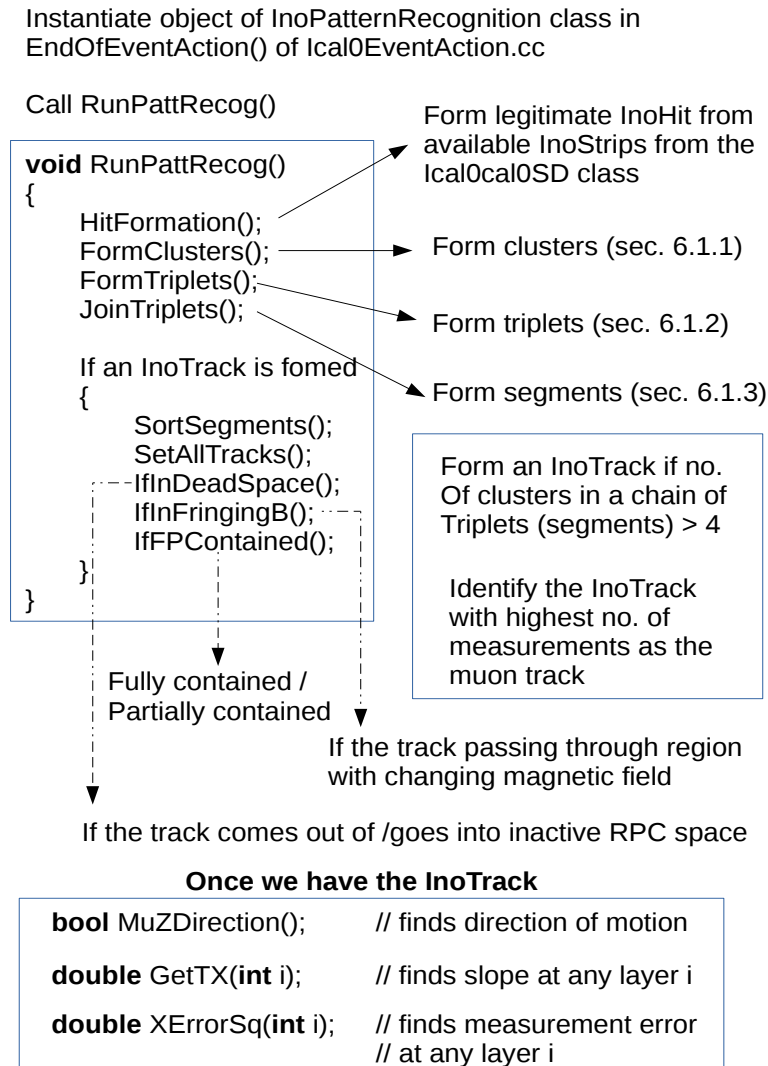
It appears that directly nothing can be done about the factor of  $\cos \theta$  in the angle-dependent term  $\frac{\sigma(\cos \theta)}{\cos \theta}$  in Eq. (91). The contribution of this term becomes harmful at higher zenith angles. One may only try to improve the estimation of the track curvature, which would improve  $\sigma(\cos \theta)$ .

## 7.6 FLOW CHART OF RECONSTRUCTION PROGRAM

In this section, we shall show the flow charts for the reconstruction programs. First, we shall show the chart for InoPatternRecognition code in figure 7.15(a) and then, for the InoTrackFitAlg code in figure 7.16(a).

### 7.6.1 InoPatternRecognition

In this section, the logical flow of the InoPatternRecognition class is shown. The corresponding sections in this thesis are referred to in appropriate places.



(a)

Figure 7.15.: Flow chart for InoPatternRecognition class

When the seed track is formed, that is passed to the InoTrackFitAlg class. The seed track properties have residuals shown in section 6.3.4. This InoPatternRecognition class is interfaced with the InoTrackFitAlg class properly. The latter directly reads the information about the seed track using the members (GetTX(), XErrorSq() etc.) of the InoPatternRecognition class.

## 7.6.2 InoTrackFitAlg

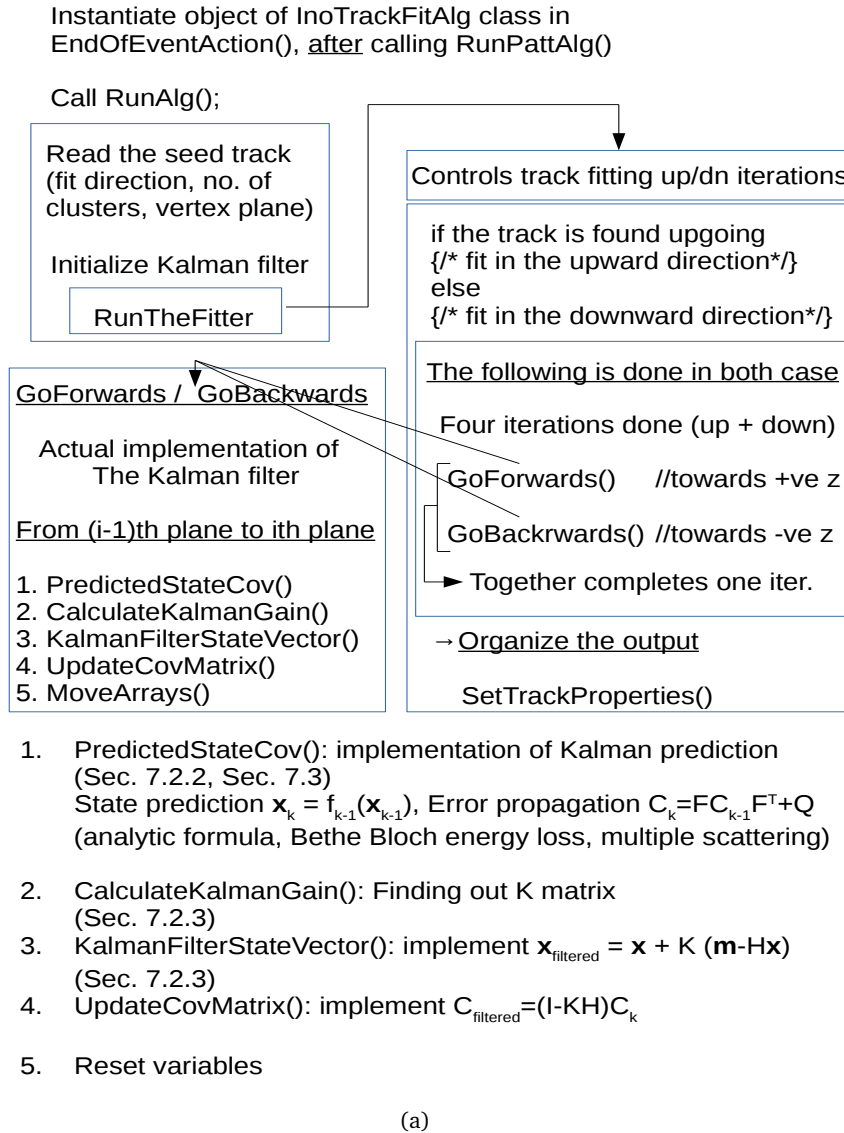


Figure 7.16.: Flow chart for InoTrackFitAlg class

The filter usually converges through four iterations controlled by RunTheFitter() function. As we have seen before, not all the reconstructed tracks are of very high qualities. Therefore, one must develop set of selection criteria that will select the set of good events. This is the topic of the following chapter.

Part III.

## Event Selection

---

EVENT SELECTION

---

## 8.1 INTRODUCTION

Neutrino oscillation analyses have been carried out so far in the INO-ICAL collaboration, assuming that the hits due to muons and those due to hadrons can be fully separated [28]. In these analyses, information about the muon reconstruction performance was taken into account through a look up table [100]. This is basically a parametrization of detector response to muons. However, this look up table was generated from the study of GEANT4 single muon MC events and hence, does not represent the true response of the detector to muons in the presence of hadron hits in realistic neutrino events. That the muon reconstruction performance worsens in presence of hadrons, has been seen in table 9. In this thesis, attempts were made to carry out the neutrino mass hierarchy sensitivity analysis using muons reconstructed in the presence of hadron shower for all CC neutrino events generated by NUANCE. In fact, the `InoPatternRecognition` class was developed out of the need to separate accurately the hits due to muons from those due to hadrons.

The set of NUANCE generated atmospheric neutrino events, reconstructed by the event reconstruction program, described in chapters 6 and 7, contains both sorts of events: those with very good reconstruction as well as those for which reconstruction is not so good. Previously it was seen in 7.4.3 and in 7.4.6 that the performance of track fitting deteriorates for events suffering from multiple scattering. Eq. (94) shows explicitly that the events with lower momenta and/or lower  $|\cos \theta|$  are prone to suffer from this. Thus, reconstruction is usually poor for these events. It is seen that out of all NUANCE generated  $\nu$  events,  $\sim 80\%$  events have  $P_\mu < 1 \text{ GeV}/c$  or  $|\cos \theta_\mu| < 0.5$  (i.e.  $\theta$  is between  $60^\circ$  and  $120^\circ$ ). This shows why  $\sim 60\%$  of these events are not reconstructed at all. Even among the reconstructed events,  $\sim 55\%$  have  $P_\mu < 1 \text{ GeV}/c$  or  $|\cos \theta_\mu| < 0.5$ . The statistics worsens alarmingly if one counts events that have  $P_\mu < 2 \text{ GeV}/c$  or  $|\cos \theta_\mu| < 0.5$ ; it is  $\sim 75\%$  of the total no. of reconstructed events. Effectively, only  $\sim 31 - 32\%$  events are reconstructed with their momenta estimated within 10% accuracy, as seen in table 9. The tricky part is that these events are mixed with all other reconstructed events and there is no direct way to recognize them. Hence, The most difficult part from the perspective of an experimentalist is to be able to select good events for performing physics analysis. Whether or not reconstructed properly, these events share similar characteristics. This makes the separation a really challenging task. The goal is to remove as many bad events (the ones with wrong charge identification, poor momenta estimation etc.) as possible without affecting the pool of good events. Once that is done, the good events can be used for performing the physics analyses.

During the thesis work, various trial and error methods were applied to achieve the separation. We shall first discuss them in section 8.2. These methods are based on

empirical observations. However, the cost-benefit ratio is found not to be so good for these trial and error methods. Many good events are also rejected along with the bad events when subjected to these methods. Therefore, other techniques were being searched and finally we applied some multi-variate techniques. This is found to be a better alternative in this respect. The work done on this topic will be discussed in section 8.3. Finally, we shall see what sort of events have been used to perform the physics analysis.

Let us here mention that no separate effort has been given to isolate CC events from NC events. It has already been dealt with in the pattern recognition package. It is found that NC background may be  $\sim 0.7\%$  in a typical atmospheric neutrino event sample 6.3.1 comprising both CC and NC events. Usually, the track reconstruction performance of these background events are not good, because the fitting program calculates energy loss assuming muon tracks whereas these tracks coming of NC background events are not due to muons. A good event selection routine, then, removes most of these events owing to the poor reconstruction. So, it is assumed that the contributions of such background events to the final sample (to be used for the physics analyses) will be very small.

## 8.2 TRIAL AND ERROR METHODS

Before the development of `InoPatternRecognition` class, the physics analysis with reconstructed data was carried out by simulation and reconstruction of *only* muons, coming of the NUANCE generated neutrino events. Hadrons of these events were not simulated as the separation efficiency of hadrons from muons was indeed very poor. The full simulation was attempted after the `InoPatternRecognition` class became fully operational. Anyway, even with single muon reconstruction, it was found that reconstruction of most of the events was bad. This was not surprising, because a majority of these muons were still being affected by multiple scattering due to lower  $P_{\mu}^{Gen}$  and lower  $|\cos \theta_{\mu}^{Gen}|$ . The problem was worse, because there was no direct way to distinguish better reconstructed events from all other reconstructed events. That time, a series of cuts were developed by trial and error methods, for separating the set of events that had been reconstructed better. In this section, we shall discuss about them using the example of charged current  $\nu_{\mu}$  events arising from *unoscillated* atmospheric  $\nu_{\mu}$  flux and the *swapped* atmospheric  $\nu_e$  flux ( $\nu_e \rightarrow \nu_{\mu}$ ). The meaning and motivation of the terms *unoscillated*, *swapped* etc. will be discussed in the next chapter. Here, we shall only talk about event selection procedures and performances for  $\nu_{\mu}$  events coming from these sources.

The NUANCE charged current data sets with 1000 years of ICAL exposure contain  $\sim 4000000$  events coming from *unoscillated* channel ( $\nu_{\mu} \rightarrow \nu_{\mu}$ ) and  $\sim 1700000$  events from *swapped* channel ( $\nu_e \rightarrow \nu_{\mu}$ ). The reconstruction efficiency is  $> 40\%$  if the minimum no. of layers to form an `InoTrack` is taken to be 3. However, in that case, about 10% NC events get identified as charged current event and get reconstructed. So, we fixed the minimum no. of allowed layers as 5. The corresponding charge identification efficiency (CID) and the percentage of muon events with momentum estimated within 10% accuracy (denoted by  $p10\%$ ) are shown next to the entry % of reconstructed events of the following table 11. Then, the events between  $\theta_{\mu}^{Rec} \in [81^{\circ} - 99^{\circ}]$  were removed, as fitting performance for  $\theta \rightarrow 90^{\circ}$  was known to be poor. This condition is represented by  $|\cos \theta_{\mu}^{Rec}|$  in the table. This only slightly changed the earlier statistics. In the third step, events with reduced  $\chi^2 < 3$  were accepted. Even this did not help at all from the

quantitative aspects of track fitting. Hence, the cut-off no. of the measurements along the track were increased gradually, as this would *increase*  $N$  as well as  $L$  of Eq. (92) and Eq. (94) and reduce the error in the momentum estimation.

Conditions	$\nu_\mu \rightarrow \nu_\mu$			$\nu_e \rightarrow \nu_\mu$		
	N	% CID	p10%	N	% CID	p10%
Total no. of CC $\nu_\mu$	4007677	-	-	1740150	-	-
% of reconstructed events	37.8%	90.3%	39.2%	32.1%	89.5%	37.3%
Events with $ \cos \theta  > 0.15$	37.2%	90.3%	39.6%	31.5%	89.4%	37.3%
Events with $\chi^2/\text{ndof} < 3$	35.8%	90.6%	40.0%	30.4%	89.7%	38.2%
Events with no. of hits > 6	27.7%	94.3%	44.3%	22.1%	93.9%	42.9%
Events with no. of hits > 7	24.2%	95.3%	46.4%	18.7%	95.1%	45.4%
Events with no. of hits > 10	18.8%	96.5%	50.3%	13.6%	96.4%	49.9%
Events with no. of hits > 14	11.1%	98.1%	57.7%	6.97%	98.2%	57.9%

Table 11.: Event selection results with trial and error

Finally, it was seen that to attain  $\sim 98.0\%$  charge identification efficiency, all events with no. of hits less than 15 were to be rejected. This roughly corresponds to cut-off length of 1.5 m (events with lower  $|\cos \theta|$  have greater  $L$ ) in the detector. The flat condition on the no. of events took toll on the statistics. Efforts were even made to make this criterion dependent on  $|\cos \theta|$ , but that did not help appreciably. On the other hand, increasing the cut-off in the no. of layers helped in reduction of the no. of events for which direction had been calculated wrong (section 6.3.3). Thus, a very tiny set of events survived the event selection criteria. In fact only  $\sim 450000$  events out of  $\sim 4000000$  survived in  $\nu_\mu \rightarrow \nu_\mu$  mode. In fact, it is seen from the table that to reject a single event with incorrect charge id,  $\sim 7$  events with correct charge id. were removed by the selection criteria. Clearly, this situation was quite unacceptable. Hence, we resorted to ROOT based multivariate techniques.

### 8.3 MULTIVARIATE TECHNIQUES

To exclude a small set of incorrect charge id. events from a much larger pool of correct charge id. events by multivariate techniques, first the network was trained with a sample consisting of signal and background events. Events with correct (incorrect) charge id. were defined to be signal events (background events). The following quantities (associated with track reconstruction) were used for the training purpose: (1)  $y$  position of the event vertex (because  $|y| > 6$  m represents the area of fringing magnetic field 7.4(b)), (2)  $p$ -Value of an event from  $\text{TMath::Prob}(\chi^2, \text{ndof})$ , (3) error in the parameter  $q/p$  at the vertex end and the rear end of the track, (4) the quantity  $\frac{N^- - N^+}{N^- + N^+}$ , where  $N^{+(-)}$  is the no. of measurement sites with  $q/p$  assigned +ve(-ve) by the filter. Clearly,  $N^- + N^+$  is the total no. of planes with measurement in an event. It was found that in some events, the sign of  $q/p$  fluctuated along the measurement sites  $k \in [1, N]$ . The reason behind this observation could be (but not limited to) the following: (a) inclusion of hadron hits, (b) irregular occurrence of measurements along the trajectory, (c) inefficiency of the track reconstruction code to take into account multiple scattering. Whatever be the reason, it is clear that in such cases, the filter is not confident enough about the sign of

$q/p$ . Hence, it is possible that this particular event reconstruction has not been good. The factor  $\frac{N^- - N^+}{N^- + N^+}$  is a measure of relative occurrence of either sign. When all the sites have -ve values of  $q/p$ , the factor equals  $-1$  and the event is more likely a  $\mu^-$  and vice versa.

ROOT based Adaptive Neural Networks and Boosted Decision Trees were trained with these quantities for a training sample. The performance of the training is shown in the following figure 8.1(a), 8.1(b), 8.1(c) and 8.1(d) for the latter. The program internally

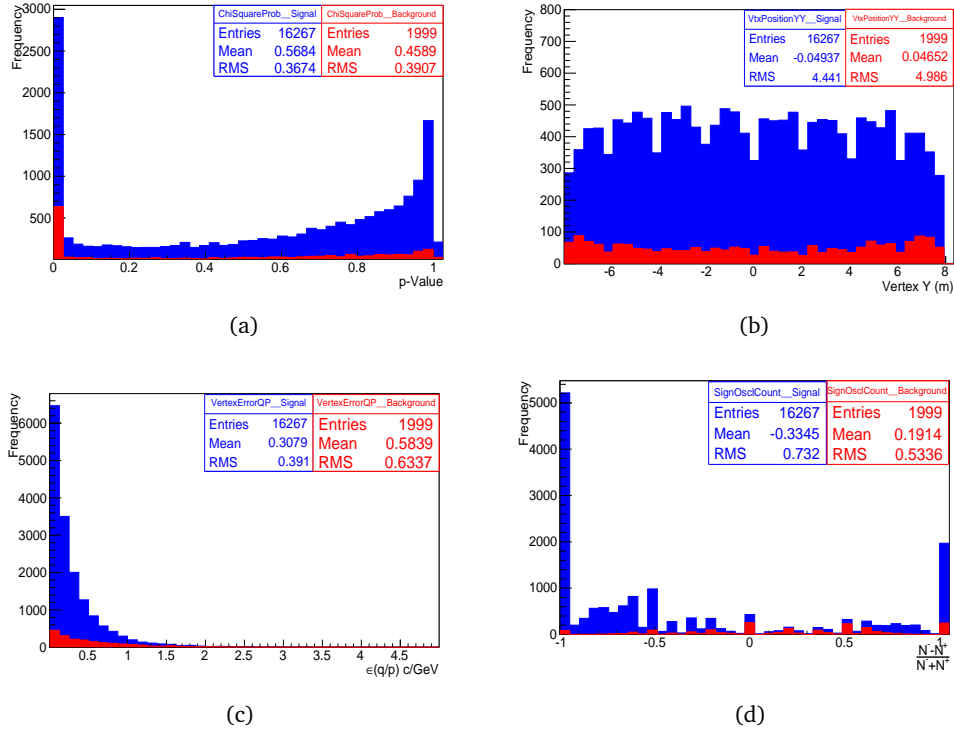


Figure 8.1.: Training plots for (a) chi square probability, (b) vertex y position, (c) error in  $q/p$  element of the state vector and (d)  $\frac{N^- - N^+}{N^- + N^+}$

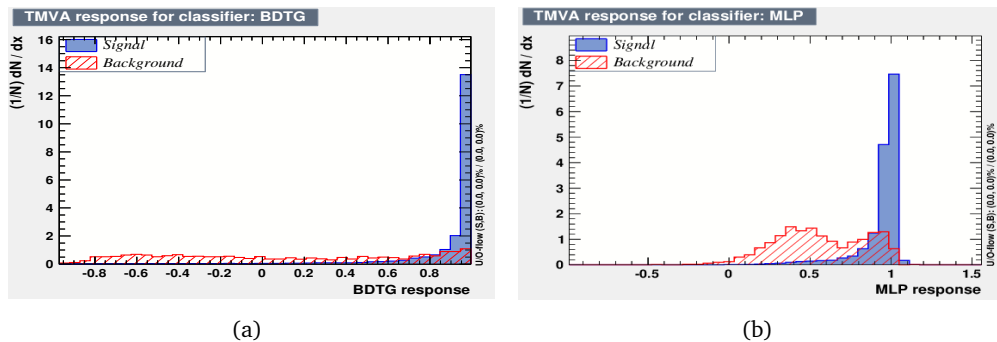


Figure 8.2.: Separation of signal like events and background like events by multivariate techniques: (a) BDT method (b) ANN method

computes all possible correlations among all the variables inserted into it. The network was checked for overtraining and was found okay. Once the training was over and weight

files were created, we passed every event of a general data sample through the trained network set in the **BDT** mode. The performance of separation is shown in the following figure 8.2(a). The same exercise was carried out with **ANN** and its performance, shown in figure 8.2(b), was found to be little poorer compared to **BDT**.

The following table 12 summarizes the event selection performance when BDTG is used. One can easily see that the selection efficiency is better in this case compared to table 11. For various values of the output of the neural network ( $x_0$ ). In this case, the no.

Conditions	$\nu_\mu \rightarrow \nu_\mu$			$\nu_e \rightarrow \nu_\mu$		
	N	% CID	p10%	N	% CID	p10%
Total no. of CC $\nu_\mu$	4005455	-	-	1740079	-	-
$x_0 = 0.650$	33.3%	97.3%	44.7%	28.9%	97.4%	44.0%
$x_0 = 0.700$	32.7%	97.6%	44.9%	28.5%	97.6%	44.1%
$x_0 = 0.750$	31.9%	97.9%	45.2%	27.8%	97.9%	44.7%
$x_0 = 0.800$	30.9%	98.1%	45.6%	26.9%	98.1%	45.0%
$x_0 = 0.825$	30.4%	98.3%	45.8%	26.4%	98.4%	45.2%
$x_0 = 0.850$	29.6%	98.5%	40.0%	25.8%	98.6%	45.3%
$x_0 = 0.875$	28.8%	98.7%	46.3%	25.0%	98.7%	45.6%
$x_0 = 0.900$	27.8%	98.9%	46.7%	24.2%	98.9%	45.7%

Table 12.: Event selection results with multivariate techniques

of muons which survive the event selection criteria is  $\sim 1100000$  out of  $\sim 4000000$  in 1000 years of exposure. In this case, the momentum resolution is poor as (a) the events have been reconstructed in the presence of hadrons and (b) the signal events in the neural network were identified as those with correct charge identification. No condition on the accuracy of momentum estimation were used in that level. The corresponding distributions for  $\frac{p^{Rec} - p^{Gen}}{p^{Gen}}$  and  $(\cos \theta^{Rec} - \cos \theta^{Gen})$  are shown in the following figures 8.3(a) and 8.3(b).

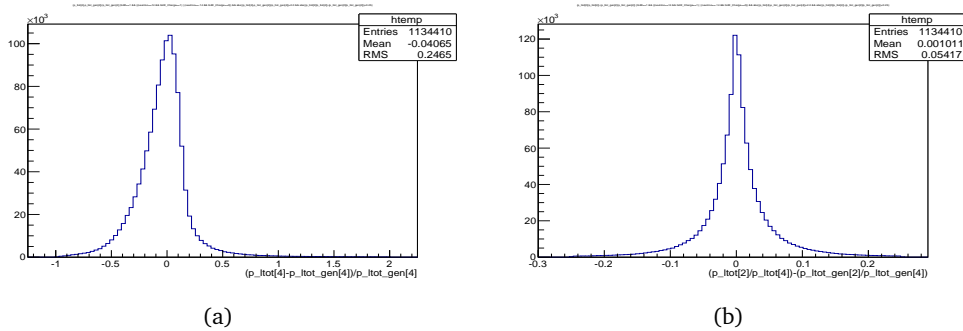


Figure 8.3.: Plots for (a) fractional error in momentum and (b) error in  $\cos \theta$  estimation, for events that survive multivariate techniques based event selection criteria.

These events were used for performing the neutrino oscillation analysis. Since the total no. of events is much higher compared to the trial and error methods 11, it is possible to have larger no. of events in every bin of the analysis.

Part IV.

Neutrino Mass Hierarchy  
Sensitivity Analysis and Results

---

## NEUTRINO MASS HIERARCHY SENSITIVITY ANALYSIS

---

### 9.1 INTRODUCTION

As have already been pointed out in the previous chapters, the major goal of the INO-ICAL experiment is to resolve the neutrino mass hierarchy. This will be achieved by collecting atmospheric neutrino event data over a decade or so. The sensitivity of the experiment to the mass hierarchy will directly depend on *how* well the detector is capable to measure the energy and direction of the final state particles produced in the neutrino events and *how* well it can distinguish between the neutrino events and the antineutrino events. The methods to perform these analyses and the corresponding efficiencies of ICAL detector have been discussed in the previous chapters on reconstruction and event selection. Using those information, the mass hierarchy sensitivity of the experiment will be determined in this chapter.

Since the real experiment has not been constructed yet, all the results are obtained from simulation. At the very early phase of these simulation studies, some preliminary works were carried out to give an estimate of the expected sensitivity for a decade of ICAL operation. These works [26], [101] were done when the R&D efforts of the RPC detector construction and the simulation were just initiated. The estimates reported in these works are rather optimistic. The problem was revisited as the preliminary detector response to single muons were obtained using a GEANT4 simulation. A look up table of muon reconstruction performance was prepared that tabulated the efficiencies of reconstruction and charge identification, momentum and zenith angle resolutions of the detector for various input momenta and directions. The ‘muons’ of the NUANCE charged current (CC) data set were subjected to these detector response functions. The output of the operation suggests *how* well the detector is capable of measuring the properties of the muons generated in the charged current neutrino interactions. This was the first result on ‘neutrino mass hierarchy sensitivity’ [27] of ICAL which was based on the detector simulation. It was followed by another work [28] that included also the estimated hadron energy in the events.

However, the estimates projected by these works needed further revisions, because the way the detector response was incorporated in the analyses was not satisfactory. First of all, the reconstruction performance of GEANT4 generated single muons cannot be taken to be the true response of the detector to muons produced in the realistic neutrino events. Because the presence of hadrons deteriorates the reconstruction performance of muons. In fact, in the present proposed detection mechanism of charged particles in ICAL (via RPC detectors), there is no obvious way to distinguish the hits due to muons from the hits due to hadrons. The work [27] was done with the reconstruction performance of single muons (generated by GEANT4) whereas the work [28] assumed that the hits

due to muons and those due to hadrons can be separated with 100% accuracy. But in reality this does not hold true, even with an improved pattern recognition algorithm as discussed in chapter 6.

Secondly, these works did not address the issue of event selection. In the realistic case, properly reconstructed events are always mixed up with poorly reconstructed events. There are no obvious ways to separate them from each other. So, the question is how to find the *particles with correct charge identification and good momentum estimation* among all reconstructed particles. This consideration was absent from these works.

In this part of the thesis work, these issues were confronted directly and a more realistic estimates of the hierarchy sensitivities were obtained. The reported sensitivity is the best estimate obtained with currently available reconstruction and event selection tools. However, with further improvement of these techniques, it might be possible to have even better estimate. We shall start with a discussion on the generation of neutrino events using the NUANCE atmospheric neutrino event generator. In the following section, a brief outline of the analysis procedure will be given. The first step is event generation. The final state particles generated in these events were passed through the ICAL code for simulation and reconstruction, as described in chapters 5, 6 and 7. The good quality events were selected using the methods described in chapter 8. The selected events were used for the oscillation analysis. This whole chain will be explained with a flow chart. Finally, we shall present the results on hierarchy sensitivity using fixed oscillation parameters.

## 9.2 EVENT GENERATION WITH NUANCE

NUANCE is a Monte Carlo event generator for atmospheric neutrinos, written in Fortran. It calculates the neutrino events in two steps. At first, one must supply a minimal detector geometry setup and a pertinent atmospheric neutrino flux to the program. Interfacing the full detector geometry with NUANCE is not possible, even with its latest version released in 2002. Since in ICAL the main target mass is iron, the dimension of a single iron plate in a plane ( $48\text{ m} \times 16\text{ m} \times 0.056\text{ m}$ ) is specified to the program. All events in 150 iron plates of ICAL are initially generated in this plate. Then the event vertices are smeared across these 150 layers uniformly using a translation code. This code is used also to separate the CC  $\nu_\mu$ , CC  $\nu_e$ , NC  $\nu_\mu$  and NC  $\nu_e$  events. During the specification of the detector geometry, the information regarding other elements (used in RPCs) that could contribute in neutrino interactions is also provided to the program.

The neutrino events are calculated in two steps. First, the rate of neutrino interactions is calculated from the known neutrino cross sections and from the neutrino flux using the default geometry of the detector. The output of this step is a rate file which is used as one of the inputs of the second step on the actual event generation. In the second step, events are generated for the operation of the detector in a specified no. of years. The exposure of the detector is defined as the no. of years times the detector mass. Therefore, for 10 years of ICAL operation, the exposure is  $50 \times 10\text{ kton-years} = 500\text{ kton years}$ . Neutrino events along with the four momenta of the final state particles generated in these events during this exposure of the detector are written to an ASCII file. The detector simulation code is interfaced with this ASCII output format.

There are two ways to implement neutrino oscillation in the analysis. The first method is to ask NUANCE to incorporate oscillation while neutrinos are traversing through the

earth matter. In this case, survived/oscillated set of muon neutrinos reach the detector. Hence, charged current events corresponding to these  $\nu_\mu$  are generated using NUANCE within the detector. This chain of actions follows what happens in reality (that is, first  $\nu$  oscillation and then the generation of  $\nu$  events). However, this approach has an issue: if the sensitivity is required to be marginalized over the  $3\sigma$  range of oscillation parameters, this approach would become impractical. Because, in that case, a large no. of survived/oscillated data sets need to be prepared, corresponding to different oscillation parameters within the  $3\sigma$  range of existing best fit values. All these data require to be simulated and reconstructed by spending a lot of computational power. The same problem arises if neutrino oscillation is implemented through the event re-weighting method prior to the detector simulation.

The second method is to *assume* that all the neutrinos that reach the detector are  $\nu_\mu$ . All these are simulated and reconstructed only *once* and then the neutrino oscillation is implemented through the event re-weighting method. In this way, one can easily prepare a large set of reconstructed as well as oscillated neutrino events, each with different neutrino oscillation parameters, without requiring to repeat the detector simulation processes.

To implement this method, first NUANCE is barred from applying the survival probability  $P_{\mu\mu}$  to the atmospheric  $\nu_\mu$  flux and is asked to tag the  $\nu_e$  flux as the  $\nu_\mu$  flux. Hence, *unoscillated*  $\nu_\mu$  flux and *swapped*  $\nu_\mu$  flux reach the detector. The oscillation is applied upon all the neutrino events when detector simulation and reconstruction are over, through event reweighting. This method is a Monte Carlo accept-reject method to apply survival probability  $P_{\mu\mu}$  to *unoscillated*  $\nu_\mu$  flux and oscillation probability  $P_{e\mu}$  to *swapped*  $\nu_\mu$  flux. A random number, generated uniformly between 0 and 1, is compared against the survival/oscillation probabilities to decide whether or not an event should be considered survived/oscillated. For the analysis performed during this thesis, the second method was adopted to remain consistent with the previous works [11].

For performing the neutrino mass hierarchy analysis in ICAL, 100 sets of data file having 10 years of exposure each was generated. Every CC  $\nu_\mu$  data set contains  $\sim 40000$  *unoscillated* events and  $\sim 17000$  *swapped* events. The energy and momenta of the neutrino are shared among all the final state particles whose number vary between 2 and 20 (see figure 6.6(a)). For CC  $\nu_\mu$  events one of the outgoing particles is a muon and ICAL is expected to be able to observe the corresponding muon track in the detector, because of its minimum ionizing nature.

### 9.3 PLAN OF MASS HIERARCHY SENSITIVITY ANALYSIS

To obtain the sensitivity of the experiment to neutrino mass hierarchy, a given hierarchy is chosen to be the true hierarchy. That is, we assume that nature chooses this hierarchy. Therefore, the data set observed in the detector after the simulation, reconstruction and event selection is already an instance of the true hierarchy, as it is observed in nature. Now, to test which hierarchy (normal or inverted) fits the data better, the observed data is fitted against the predictions of the normal hierarchy (NH) and the inverted hierarchy (IH). These predictions are obtained by scaling down one thousand years of data set (that is compiled from 100 data sets each with 10 years of exposure) to ten years. This reduces the fluctuation in the no. of generated events at NUANCE level.

The  $\chi^2$  between the observed data (that follows the true hierarchy chosen by nature) and the fits are compared to rule out the wrong hierarchy. The model that assumes correct hierarchy leads to a  $\chi^2$  smaller than that produced by the model that uses incorrect hierarchy. The difference between these two  $\chi^2$ s gives the sensitivity of the experiment to resolve the neutrino mass hierarchy problem. The plan of the analysis is shown through a schematic diagram in figure 9.1.

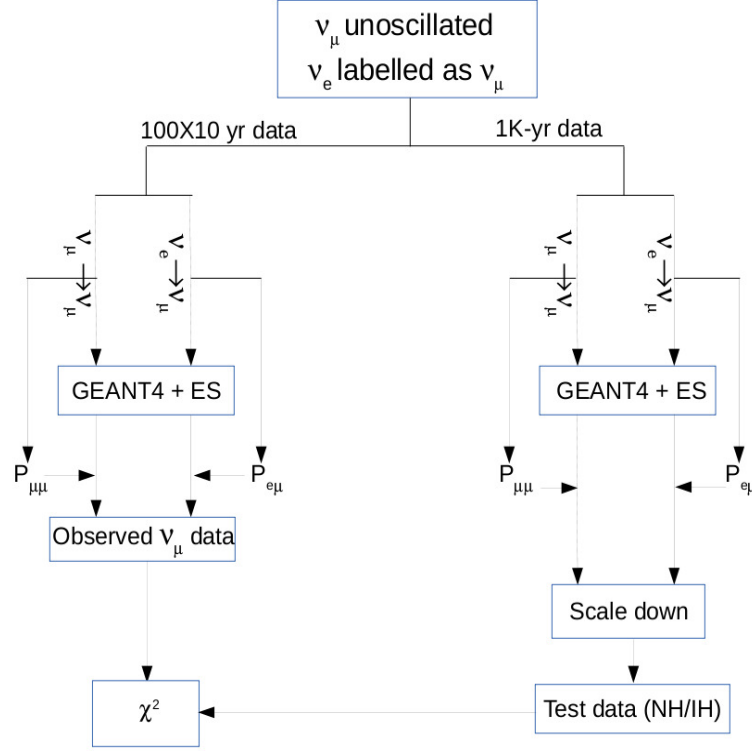


Figure 9.1.: plan for  $\nu$  mass hierarchy sensitivity analysis

The above figure shows the observed data set (left) and the modeled data set (right) that undergo through the same chain of simulation, reconstruction (GEANT4) and event selection (ES). The only difference is that in case of theoretical data set (which is first modeled with NH and then modeled with IH), the full one thousand years of data set is scaled down to ten years to reduce the statistical fluctuation in the no. of generated neutrino events.

A binned  $\chi^2$  analysis is performed by binning the muons in signed momentum (charge  $q$  times momentum  $P_\mu$ :  $q \cdot P_\mu$ ) and  $\cos \theta_\mu$  plane. As many of these bins might have zero muons, the usual Gaussian definition of  $\chi^2$  [102] is avoided and the binning is performed according to the Poissonian definition of  $\chi^2$  [103]:

$$\chi^2(\mu^\pm) = \sum_{i=1}^{N_E} \sum_{j=1}^{N_{\cos\theta}} [2(N_{ij}^{pred} - N_{ij}^{obs}) - 2N_{ij}^{obs} \ln \frac{N_{ij}^{pred}}{N_{ij}^{obs}}] \quad (95)$$

That is, the plane  $qP_\mu - \cos \theta_\mu$  is divided into small two dimensional cells and the muons are filled into the cells according to their momenta and directions. Each small cell contributes to the total  $\chi^2$ , as shown in Eq. (95). The quantity  $N_{ij}^{obs}$  denotes the

observed no. events in a given cell. The assignment of a muon to a cell is done according to its reconstructed  $qP_\mu$  and  $\cos\theta_\mu$ , as measured by the detector. The observed profile of events in the  $qP_\mu - \cos\theta_\mu$  plane carries the signature of the mass hierarchy chosen by the nature. On the other hand,  $N_{ij}^{pred}$  denotes the true no. events in a given cell, as predicted by a given model (NH or IH).

The no.  $N_{ij}^{pred}$  is different, depending on whether NH or IH is the true hierarchy. This follows from the fact that the oscillation probabilities depend on the matter effect which in turn, depend on the sign of  $\Delta m^2$ , as was seen in Eq.(27). The corresponding difference in the oscillation probabilities for  $\Delta m^2 > 0$  or  $\Delta m^2 < 0$  is shown in the following figure 9.2:

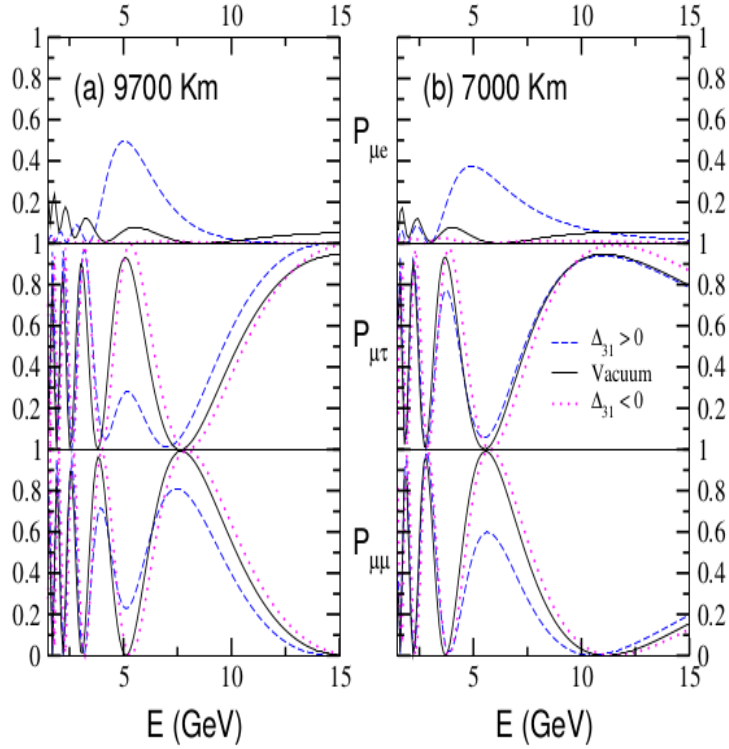


Figure 9.2.: Difference of neutrino oscillation probabilities for NH ( $\Delta_{31} > 0$ ) and for IH ( $\Delta_{31} < 0$ ) for two values of baselines  $L$ . Thus,  $N_{ij}^{pred}$  at every  $ij^{th}$  bin is different depending on whether calculated based on NH or IH. The figure is adopted from [6]

Thus, fitted  $\chi^2$  is different, depending on whether NH or IH is being fitted against the data. The wrong model will give  $\langle\chi_{false}^2\rangle$  which is expected to be greater than  $\langle\chi_{true}^2\rangle$  that results if the observed data is fitted with the correct model. In previous analyses [27], [28] etc.  $\langle\chi_{true}^2\rangle$  was zero, because both the observed data  $N_{ij}^{obs}$  and the data  $N_{ij}^{pred}$  predicted with correct model were scaled down from the 1000 years data set. This scaling down also resulted in the fractional no. of observed events in the bins used in the analysis. The present analysis is free from these issues.

We have assumed that the NH is the true hierarchy chosen by the nature and calculated the sensitivity of the experiment. The results are shown in the next section. Fixed values of the neutrino oscillation parameters were used in this analysis. Events were binned in

5 bins in  $|qP_\mu|$  between  $[0.1,100]$  GeV/c (i.e. 5 bins for  $\mu^+$  and 5 bins for  $\mu^-$ ) and 45 bins in  $\cos\theta_\mu$  between  $[-1,+1]$ .

#### 9.4 MASS HIERARCHY SENSITIVITY RESULT

The distribution of the events from a 10 years data file used for physics analysis in  $qP_\mu - \cos\theta_\mu$  plane is shown in the following figure 9.3:

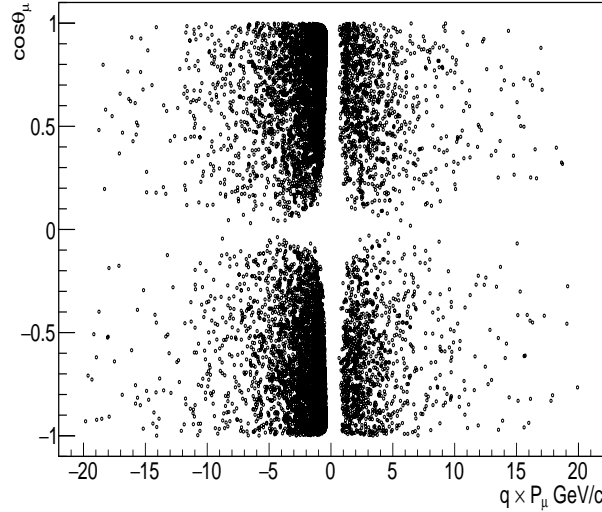


Figure 9.3.: Distribution of events in  $q \times P_\mu - \cos\theta_\mu$  plane

Because of the nature of the distribution, it is not possible to avoid cases where the no. of events in a bin becomes zero. Specifically, the no. of muons drops sharply when energy is increased. Hence, only 5 bins in energy were used  $E_\mu \in [0.10, 1.80, 3.50, 5.50, 10.0, 100]$ . On the other hand, a non-uniform binning scheme with minimum width of 0.03 is used to bin the events in  $\cos\theta_\mu$ . It is possible to perform a finer binning in  $\cos\theta_\mu$ , because the distribution extends up to  $|\cos\theta_\mu| \rightarrow 0.2$ . With this binning scheme,  $> 89.3\%$  bins in  $\mu^-$  and  $> 83.5\%$  bins in  $\mu^+$  have at least one event. Thus, 450 bins for  $\mu^-$  and  $\mu^+$  have been used. The total no. of events, the no. of filled bins and the no. of bins with no events are shown in the following table 13:

The bins with zero no. of observed events do not contribute to the total  $\chi^2$  because of the Poissonian definition of  $\chi^2$ . These bins were removed from the analysis, such that no divergence is observed due to the factor  $\ln \frac{N_{ij}^{pred}}{N_{ij}^{obs}}$  in the definition (95). In the above figure 9.4, the histogram with red line-color represents  $\chi_{true}^2$  between observed data and the fit with the correct model (NH, in this case) and the other histogram stands for  $\chi_{false}^2$  between observed data and the incorrect model (NH, in this case). Clearly, the  $\chi^2$  of the fits are seen to be of the same order ( $\chi^2 \sim 450$ ). However, average value of  $\chi_{false}^2$  is greater, corresponding to some non-zero sensitivity of the experiment. The two distributions have considerable overlapping with each other. Not only that, in some specific cases,  $\chi_{false}^2$  is found less than  $\chi_{true}^2$ . In the following figure 9.5 the sensitivities for an ensemble of 100 identical INO-ICAL experiments are shown. The mean sensitivity

Data set	No. of $\mu^-$	No. of $\mu^+$	% of filled $\mu^-$ bins	% of filled $\mu^+$ bins
1	4896	1290	90.22%	87.11%
2	4959	1281	95.11%	87.55%
3	4951	1304	94.22%	88.00%
4	5032	1193	90.22%	88.89%
5	5123	1291	93.33%	85.78%
6	4901	1301	90.67%	86.22%
7	4950	1236	92.00%	88.44%
8	5014	1235	91.11%	90.22%
9	4878	1292	90.67%	85.78%
10	4839	1295	92.00%	84.89%

Table 13.: Event Sample for oscillation analysis

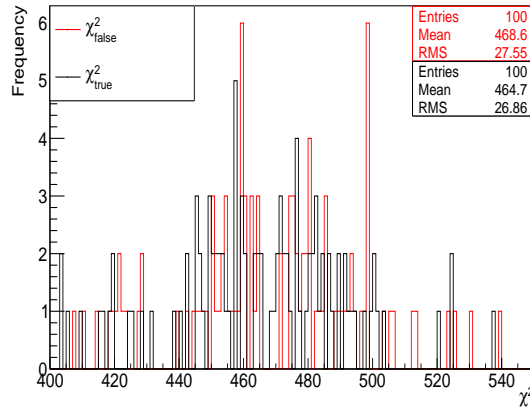


Figure 9.4.: Overlapped distributions of  $\chi^2_{true}$  and  $\chi^2_{false}$

of all these experiments is found to be  $\sim \sqrt{4}\sigma \approx 2\sigma$  with which the wrong hierarchy can be rule out after 10 years of ICAL operation.

## 9.5 SCOPE OF IMPROVEMENTS

The reported sensitivity is considerably lower compared to previously projected estimates by Ghosh et al. [27]. They obtained  $\Delta\chi^2 \sim 7.0$  for 10 years of ICAL operation. The reduction in the estimated  $\mu$  sensitivity is due to incorporation of the detector response in a more realistic manner.

On retrospect of the doctoral works performed in this thesis, it appears that the improvement of the mass hierarchy sensitivity of the INO-ICAL detector will be rather challenging. Efforts from various corners of the experiment are essential to achieve a sensitivity  $3\sigma$  or more. Whereas not much improvement of the Kalman filter is foreseen, ample amount of work needs to be done in separating the hits due to muons from those due to hadrons. The present form of the pattern recognition code can be a starting point in this work. With a better separation performance, the track fitting efficiency will automatically improve. Some groups within INO-ICAL collaboration have started

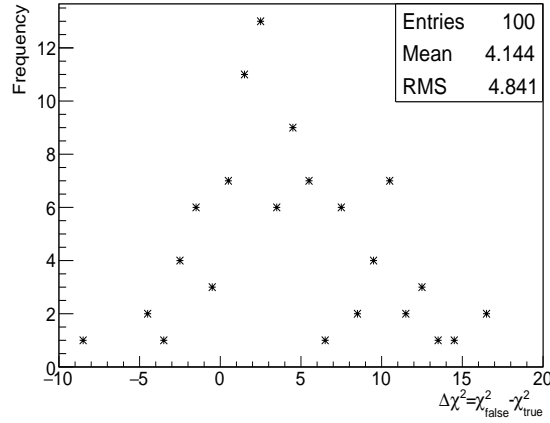


Figure 9.5.:  $\nu$  mass hierarchy sensitivity plot of ICAL experiment, assuming NH as the true hierarchy

working on this issue by implementing neural networks, but these attempts have not very successful. If some sort of information about the analogue shape of the pulses generated in RPCs is stored, perhaps that could be used as one of the parameters for identification of hadron hits. Another important aspect is event selection, on which there has been practically no works apart from what has been done during this thesis. It is not an easy task to separate a properly reconstructed track from a poorly reconstructed track which looks similar to the former from the geometrical appearance. So, these two aspects are the most important issues that seem relevant at this point.

On the other direction, works should also be directed towards alternative ways for performing the neutrino oscillation analysis. There has already been some works on the incorporation of muonless events to obtain some sensitivity to the neutrino mass hierarchy [104]. Apart from this, new efforts needs to be given towards performing the oscillation analysis with a proper scheme of binning. The rectangular binning scheme used in this thesis work and all the previous works on ICAL physics potentials [27], [11], [28], [105] is bound to have widely varying no. of events across the  $qP_\mu - \cos\theta_\mu$  plane, as shown in figure 9.2. This induces uncertainties in the no. of events in a bin. A polar binning scheme may instead be tried to bin the events. This must treat  $\mu^-$  and  $\mu^+$  separately, because the relative occurrence of  $\mu^+$  is about one third of that of  $\mu^-$ .

Part V.  
Appendix

---

## APPENDIX: A

---

The calculation of the propagator matrix in [87] was facilitated by the use of *SC* coordinate system  $(x_{\perp}, y_{\perp}, z_{\perp})$ , where  $x_{\perp}$  is along the track direction and  $y_{\perp}$  and  $z_{\perp}$  are chosen to be locally orthogonal to the track. In this frame, the detector planes are the planes of constant  $x_{\perp}$ , and therefore,  $\delta(dl)$  in section 7.3.3 is exactly equal to  $\delta(dx_{\perp})$  and both  $\delta(dy_{\perp})$  and  $\delta(dz_{\perp})$  are equal to zero. This frame is related to the Cartesian coordinates by the following equation [87]:

$$\begin{bmatrix} x_{\perp} \\ y_{\perp} \\ z_{\perp} \end{bmatrix} = \begin{bmatrix} \cos \lambda \cos \phi & \cos \lambda \sin \phi & \sin \lambda \\ -\sin \phi & \cos \phi & 0 \\ -\sin \lambda \cos \phi & -\sin \lambda \sin \phi & \cos \lambda \end{bmatrix} \begin{bmatrix} x \\ y \\ z \end{bmatrix} \quad (96)$$

where  $\phi$  is the azimuthal angle and  $\lambda$  is the dip angle and is related to the zenith angle  $\theta$  as  $\lambda = 90^\circ - \theta$ . It has been shown that in the *SC* system, that the infinitesimal displacement of the track in terms of infinitesimal deflections  $(d\lambda, d\phi)$  in the magnetic field can be written as:

$$\begin{bmatrix} x'_{\perp} \\ y'_{\perp} \\ z'_{\perp} \end{bmatrix} = \begin{bmatrix} 1 & (\cos \lambda d\phi) & d\lambda \\ -\cos \lambda d\phi & 1 & \tan \lambda (\cos \lambda d\phi) \\ -d\lambda & -\tan \lambda (\cos \lambda d\phi) & 1 \end{bmatrix} \begin{bmatrix} x_{\perp} \\ y_{\perp} \\ z_{\perp} \end{bmatrix} \quad (97)$$

which corresponds to a deflection of angle  $d\vec{\alpha}$  (due to magnetic field), given by:

$$d\vec{\alpha} = \begin{bmatrix} \sin \lambda d\phi \\ -d\lambda \\ \cos \lambda d\phi \end{bmatrix} \quad (98)$$

We want to find the corresponding equations in ICAL. With the help of  $3 \times 3$  Jacobian matrix in Eq.(96), we do similarity transformation of Eq.(97) and obtain:

$$\begin{bmatrix} x' \\ y' \\ z' \end{bmatrix} = \begin{bmatrix} 1 & d\phi & -\cos \phi d\theta \\ -d\phi & 1 & -\sin \phi d\theta \\ \cos \phi d\theta & \sin \phi d\theta & 1 \end{bmatrix} \begin{bmatrix} x \\ y \\ z \end{bmatrix} \quad (99)$$

corresponding to an angle  $d\vec{e} = \kappa \frac{q}{P} (\mathbf{e} \times \mathbf{B}) dl$  [Eq.(8) in [18] with  $\mathbf{e} = (\frac{t_x}{T}, \frac{t_y}{T}, \frac{1}{T})$  where:

$$d\vec{e} = \begin{bmatrix} \sin \phi d\theta \\ -\cos \phi d\theta \\ -d\phi \end{bmatrix} = \kappa \frac{q}{P} \frac{1}{T} \begin{bmatrix} -B_y \\ +B_x \\ (t_x B_y - t_y B_x) \end{bmatrix} dl \quad (100)$$

Eq.(100) says that the direction of the particle of momentum  $P$  is rotated by the magnetic field  $\mathbf{B}$  through an angle  $d\vec{e}$  over a track length  $dl$ . As the track of the particle is followed

from  $\mathbf{r}(z)$  to  $\mathbf{r}(z + dz)$  an error  $\delta$  in the estimation of the differential increment in the particle track length  $dl$  happens due to curvature of the track in magnetic field (Fig. 10.1). From Eq.(73), we see that  $\delta(dl)$  depends on  $\delta(dz)$ .

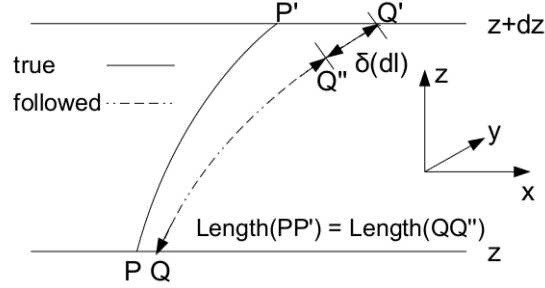


Figure 10.1.:  $\delta(dl)$  Correction

$$\begin{bmatrix} \delta x \\ \delta y \\ \delta z \end{bmatrix}_{\mathbf{r}(z+dz)} = \begin{bmatrix} 1 & d\phi & -\cos \phi d\theta \\ -d\phi & 1 & -\sin \phi d\theta \\ \cos \phi d\theta & \sin \phi d\theta & 1 \end{bmatrix} \begin{bmatrix} \delta x \\ \delta y \\ \delta z \end{bmatrix}_{\mathbf{r}(z)} + \begin{bmatrix} \delta(dx) \\ \delta(dy) \\ \delta(dz) \end{bmatrix} \quad (101)$$

The errors  $\delta x$ ,  $\delta y$  and  $\delta z$  at  $\mathbf{r}(z)$  propagate to  $\mathbf{r}(z + dz)$  according to Eq.(99). Apart from these, the errors  $\delta(dx)$ ,  $\delta(dy)$  and  $\delta(dz)$  also creep in due to the curvature of the track. The total errors  $\delta x$ ,  $\delta y$  and  $\delta z$  at  $\mathbf{r}(z + dz)$  are concisely given by Eq.(101).

We found the key relation Eq.(100) from Eq.(97) (valid in SC system) by using  $(3 \times 3)$  Jacobian (Eq.(96)) for coordinate transformation between the SC system and the Cartesian system. The propagator in the SC system [20], derived from helix model, was not directly used to express  $\delta(dl)$  in terms of  $\delta x$  etc. In fact, the propagator matrix  $F_{k-1}$  in section 7.3 is based on the analytic formulae for track extrapolation. Of course, one can obtain the transformed propagator (equipped with these formulae) in SC/perigee system by using the  $(5 \times 5)$  Jacobian matrices (Eq. A24, A25, A28, A29) derived in [106]. They are very helpful when  $F_{k-1}$  is not known in the required system, but is known in some other system.

Part VI.  
Bibliography

---

## BIBLIOGRAPHY

---

- [1] Kai Zuber. *Neutrino physics*. CRC Press, 2011.
- [2] M Sajjad Athar, M Honda, T Kajita, K Kasahara, and S Midorikawa. Atmospheric neutrino flux at ino, south pole and pyhäsalmi. *Physics Letters B*, 718(4):1375–1380, 2013.
- [3] Tapasi Ghosh. *Development of Track Reconstruction and Data Analysis Techniques for Neutrino Experiments*. PhD thesis, Variable Energy Cyclotron Center, 2009.
- [4] Satyanarayana Bheesette. *Design and Characterisation Studies of Resistive Plate Chambers*. PhD thesis, INDIAN INSTITUTE OF TECHNOLOGY BOMBAY, 2009.
- [5] MS Athar, INO Collaboration, et al. a report of the ino feasibility study. *Updated from the earlier Interim Report of May*, 1:2005, 2006.
- [6] Raj Gandhi, Pomita Ghoshal, Srubabati Goswami, Poonam Mehta, and S Uma Sankar. Earth matter effects at very long baselines and the neutrino mass hierarchy. *Physical Review D*, 73(5):053001, 2006.
- [7] Carlo Giunti and Chung W. Kim. *Fundamentals of Neutrino Physics and Astrophysics*. Oxford University Press, USA, 2007.
- [8] Y Fukuda, T Hayakawa, E Ichihara, K Inoue, K Ishihara, H Ishino, Y Itow, T Kajita, J Kameda, S Kasuga, et al. Evidence for oscillation of atmospheric neutrinos. *Physical Review Letters*, 81(8):1562, 1998.
- [9] John Bahcall. Solving the mystery of the missing neutrinos. *arXiv preprint physics/0406040*, 2004.
- [10] Michael F Altmann, Rudolf L Mößbauer, and Lothar JN Oberauer. Solar neutrinos. *Reports on Progress in Physics*, 64(1):97, 2001.
- [11] Tarak Thakore, Anushree Ghosh, Sandhya Choubey, and Amol Dighe. The reach of ino for atmospheric neutrino oscillation parameters. *Journal of High Energy Physics*, 2013(5):1–21, 2013.
- [12] William R. Leo. *Techniques for Nuclear and Particle Physics Experiments: A How-to Approach*. Springer, 1994.
- [13] Moon Moon Devi, Anushree Ghosh, Daljeet Kaur, SM Lakshmi, Sandhya Choubey, Amol Dighe, D Indumathi, Sanjeev Kumar, MVN Murthy, and Md Naimuddin. Hadron energy response of the iron calorimeter detector at the india-based neutrino observatory. *Journal of Instrumentation*, 8(11):P11003, 2013.
- [14] John Stuart Marshall. *A study of muon neutrino disappearance with the MINOS detectors and the NuMI neutrino beam*. PhD thesis, University of Cambridge, 2008.

- [15] Fujii Keisuke. Extended kalman filter. *The ACFA-Sim-J Group*, pages pp. 7, 15–17, 20, 2002.
- [16] C Milstène, G Fisk, and A Para. Muon id at the ilc. *Journal of Instrumentation*, 1(10):P10003, 2006.
- [17] Kolahal Bhattacharya, Arnab K Pal, Gobinda Majumder, and Naba K Mondal. Error propagation of the track model and track fitting strategy for the iron calorimeter detector in india-based neutrino observatory. *Computer Physics Communications*, 185(12):3259–3268, 2014.
- [18] S. Gorbunov and I. Kisel. Analytic formula for track extrapolation in non-homogeneous magnetic field. *Nucl.Instrum.Meth.*, A559:148–152, 2006.
- [19] Kolahal Bhattacharya. Range-Momentum table for convergence of q/p element in Kalman filter. [http://www.ino.tifr.res.in/inowiki/index.php?option=com\\_content&view=article&id=53:range-momentum-table-for-convergence-of-qp-element-in-kalman-filter&catid=1:physics-and-simulations-public-&Itemid=2](http://www.ino.tifr.res.in/inowiki/index.php?option=com_content&view=article&id=53:range-momentum-table-for-convergence-of-qp-element-in-kalman-filter&catid=1:physics-and-simulations-public-&Itemid=2), 2015.
- [20] W Wittek. Error propagation with energy loss: second addendum. Propagation of errors along a particle trajectory in a magnetic field. Technical Report EMC-80-15-ADD-2, CERN, Geneva, May 1982.
- [21] A Fontana, P Genova, L Lavezzi, and A Rotondi. Track following in dense media and inhomogeneous magnetic fields. *PANDA Report PVI01-07*, pages pp. 3–6, 19–28, 2007.
- [22] Animesh Chatterjee, KK Meghna, R Kanishka, Tarak Thakore, Vipin Bhatnagar, R Gandhi, D Indumathi, NK Mondal, and Nita Sinha. A simulations study of the muon response of the iron calorimeter detector at the india-based neutrino observatory. *Journal of Instrumentation*, 9(07):P07001, 2014.
- [23] E.J. Wolin and L.L. Ho. Covariance matrices for track fitting with the Kalman filter. *Nucl.Instrum.Meth.*, A329:493–500, 1993.
- [24] R Frühwirth and M Regler. On the quantitative modelling of core and tails of multiple scattering by gaussian mixtures. *Nuclear Instruments and Methods in Physics Research Section A: Accelerators, Spectrometers, Detectors and Associated Equipment*, 456(3):369–389, 2001.
- [25] Kati Lassila-Perini and László Urbán. Energy loss in thin layers in geant. *Nuclear Instruments and Methods in Physics Research Section A: Accelerators, Spectrometers, Detectors and Associated Equipment*, 362(2):416–422, 1995.
- [26] Abhijit Samanta. The Mass hierarchy with atmospheric neutrinos at INO. *Phys.Lett.*, B673:37–46, 2009.
- [27] Anushree Ghosh, Tarak Thakore, and Sandhya Choubey. Determining the Neutrino Mass Hierarchy with INO, T2K, NOvA and Reactor Experiments. *JHEP*, 1304:009, 2013.

- [28] Moon Moon Devi, Tarak Thakore, Sanjib Kumar Agarwalla, and Amol Dighe. Enhancing sensitivity to neutrino parameters at ino combining muon and hadron information. *Journal of High Energy Physics*, 2014(10):1–26, 2014.
- [29] Nickolas Solomey. The elusive neutrino: A subatomic detective story. *The elusive neutrino: a subatomic detective story/Nickolas Solomey*. New York: Scientific American Library; distributed through WH Freeman, 1997. QC 793.5 N422 S65 1997., 1, 1997.
- [30] BEISER ARTHUR. Concepts of modern physics, 1995.
- [31] Clyde L Cowan, Frederick Reines, FB Harrison, HW Kruse, and AD McGuire. Detection of the free neutrino: A confirmation. *Science*, 124(3212):103–104, 1956.
- [32] Chien-Shiung Wu, Ernest Ambler, RW Hayward, DD Hoppes, and R Pl Hudson. Experimental test of parity conservation in beta decay. *Physical review*, 105(4):1413, 1957.
- [33] Maurice Goldhaber, L Grodzins, and AW Sunyar. Helicity of neutrinos. *Physical Review*, 109(3):1015, 1958.
- [34] Gaillard Danby, JM Gaillard, Konstantin Goulianos, LM Lederman, N Mistry, M Schwartz, and J Steinberger. Observation of high-energy neutrino reactions and the existence of two kinds of neutrinos. *Physical Review Letters*, 9(1):36, 1962.
- [35] K Kodama, N Ushida, C Andreopoulos, N Saoulidou, G Tzanakos, P Yager, B Baller, D Boehnlein, W Freeman, B Lundberg, et al. Observation of tau neutrino interactions. *Physics Letters B*, 504(3):218–224, 2001.
- [36] John N Bahcall and Raymond Davis Jr. Solar neutrinos: A scientific puzzle. *Science*, 191(4224):264–267, 1976.
- [37] Bruce T Cleveland, Timothy Daily, Raymond Davis Jr, James R Distel, Kenneth Lande, CK Lee, Paul S Wildenhain, and Jack Ullman. Measurement of the solar electron neutrino flux with the homestake chlorine detector. *The Astrophysical Journal*, 496(1):505, 1998.
- [38] JN Abdurashitov, EL Faizov, VN Gavrin, AO Gusev, AV Kalikhov, TV Knodel, II Knyshenko, VN Kornoukhov, IN Mirmov, AM Pshukov, et al. Results from sage (the russian-american gallium solar neutrino experiment). *Physics Letters B*, 328(1):234–248, 1994.
- [39] Wolfgang Hampel, J Handt, G Heusser, J Kiko, T Kirsten, M Laubenstein, E Pernicka, W Rau, M Wojcik, Yu Zakharov, et al. Gallex solar neutrino observations: Results for gallex iv. *Physics Letters B*, 447(1):127–133, 1999.
- [40] Yoichiro Suzuki. Kamiokande solar neutrino results. *Nuclear Physics B-Proceedings Supplements*, 38(1):54–59, 1995.
- [41] QR Ahmad, RC Allen, TC Andersen, JD Anglin, JC Barton, EW Beier, M Bercovitch, J Bigu, SD Biller, RA Black, et al. Direct evidence for neutrino flavor transformation

- from neutral-current interactions in the sudbury neutrino observatory. *Physical Review Letters*, 89(1):011301, 2002.
- [42] Gian Luigi Fogli, E Lisi, A Marrone, and G Scioscia. Super-kamiokande atmospheric neutrino data, zenith distributions, and three-flavor oscillations. *Physical Review D*, 59(3):033001, 1998.
- [43] V Gribov and B Pontecorvo. Neutrino astronomy and lepton charge. *Physics Letters B*, 28(7):493–496, 1969.
- [44] Ziro Maki, Masami Nakagawa, and Shoichi Sakata. Remarks on the unified model of elementary particles. *Progress of Theoretical Physics*, 28(5):870–880, 1962.
- [45] Brian Martin. *Nuclear and particle physics: An introduction*. John Wiley & Sons, 2006.
- [46] Juerg Beringer, JF Arguin, RM Barnett, K Copic, O Dahl, DE Groom, CJ Lin, J Lys, H Murayama, CG Wohl, et al. Review of particle physics. *Physical Review D*, 86(1), 2012.
- [47] Makoto Kobayashi and Toshihide Maskawa. Cp-violation in the renormalizable theory of weak interaction. *Progress of Theoretical Physics*, 49(2):652–657, 1973.
- [48] KamLAND& Eguchi, S Enomoto, K Furuno, J Goldman, H Hanada, H Ikeda, K Ikeda, K Inoue, K Ishihara, W Itoh, et al. First results from kamland: evidence for reactor antineutrino disappearance. *Physical Review Letters*, 90(2):021802, 2003.
- [49] Lincoln Wolfenstein. Neutrino oscillations in matter. *Physical Review D*, 17(9):2369, 1978.
- [50] Douglas Michael. The minos experiment. *Nuclear Physics B-Proceedings Supplements*, 118:189–196, 2003.
- [51] C Athanassopoulos, LB Auerbach, RL Burman, DO Caldwell, ED Church, I Cohen, JB Donahue, A Fazely, FJ Federspiel, GT Garvey, et al. Results on  $\nu_{\mu} \rightarrow \nu_e$  neutrino oscillations from the lsnd experiment. *Physical Review Letters*, 81(9):1774, 1998.
- [52] AA Aguilar-Arevalo, BC Brown, L Bugel, G Cheng, ED Church, JM Conrad, R Dharmapalan, Z Djurcic, DA Finley, R Ford, et al. Improved search for  $\nu_{\mu} \rightarrow \nu_e$  oscillations in the mini-boone experiment. *Physical review letters*, 110(16):161801, 2013.
- [53] Jose Luis Alcaraz-Aunión and Joseph Walding. Measurement of the muon-neutrino charged-current quasi-elastic cross-section in the sciboone experiment. *arXiv preprint arXiv:0909.5647*, 2009.
- [54] Kevin S McFarland, MINER  $\nu$ A Collaboration, et al. Miner  $\nu$ a: a dedicated neutrino scattering experiment at numi. *Nuclear Physics B-Proceedings Supplements*, 159:107–112, 2006.

- [55] DD Stancil, P Adamson, M Alania, L Aliaga, M Andrews, C Araujo Del Castillo, L Bagby, JL Bazo Alba, A Bodek, D Boehnlein, et al. Demonstration of communication using neutrinos. *Modern Physics Letters A*, 27(12):1250077, 2012.
- [56] D Ayres, NOvA Collaboration, et al. Nova proposal to build a 30 kiloton off-axis detector to study neutrino oscillations in the fermilab numi beamline. *arXiv preprint hep-ex/0503053*, 2005.
- [57] K Abe, N Abgrall, H Aihara, Y Ajima, JB Albert, D Allan, P-A Amaudruz, C Andreopoulos, B Andrieu, MD Anerella, et al. The t2k experiment. *Nuclear Instruments and Methods in Physics Research Section A: Accelerators, Spectrometers, Detectors and Associated Equipment*, 659(1):106–135, 2011.
- [58] M Apollonio, A Baldini, C Bemporad, E Caffau, F Cei, Y Declais, H De Kerret, B Dieterle, A Etenko, J George, et al. Limits on neutrino oscillations from the chooz experiment. *Physics Letters B*, 466(2):415–430, 1999.
- [59] Jun Cao. Daya bay neutrino experiment. *arXiv preprint hep-ex/0509041*, 2005.
- [60] JK Ahn, S Chebotaryov, JH Choi, S Choi, W Choi, Y Choi, HI Jang, JS Jang, EJ Jeon, IS Jeong, et al. Observation of reactor electron antineutrinos disappearance in the reno experiment. *Physical Review Letters*, 108(19):191802, 2012.
- [61] F Arneodo. The icarus experiment, a second-generation proton decay experiment and neutrino observatory at the gran sasso laboratory. *arXiv preprint hep-ex/0103008*, 2001.
- [62] N Agafonova, A Aleksandrov, O Altinok, M Ambrosio, A Anokhina, S Aoki, A Ariga, T Ariga, D Autiero, A Badertscher, et al. Observation of a first  $\nu\tau$  candidate event in the opera experiment in the cngs beam. *Physics Letters B*, 691(3):138–145, 2010.
- [63] Abraham Achterberg, M Ackermann, J Adams, J Ahrens, K Andeen, DW Atlee, J Baccus, JN Bahcall, X Bai, B Baret, et al. First year performance of the icecube neutrino telescope. *Astroparticle Physics*, 26(3):155–173, 2006.
- [64] F Capozzi, GL Fogli, E Lisi, A Marrone, D Montanino, and A Palazzo. Status of three-neutrino oscillation parameters, circa 2013. *Physical Review D*, 89(9):093018, 2014.
- [65] Joachim Wolf, Katrin Collaboration, et al. The katrin neutrino mass experiment. *Nuclear Instruments and Methods in Physics Research Section A: Accelerators, Spectrometers, Detectors and Associated Equipment*, 623(1):442–444, 2010.
- [66] R Santonico and R Cardarelli. Development of resistive plate counters. *Nuclear Instruments and Methods in physics research*, 187(2):377–380, 1981.
- [67] R Cardarelli, A Di Ciaccio, and R Santonico. Performance of a resistive plate chamber operating with pure cf 3 br. *Nuclear Instruments and Methods in Physics Research Section A: Accelerators, Spectrometers, Detectors and Associated Equipment*, 333(2):399–403, 1993.

- [68] S. Agostinelli et al. Geant4 - a simulation toolkit. *Nuclear Instruments and Methods in Physics Research Section A: Accelerators, Spectrometers, Detectors and Associated Equipment*, 506(3):250 – 303, 2003.
- [69] D. Casper. The Nuance neutrino physics simulation, and the future. *Nucl.Phys.Proc.Suppl.*, 112:161–170, 2002.
- [70] Costas Andreopoulos, A Bell, D Bhattacharya, F Cavanna, J Dobson, S Dytman, H Gallagher, P Guzowski, R Hatcher, P Kehayias, et al. The genie neutrino monte carlo generator. *Nuclear Instruments and Methods in Physics Research Section A: Accelerators, Spectrometers, Detectors and Associated Equipment*, 614(1):87–104, 2010.
- [71] SP Behera, N Dash, MS Bhatia, VM Datar, and P Verma. On the simulation of the iron calorimeter magnet for ino. In *Proceedings of the DAE Symp. on Nucl. Phys*, volume 55, page 776, 2010.
- [72] MagNet User’s Manual. Infolytica corporation. *Montreal, Canada*, 2011.
- [73] William H Press. *Numerical recipes 3rd edition: The art of scientific computing*. Cambridge university press, 2007.
- [74] Edwin Bos. Reconstruction of charged particles in the lhcb experiment. *CERN-3301 THESIS-2010-049. URL*, 3302, 2009.
- [75] Rainer Mankel. Pattern recognition and event reconstruction in particle physics experiments. *Reports on Progress in Physics*, 67(4):553, 2004.
- [76] Sudeshna Dasgupta, Deepak Samuel, Mandar N Saraf, Bheesette Satyanarayana, Suresh S Upadhya, and Naba K Mondal. Proposed trigger scheme for the ical detector of india-based neutrino observatory. *PoS*, page 068, 2012.
- [77] Philip R Bevington and D Keith Robinson. Data reduction and error analysis. *McGraw–Hill, New York*, 2003.
- [78] Morihiro Honda, Takaaki Kajita, Katsuaki Kasahara, and Shoichi Midorikawa. Improvement of low energy atmospheric neutrino flux calculation using the jam nuclear interaction model. *Physical Review D*, 83(12):123001, 2011.
- [79] Rudolph Emil Kalman. A new approach to linear filtering and prediction problems. *Transactions of the ASME–Journal of Basic Engineering*, 82(Series D):35–45, 1960.
- [80] R. Frühwirth, M. Regler, R. K. Bock, H. Grote, and D. Notz. *Data Analysis Techniques for High-Energy Physics (Cambridge Monographs on Particle Physics, Nuclear Physics and Cosmology)*. Cambridge University Press, 2000.
- [81] Tapasi Ghosh and Subhasis Chattopadhyay. Track fitting by Kalman Filter method for a prototype cosmic ray muon detector. *arXiv*, 2009.
- [82] Juan Andrade Cetto and Alberto Sanfeliu. *Environment Learning for Indoor Mobile Robots: A Stochastic State Estimation Approach to Simultaneous Localization and Map Building (Springer Tracts in Advanced Robotics)*. Springer, 2006.

- [83] Martin A Salzmann and University of New Brunswick. Dept. of Surveying Engineering. *Some aspects of Kalman filtering*. University of New Brunswick Canada, 1988.
- [84] Arnold W Heemink, Martin Verlaan, and Arjo J Segers. Variance reduced ensemble kalman filtering. *Monthly Weather Review*, 129(7):1718–1728, 2001.
- [85] R. Frühwirth. Application of Kalman filtering to track and vertex fitting. *Nucl.Instrum.Meth.*, A262:444–450, 1987.
- [86] K. Nakamura et al. Review of particle physics. *J.Phys.*, G37:075021, 2010.
- [87] W Wittek. Propagation of errors along a particle trajectory in a magnetic field. Technical Report EMC-80-15, EMC-80-15-ADD-1, CERN, Geneva, 1980-81.
- [88] Wolfram Res Mathematica. Inc., champaigne il, 2011.
- [89] Donald E Groom, Nikolai V Mokhov, and Sergei I Striganov. Muon stopping power and range tables 10 mev–100 tev. *Atomic Data and Nuclear Data Tables*, 78(2):183–356, 2001.
- [90] Donald E. Groom, Nikolai V. Mokhov, and Sergei I. Striganov. Muon stopping power and range tables 10-MeV to 100-TeV. *Atom.Data Nucl.Data Tabl.*, 78:183–356, 2001.
- [91] Particle Data Group. Muon in iron. [http://pdg.lbl.gov/2013/AtomicNuclearProperties/MUON\\_ELOSS\\_TABLES/muonloss\\_026.dat](http://pdg.lbl.gov/2013/AtomicNuclearProperties/MUON_ELOSS_TABLES/muonloss_026.dat), 2013.
- [92] Lewis Fry Richardson. The approximate arithmetical solution by finite differences of physical problems involving differential equations, with an application to the stresses in a masonry dam. *Philosophical Transactions of the Royal Society of London. Series A, Containing Papers of a Mathematical or Physical Character*, pages 307–357, 1911.
- [93] Gerald R Lynch and Orin I Dahl. Approximations to multiple coulomb scattering. *Nuclear Instruments and Methods in Physics Research Section B: Beam Interactions with Materials and Atoms*, 58(1):6–10, 1991.
- [94] Rainer Mankel and Alexander Spiridonov. Ranger, a pattern recognition algorithm. *HERA-B note*, pages 97–082, 1997.
- [95] Virgil L Highland. Some practical remarks on multiple scattering. *Nuclear Instruments and Methods*, 129(2):497–499, 1975.
- [96] Hans Bichsel, DE Groom, and SR Klein. Passage of particles through matter. *J. Phys. G*, 637:285, 2010.
- [97] Francesco Ragusa. An introduction to charged particles tracking. *Presentation slides, Martignano, Italy June*, 2006.
- [98] RL Gluckstern. Uncertainties in track momentum and direction, due to multiple scattering and measurement errors. *Nuclear Instruments and Methods*, 24:381–389, 1963.

- [99] John Hauptman. *Particle physics experiments at high energy colliders*. John Wiley & Sons, 2011.
- [100] Animesh Chatterji, Kanishka Rawat, Meghna, and Tarak Thakore. Muon reconstruction look up table, v2. Technical report, INO Collaboration, 2012.
- [101] Abhijit Samanta. Discrimination of mass hierarchy with atmospheric neutrinos at a magnetized muon detector. *arXiv preprint arXiv:0907.3540*, 2009.
- [102] Roger J Barlow. *Statistics: a guide to the use of statistical methods in the physical sciences*, volume 29. John Wiley & Sons, 1989.
- [103] Steve Baker and Robert D Cousins. Clarification of the use of chi-square and likelihood functions in fits to histograms. *Nuclear Instruments and Methods in Physics Research*, 221(2):437–442, 1984.
- [104] Ali Ajmi and S Uma Sankar. Muonless events in ical at ino. *Journal of Instrumentation*, 10(04):P04006, 2015.
- [105] Shakeel Ahmed, M Sajjad Athar, Rashid Hasan, Mohammad Salim, SK Singh, SSR Inbanathan, Venkatesh Singh, VS Subrahmanyam, Shiba Prasad Behera, Vinay B Chandratre, et al. Physics potential of the ical detector at the india-based neutrino observatory (ino). *arXiv preprint arXiv:1505.07380*, 2015.
- [106] A Strandlie and W Wittek. Derivation of jacobians for the propagation of covariance matrices of track parameters in homogeneous magnetic fields. *Nuclear Instruments and Methods in Physics Research Section A: Accelerators, Spectrometers, Detectors and Associated Equipment*, 566(2):687–698, 2006.